Ion yields in HIGISOL experiments

– based on JYFLTRAP data and PACE4 simulations –

Laura Vainio

Master's Thesis
March 2012

Supervisor:
Ph.D. Anu Kankainen

UNIVERSITY OF JYVÄSKYLÄ
DEPARTMENT OF PHYSICS

Abstract

The purpose of this thesis was to calculate ion yields in the neutron-deficient mass region A=78-111 in heavy-ion ion-guide experiments at the Ion Guide Isotope Separator On-Line (IGISOL) facility in the Accelerator Laboratory of the University of Jyväskylä. The biggest challenge was that the experiments were not designed for yield calculations but for precision mass measurements. Therefore, only a small fraction of the available data could be used.

The results were compared to theoretical cross sections calculated with PACE4 code. Ion yields agreed roughly with the cross-section calculations: On the one hand, the ions with the highest cross sections were detected. On the other hand, ratios between calculated cross sections and measured ion rates differed in some cases even within the same file. Cross sections for measured isotopes were in general more than 1 mb. Stable isotopes, which are used for calibration and reference purposes, were detected although no calculated cross section existed.

Finally, some cross-section calculations were performed in order to find reasonable beam, target and energy combinations for future measurements. Main focus was on extending the JYFLTRAP measurements in the neutron-deficient A=78-111 region. Masses of some nuclei are already known with a precision which will be difficult to beat. For many of the nuclei of interest the calculated cross sections were found to be too small in order to safely evaluate whether measuring would succeed or not. Based on PACE4 calculations, the most promising candidates for future measurements are for example ^{79}Y, ^{81,82}Zr, ^{83,84}Nb, $^{96-98}$Ag and ^{100,101}In.

Tiivistelmä

Tässä tutkielmassa määritettiin ionituottoja Jyväskylän yliopiston kiihdytinlaboratorion IGISOL-laitteistolla suoritetuissa raskasioniohjainkokeissa neutronivajaalla massa-alueella A=78-111. Määritys perustui kahdesta Penning-loukusta koostuvan JYFLTRAP-laitteiston avulla suoritetuissa massamittauksissa kerättyyn mittausaineistoon, josta vain pieni osa soveltui tuottojen laskemiseen.

Laskettuja ionituottoja verrattiin PACE4-koodilla laskettuihin vaikutusaloihin. Ionit, joita PACE4-koodin mukaan tuotettiin eniten, olivat helposti havaittavissa mittausaineistossa. Toisaalta laskettujen vaikutusalojen ja tuottojen suhteet vaihtelivat paljon yhdenkin mittauksen sisällä. Lisäksi havaittiin kalibroinnissa tai vertailuisotooppeina käytettyjä pysyviä isotooppeja, joilla ei ollut laskettua vaikutusalaa. Vaikutusalojen ja tuottojen vertailua vaikeutti epävarmuus vanhoista mittausasetuksista. Joidenkin isotooppien kohdalla myös PACE4-koodilla lasketut vaikutusalat voivat olla virheellisiä epätarkoista massaylijäämistä johtuen.

Lopuksi, PACE4-vaikutusaloja laskettiin tulevaisuuden mittauksia silmälläpitäen. Laskuja suoritettiin eri suihkuilla, kohtioilla ja suihkun energioilla tavoitteena täydentää JYFLTRAP-mittaukset massa-alueella A=78-111. Osa kyseisen alueen ydinten massoista tunnetaan jo tarkkuudella, jota tuskin voidaan parantaa nykyisellä raskasioniohjain-laitteistolla. Suurin osa lasketuista vaikutusaloista oli niin pieniä, ettei niiden perusteella voida sanoa mitään varmaa mittauksen onnistumisesta. Mitatuille isotoopeille vaikutusala oli tyypillisesti $\sigma > 1$ mb. Tämän perusteella lupaavimpia isotooppeja mitattaviksi tulevaisuudessa ovat mm. ^{79}Y, ^{81,82}Zr, ^{83,84}Nb, $^{96-98}$Ag ja ^{100,101}In.

Contents

1 Introduction

In this thesis, ion yields in heavy-ion ion-guide experiments performed at the IGISOL facility in the Accelerator Laboratory of the University of Jyväskylä are determined. The determination is based on data from precision mass measurements with the Penning trap system JYFLTRAP. Yields are also compared to cross sections calculated with PACE4 code for reactions used in the experiments. The measurements were focused on the neutron-deficient mass region A=78-111.

Precise information on ion yields can be used to improve the accuracy of cross-section calculations with codes such as PACE4 and thus to ease the planning of new experiments. It can also deepen the understanding of the function of the measurement set-up. IGISOL measurements in the neutron-deficient mass region in question give valuable information for the study of nuclear astrophysics, shell model and isomers. These are elaborated further in Section 2.

2 Motivation for HIGISOL experiments

2.1 Nuclear Astrophysics

2.1.1 *rp* process

One of the greatest motivations for the study of nuclei near the N=Z line is nuclear astrophysics. The astrophysical rapid proton capture process (*rp* process) [1] is a sequence of proton captures and beta decays on the neutron-deficient side of the line of stability. This nucleosynthesis process occurs at high temperatures ($T > 10^8$ K) and hydrogen densities e.g. in x-ray bursts. In an x-ray burst, hydrogen-rich matter is accreted on the surface of a neutron star from the surface layers of a close companion star leading to thermonuclear burning. The *rp* process starts with a breakout from the CNO cycle, in which helium is produced via proton captures on catalytic carbon, nitrogen and oxygen isotopes and β-decays. The process proceeds as fast proton captures until negative or low proton capture Q-value occurs and further capture is hampered [2]. At this point, the process can continue via a β-decay. The β-decaying nuclei are called "waiting points" since β-decay is relatively slow. Timescale of the process is of the order of seconds. Whether a nucleus is a waiting point or not depends on the temperature and density conditions. According to current knowledge, the process ends in a SnSbTe cycle [3]. The path of the *rp* process in x-ray bursts is illustrated in Fig 1. In x-ray pulsars, for example, the path is wider.

Produced isotopic abundances depend on the processing speed of the *rp* process since the timescale of the requisite conditions for example in x-ray bursts is short [2]. The material is stored in the waiting point nuclei whose total lifetimes determine the speed of the process and thus the isotopic abundances. The total lifetime of a waiting point nucleus depends also on 2p-capture reactions. When the process stops, all nuclei β-decay towards the line of stability. The *rp* process has been studied as a possible explanation for the production of some light p-nuclei, i.e. neutron-deficient stable nuclei, such as ^{92}Mo, whose origin is yet unknown. Fig. 2 shows that many of the p-nuclei can be produced in the *rp* process. This does not necessarily explain the solar abundances since only a small fraction of the produced nuclei may possibly be ejected due to a strong gravitational field of the underlying neutron star. An escape factor of roughly 1% would explain the observed solar system abundances of p-nuclei like ^{84}Sr, ^{92}Mo and ^{96}Ru [4].

Accurate nuclear masses and β-decay half-lives are crucial in order to model the process reliably since reaction rates depend exponentially on Q-value, i.e. masses [5]. Masses can be measured with high accuracy at JYFLTRAP and half-lives with a decay spectroscopy setup after IGISOL or JYFLTRAP. The opera-

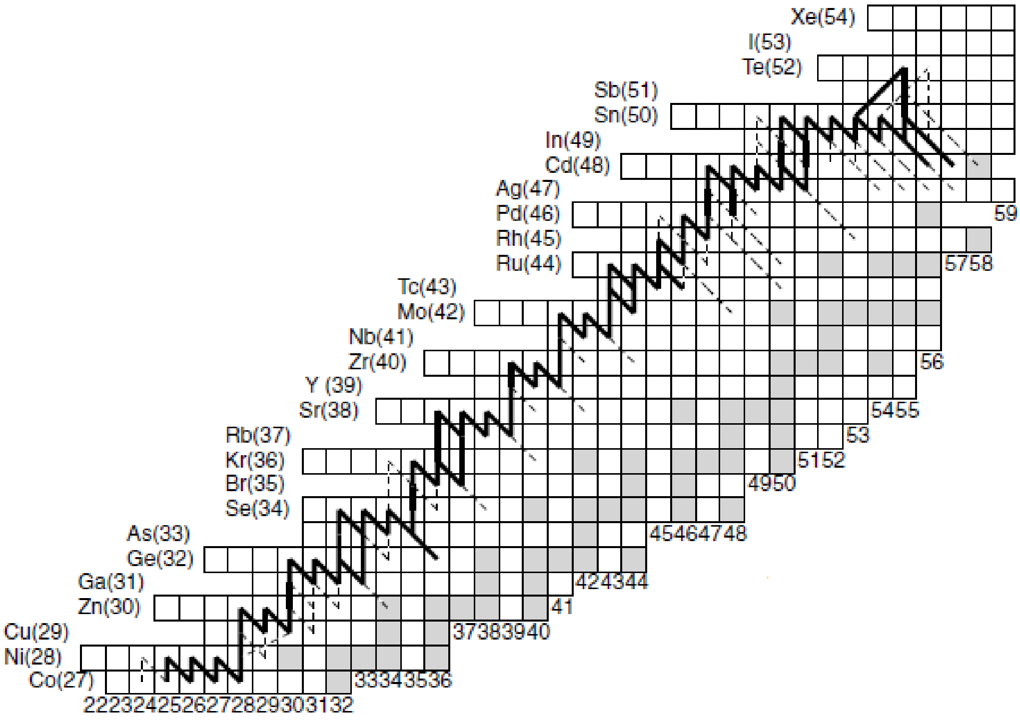

Figure 1: Rapid proton capture process in x-ray bursts [3].

tion principles of the ion-guide system IGISOL and the Penning trap facility JYFLTRAP are explained in section 3.

2.1.2 νp process

Another process explaining the production of neutron-deficient nuclei with $A > 64$ in the same region as the *rp* process has been introduced [6-8]. The νp process proceeds, like the *rp* process, as a sequence of proton captures and beta decays but the nucleosynthesis can bypass waiting-point nuclei with long β-decay half-lives via (n,p) reactions. The process occurs in core-collapse supernovae.

According to supernova simulations that take accurate neutrino transport into account, the early innermost ejecta of a core-collapse supernova is proton rich. As the proton-rich neutrino-heated ejecta expands and cools, nuclei start to form and the ejecta will consist mostly of protons and N=Z nuclei such as ^{4}He and ^{56}Ni. Now, without consideration of neutrino and antineutrino reactions,

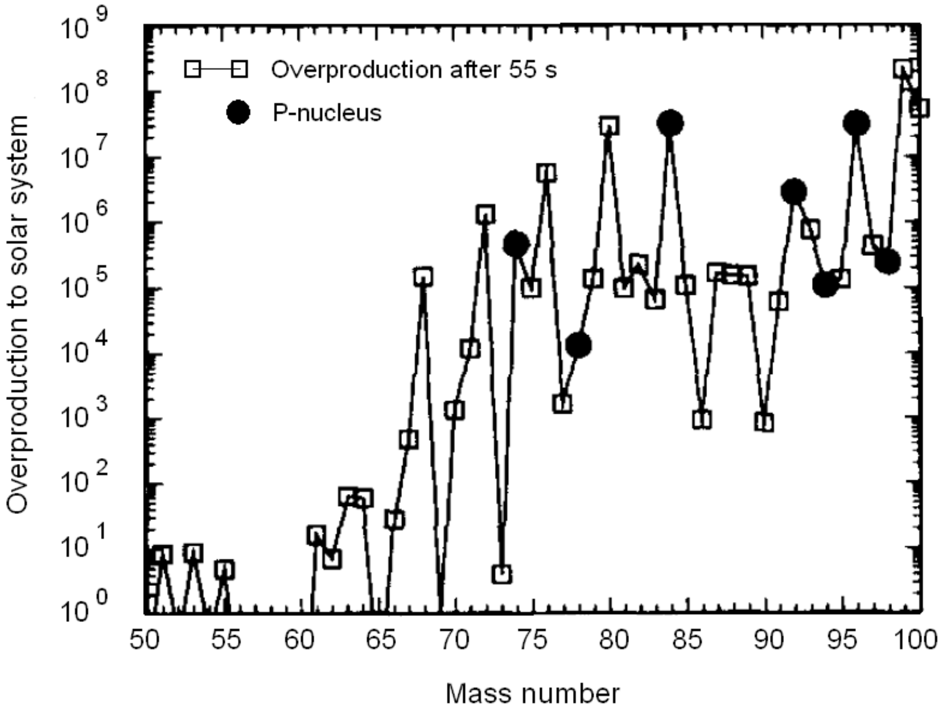

Figure 2: Overabundance pattern at the time of maximum ^{92}Pd production in the *rp* process [4]. The overproduction factors are calculated as the sum of all abundances in a mass chain divided by the solar abundance of the most proton-rich stable nucleus.

the nucleosynthesis would not pass waiting points (e.g. ^{64}Ge) due to long β-decay half-lives and small proton capture probabilities. Neutrino captures on neutron-deficient N$\sim$Z nuclei are endoergic but antineutrino captures occur on both protons and nuclei, mainly on more abundant protons. The resulting neutrons are easily captured by neutron-deficient nuclei, such as ^{64}Ge, allowing the nucleosynthesis to continue to heavier nuclei via proton captures.

The *νp* process is also a strong candidate for the origin of light p-nuclei. It differs from the *rp* process in that the nuclei produced in the *νp*-process conditions are strongly ejected. Figure 3 shows that in the inner ejecta of supernovae the production of the p-nuclei depends on the electron abundance Y_e [6]. In Ref. [7], nucleosynthesis in both neutron-rich and proton-rich neutrino-driven winds was investigated. The production of p-nuclei was shown to depend on the proton abundance and the entropy in the wind. Interestingly, as can be seen from Fig. 4, a higher production of p-nucleus ^{92}Mo was detected in slightly neutron-rich winds ($Y_e \approx 0.46$ - 0.49) than in proton-rich winds ($Y_e > 0.5$). Again, precision mass measurements are needed to improve the simulations and thus to determine if the observed abundances of the p-nuclei are due to the νp process.

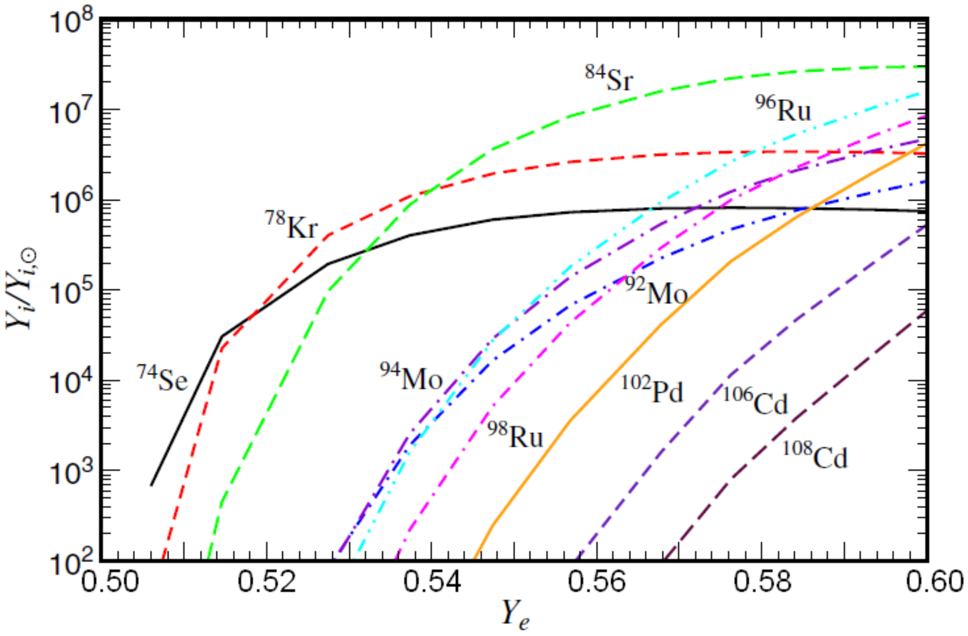

Figure 3: P-nuclei abundances with respect to solar abundances as a function of electron abundance Y_e at the beginning of the νp process phase ($T = 3\,\mathrm{GK}$) [6]. The larger the Y_e value, the larger the proton abundance. In Ref. [6], only proton-rich conditions ($Y_e > 0.5$) were investigated.

2.2 Shell Model and Isomers

The nuclei in the region Z=40-50 near the N=Z line have been of special interest in nuclear structure studies [9-15]. The nuclear shell model describes the structure of the nucleus in terms of energy levels, or shells. Magic numbers indicate nucleon numbers at which large gaps between energy levels occur (Fig. 5). The studies of Z=40-50 nuclei can be used to test the shell model and to explore excitations across the N=Z=50 shell gap. Accurate information on nuclear structure is also useful in nuclear astrophysics since the reaction rates and therefore the paths of the astrophysical processes depend on the nuclear structure [2].

The region close to N=Z=50 is also interesting due to occurence of high-spin isomers. High-spin isomers have recently been found for example in ^{95}Ag [12]

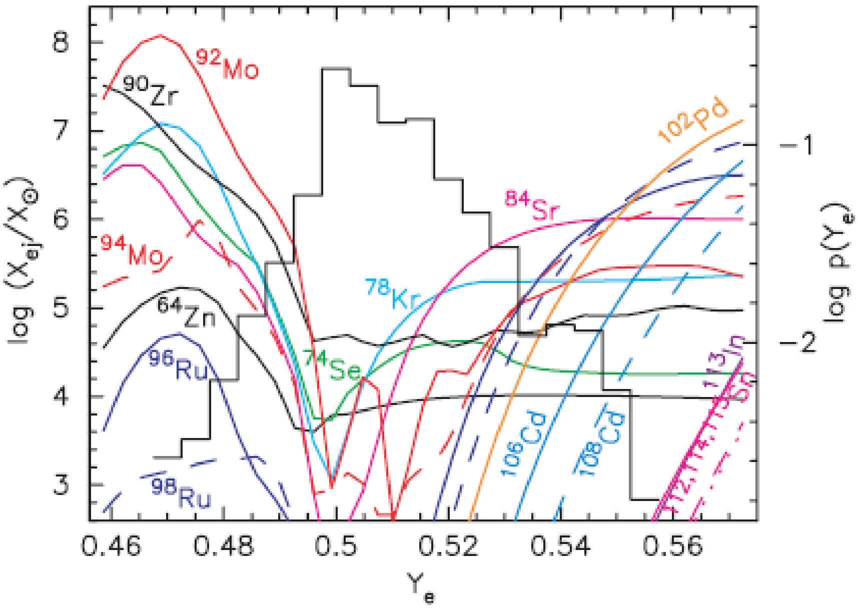

Figure 4: Mass fractions of p-nuclei in comparison to solar values against electron abundance Y_e at $T = 3\,\mathrm{GK}$ from Ref. [7] where nucleosynthesis in both neutron-rich and proton-rich neutrino-driven winds was studied. A higher production of p-nucleus ^{92}Mo was detected in slightly neutron-rich winds than in proton-rich winds.

and ^{94}Pd [12,13]. The high-spin 21^+ isomer in ^{94}Ag with a high excitation energy and a relatively long half-life of 0.39(4) s has been of special interest [14,15]. Studies of these isomers provides information on neutron–proton interaction since according to current shell-model knowledge high-spin isomers are formed by an extra binding energy due to large attractive proton-neutron interaction. Furthermore, the existence of isomeric states can effect β-decay lifetimes and proton capture rates and thus the timescale of the *rp* process. For example, a reduction of 17% in the effective ^{80}Y β-decay lifetime was established in the study of the 228.5 keV isomeric state of ^{80}Y [16]. Other isomers of astrophysical interest have also been studied at IGISOL [15,17]. Estimated yields are important for planning new experiments in this region.

2.3 Fusion-evaporation Reactions

A fusion-evaporation reaction is a compound nucleus reaction [18,19]. As a first step, a particle enters a target nucleus and interacts with target nucleons. The incoming particle and the target nucleus coalesce and form a compound nucleus which is at an excited state. The reaction can be light-particle (e.g. $p+^{92}Mo \rightarrow ^{93}Tc^*$) or heavy-particle (e.g. $^{40}Ca+^{58}Ni \rightarrow ^{98}Ca^*$) induced. The compound nucleus can then decay in several ways. The decay and the formation are separate processes i.e. the compound nucleus "forgets" how it was formed. Minimum amount of excitation energy is eligible if particle evaporation is pursued instead of fission, especially for heavier nuclei due to higher fission probability. Usually, the compound nucleus evaporates a neutron but depending on the available energy several neutrons or charged particles can be evaporated. At higher energies, the evaporation of several particles is favoured over the evaporation of fewer high-energy particles.

Neutron-deficient nuclei can be produced via fusion-evaporation reactions but there is a limited choice of isotopes which can be used as beam and target materials. Heavy-ion-induced reactions produce neutron-deficient nuclei further away from the valley of stability whereas light-ion-induced reactions are exploited in experiments closer to stable nuclei. However, light-ion reactions with high beam intensities can ensue in higher counting rates and more favourable populated low-spin states for isomer studies [20]. Experimental data on production rates in fusion-evaporation reactions yield necessary information for more rigorous modelling of the production process. It also helps in optimizing the measurement set-ups.

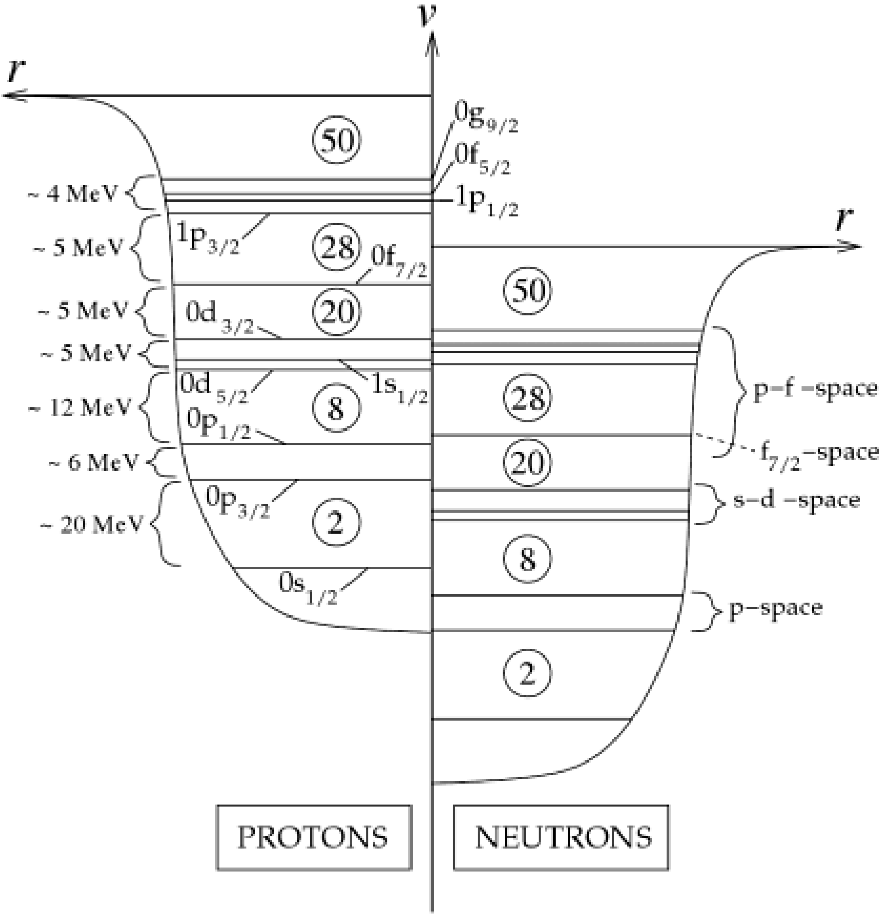

Figure 5: Schematic view of mean-field potentials with energy shells for protons and neutrons [21]. Magic numbers and rough gap energies are shown. In the mean-field approximation each nucleon is treated as moving in an external field created by the remaining nucleons.

2.4 Previous Mass Measurements in the Neutron-deficient Mass Region Around A=80-110

The history of the development of nuclear mass measurements is briefly presented in Ref. [22]. Lately, there has been a large improvement in precision due to a powerful Penning trap technique. For example, in year 2006 the Q_{EC} value of ^{86}Nb was improved from the AME2003 value of 7980(80) keV [23] to 8829(9) keV [24]. The Penning trap mass spectrometer enables direct mass measurements whereas the past mass and Q_{EC} values were typically based on determination of the β-decay end-point energy, i.e. the maximum β-particle energy. The end-point-energy method often gives incorrect results since β-decay to higher-lying excited states may have been unobserved in those experiments.

Several facilities have utilized the Penning trap technique in the mass determination of neutron-deficient nuclei in the mass region around A=80-110 relevant for HIGISOL experiments. The targets and corresponding beam energies used at JYFLTRAP [20,24-26], SHIPTRAP [25,27,28], ISOLTRAP [29] and Canadian Penning trap (CPT) [30] facilities are presented in Table 1. Both heavy-ion and light-ion induced reactions have been used. At ISOLTRAP, the high-energy proton beam produces the nuclei of interest via spallation reaction. Nuclear astrophysics is a strong motivation for all of these measurements. The mass of some of the nuclei has been measured with more than one Penning trap. The agreement between the different facilities further supports the accuracy of these measurements. The neutron-deficient nuclei whose masses were measured with JYFLTRAP by way of the reactions in Table 1 can be seen from Fig. 6. In other facilities, over 50 nuclei from Rb to Xe were measured.

Table 1: Used reactions and beam energies in the study of neutron-deficient nuclei at JYFLTRAP in Finland, SHIPTRAP in Germany, ISOLTRAP in CERN and CPT in the USA. All results of the ^{40}Ca+$^{\mathrm{nat}}$Ni experiments at JYFLTRAP have not been published yet.

	Reaction	Beam energy (MeV)	Ref.
JYFLTRAP	p+^{92}Mo	62	[20]
	p+^{106}Cd	62	[20]
	^{3}He+$^{\mathrm{nat}}$Ru	70	[20]
	^{3}He+^{106}Cd	70-100	[20]
	^{32}S+^{54}Fe	160-170	[24]
	^{32}S+$^{\mathrm{nat}}$Ni	135-170	[24]
	^{40}Ca+$^{\mathrm{nat}}$Ni	170-260	[25]
	^{36}Ar+$^{\mathrm{nat}}$Ni	222	[25]
	^{58}Ni+$^{\mathrm{nat}}$Ni	295-330	[26]
SHIPTRAP	^{40}Ca+^{58}Ni	200	[25]
	^{58}Ni+^{58}Ni	≈197-232	[27]
	^{50}Cr+^{58}Ni	199	[27]
	^{36}Ar+^{54}Fe	≈290-342	[28]
ISOLTRAP	p+$^{\mathrm{liquid}}$Sn	1400	[29]
CPT	^{40}Ca+$^{\mathrm{nat}}$Ni	170	[30]
	^{40}Ca+^{58}Ni	185-200	[30]
	^{36}Ar+$^{\mathrm{nat}}$Ni	130-150	[30]
	^{36}Ar+^{58}Ni	125	[30]

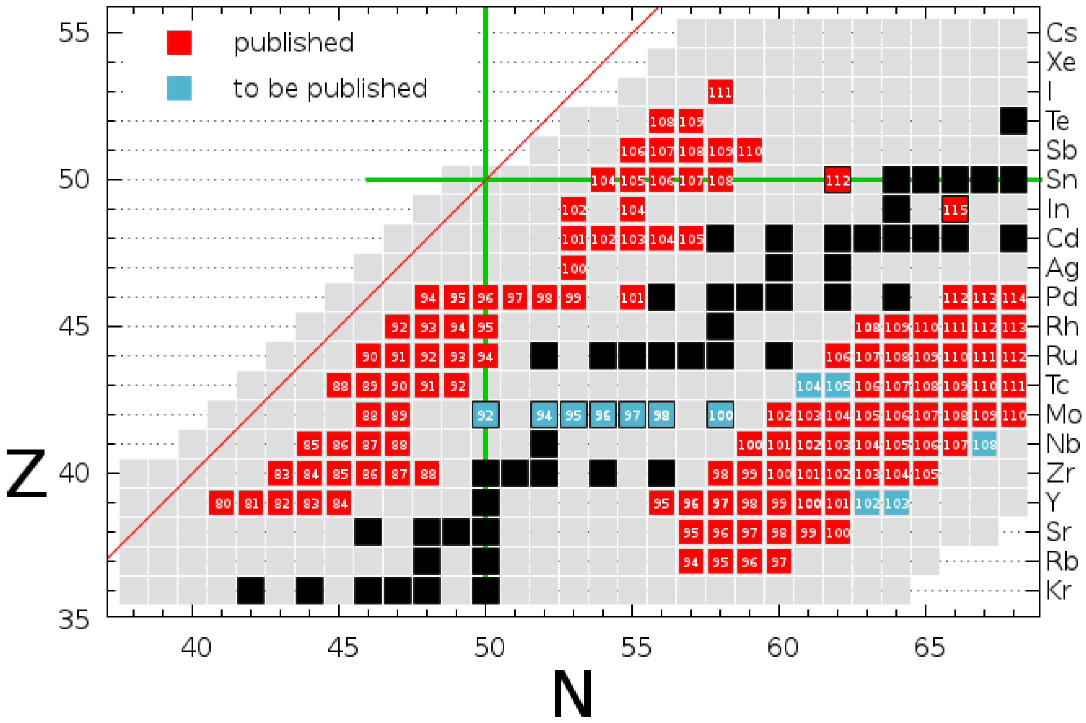

Figure 6: Nuclei whose masses have been measured at JYFLTRAP [31]. The neutron-rich nuclei on the right-hand side of the chart are produced via fission and are not discussed in this work.

3 Experimental Methods

3.1 Production of stable beams for HIGISOL experiments

The measurements were performed at IGISOL (Ion Guide Isotope Separator On-line) facility. High-energy heavy-ion beams required for IGISOL experiments are produced with Electron Cyclotron Resonance (ECR) ion sources [32] and K-130 cyclotron. In the Accelerator Laboratory of the University of Jyväskylä, two ECR ion sources, JYFL 6.4 GHz ECRIS and JYFL 14 GHz ECRIS, are used to produce highly-charged ions. In ion-production process, neutral gas and microwaves are fed into a plasma chamber. The simplest way to bring material into the plasma chamber is to use materials which are gaseous at room temperature together with appropriate valves. A wider selection of materials can be achieved with evaporation ovens [33], MIVOC method [34], sputtering [35] or laser ablation [36]. The frequencies 6.4 GHz and 14 GHZ of the JYFL ion sources refer to microwaves heating the plasma which is confined with solenoids and hexapole magnets. Free electrons in the plasma chamber can gain energy in the electric field created by the microwaves but the gyration frequency of the electrons must equal the frequency of the electromagnetic waves. This is known as electron cyclotron resonance. The electrons collide with ions and neutrals in the plasma causing ionization and charge exchange reactions. The plasma chamber must be in a good vacuum in order to minimize charge exchange between ions and neutrals so that highly-charged ions can be produced. The charged ions are then extracted using high voltage.

The charged ions from the ion source are injected into an accelerator. High charge-state is usually desirable since the final energy of the beam depends on the ion charge. The Jyväskylä K-130 cyclotron can accelerate heavy ions up to an energy of 130 q^2/A MeV. Available ion beams are shown in Fig. 7. For example, from 9+ to 12+ charged ^{40}Ca ions, corresponding to beam energies up to 468 MeV, can be produced. For ^{58}Ni charge states from 10+ to 17+ are possible corresponding to a maximum energy of 650 MeV. In 2009, a new MCC 30/15 cyclotron was installed to the Accelerator Laboratory extension. The new cyclotron can accelerate protons (18-30 MeV) and deuterons (9-15 MeV) and will be used alongside the K-130 cyclotron.

3.2 Heavy-ion Ion Guide Isotope Separator On-Line (HIGISOL)

A schematic layout of the IGISOL3 setup (in operation 2003-2010) is shown in Fig. 8. The ion-guide method for isotope separation is based on thermalization of recoil ions from nuclear reactions in gas, typically helium [37,38]. The ions are then transferred by a gas flow through a pumping system for mass separation. The method is very fast since no separate ion source is needed. There are

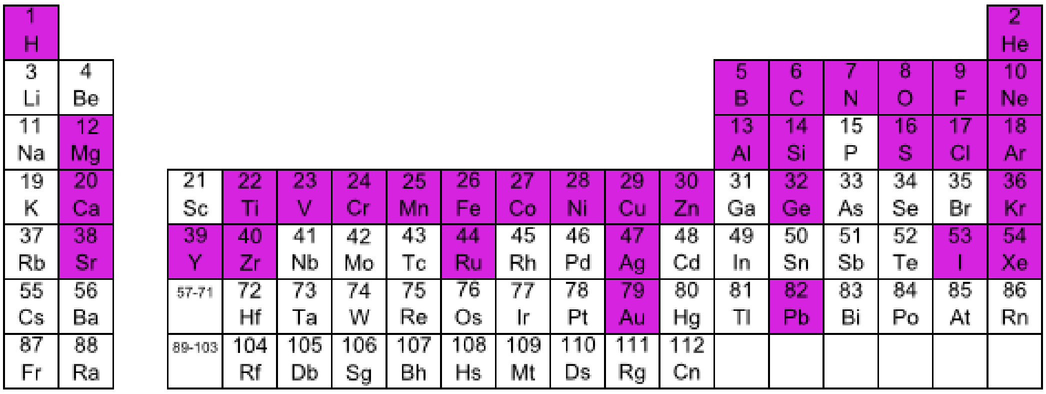

1 H																	2 He
3 Li	4 Be											5 B	6 C	7 N	8 O	9 F	10 Ne
11 Na	12 Mg											13 Al	14 Si	15 P	16 S	17 Cl	18 Ar
19 K	20 Ca	21 Sc	22 Ti	23 V	24 Cr	25 Mn	26 Fe	27 Co	28 Ni	29 Cu	30 Zn	31 Ga	32 Ge	33 As	34 Se	35 Br	36 Kr
37 Rb	38 Sr	39 Y	40 Zr	41 Nb	42 Mo	43 Tc	44 Ru	45 Rh	46 Pd	47 Ag	48 Cd	49 In	50 Sn	51 Sb	52 Te	53 I	54 Xe
55 Cs	56 Ba	57-71	72 Hf	73 Ta	74 W	75 Re	76 Os	77 Ir	78 Pt	79 Au	80 Hg	81 Tl	82 Pb	83 Bi	84 Po	85 At	86 Rn
87 Fr	88 Ra	89-103	104 Rf	105 Db	106 Sg	107 Bh	108 Hs	109 Mt	110 Ds	111 Rg	112 Cn						

Figure 7: Available accelerated ion beams at JYFL Accelerator Laboratory are shown in colour.

three main ion guide types: guides for light-ion and heavy-ion induced fusion-evaporation reactions and for fission reactions [39]. The HIGISOL (Heavy Ion Guide Isotope Separator On-line) setup used in the heavy-ion measurements of interest is shown in Fig. 9 [40,41]. The beam from the K=130 cyclotron hits a thin target in front of the ion guide gas cell. In this particular system, two changeable targets in a water-cooled frame can be installed. Target can be changed outside the vacuum chamber without breaking the vacuum. Helium gas is pumped into the target chamber in order to stop the reaction products. Next, ions, which are usually singly-charged, are extracted from the gas cell into a sextupole ion guide (SPIG) [42]. After, the low-energy ion beam is accelerated to an energy of 30 keV and a dipole magnet is used for mass separation. The beam is then guided to a triple-trap system, JYFLTRAP [43].

A low ion-guide efficiency has been a common problem encountered in heavy-ion experiments [41]. This has been due to difficulties in stopping the high-energy recoils and to ionization in the stopping gas caused by the accelerator beam. At IGISOL, this plasma effect is minimized by means of the recoil shadow method which is based on the fact that the recoiling products have a wider, nearly Gaussian angular distribution than the primary heavy ion beam with an average opening angle around 1° [44]. The accelerator beam is stopped in a mini-sized beam dump in front of the stopping chamber and the recoiling products have to pass through the surrounding about 2μm-thick Havar window (Fig. 10). Approximately less than 1 % of the primary beam enters the stopping chamber and thus the plasma effect is strongly reduced. Another possibility would be a tube inside the chamber for the beam to go through but this could have non-wanted effects on the gas flow. The distance between the target and the Havar window must be correct in order to achieve maximum

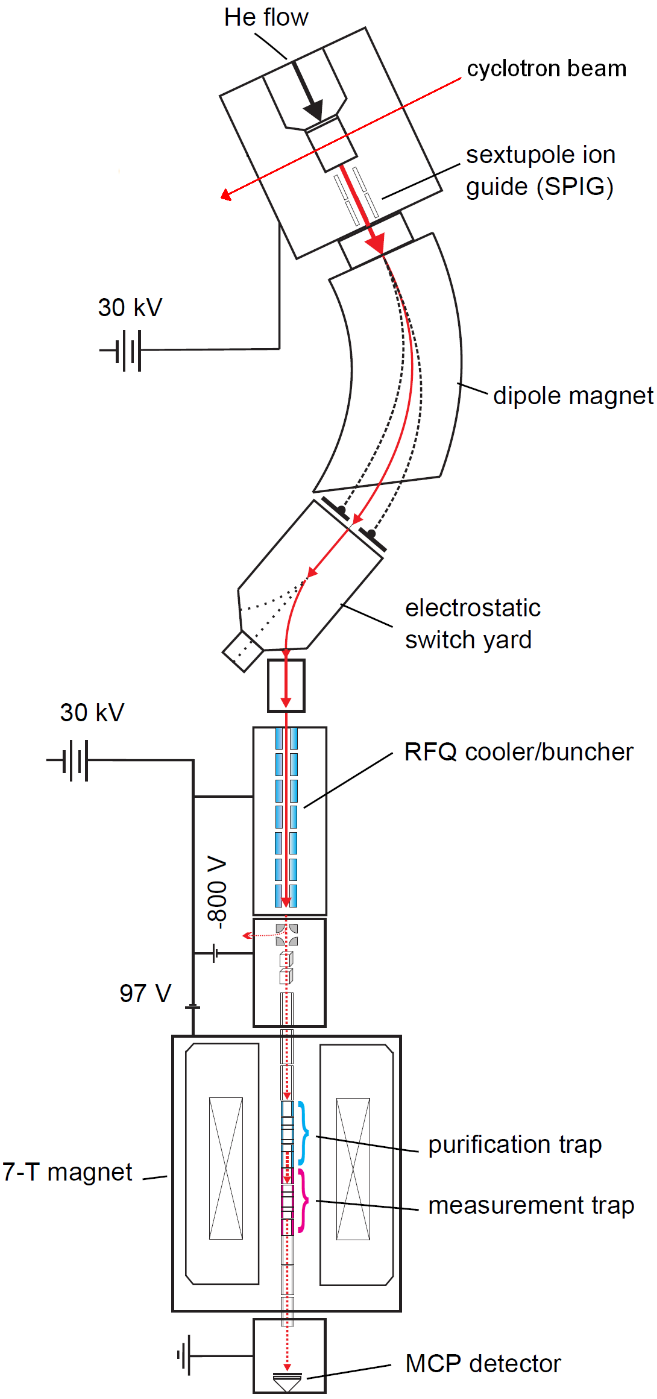

Figure 8: Layout of the IGISOL setup (old facility).

efficiency. The primary beam should be stopped but the largest possible share of the recoiling products should hit the entrance window between the beam stopper and the window frame. The cone covered by the primary beam and the recoiling products depends on the used beam, target and beam energy. The ratio of the scattered beam and recoiling products is approximately $\frac{Z_\mathrm{b}A_\mathrm{b}}{Z_\mathrm{c}A_\mathrm{c}}$ where b and c stand for the beam and compound nucleus. A typical HIGISOL efficiency is around 0.5 % [41].

3.3 JYFLTRAP Penning trap system

Yield determinations carried out in this work are based on measurements performed at the JYFLTRAP Penning trap. The JYFLTRAP system consisting of a radio-frequency quadrupole cooler and buncher (RFQ) and JYFLTRAP double Penning trap mass spectrometer is placed inside a high voltage cage. The beam is decelerated and injected into the radio-frequency quadrupole which is filled with helium gas at a pressure around 0.1 mbar [45]. Focusing into the quadrupole is achieved with an electrostatic lens system. The ions are confined to the trap with radio frequency electric field. In the RFQ, the ions are bunched: The ions cool down when colliding with the buffer gas atoms. When bunching, the voltage of a plate electrode at the end of the structure is kept high so that the ions cannot escape from the RFQ. Once a desired amount of ions has been gathered, the bunch is released by lowering the extraction voltage and the ions are re-accelerated.

The ions are injected into the first Penning trap, the purification trap. The Penning trap is an electromagnetic trap to which electrically charged particles are trapped by electric and magnetic fields [43]. The injection is done by adjusting the RFQ side potential wall. The Penning traps are inside a 7-Tesla superconducting solenoid. As well as the RFQ, also the purification trap is filled with helium gas at a low pressure of the order of 10^{-4} mbar. The ion motion in a Penning trap consists of three harmonic eigenmotions: an axial oscillation and two circular motions called magnetron and reduced cyclotron motions. The corresponding frequencies are denoted as ν_z, ν_- and ν_+ and the sum $\nu_- + \nu_+$ is the cyclotron frequency ν_c.

The determination of the ion yields is done with the purification trap. There, the ions collide with buffer gas atoms and lose kinetic energy. Cyclotron motion will cool down but magnetron motion will increase. An electric dipole excitation is switched on to increase the magnetron orbit of the ions so that the ions cannot escape through the small extraction. Magnetron frequency is almost mass independent so all ions are affected. A typical duration of the dipole excitation is around 10 ms. After, the magnetron motion of the ions of

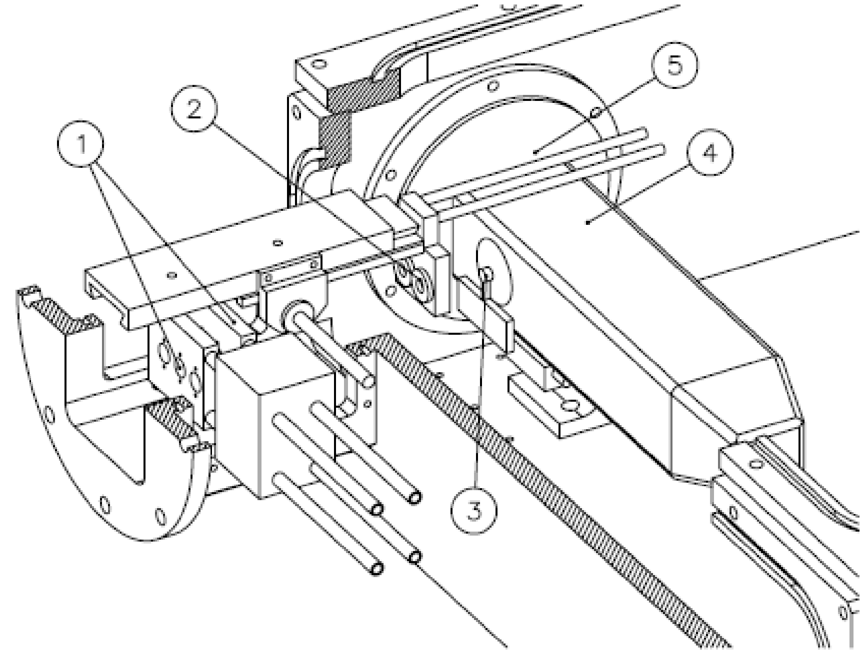

Figure 9: The HIGISOL set-up in Jyväskylä [41]. (1) Degraders, (2) targets, (3) beam stopper, (4) stopping chamber, (5) skimmer plate. Degraders can be used for fine tuning of the beam energy. The entrance window behind the beam stopper is made of havar.

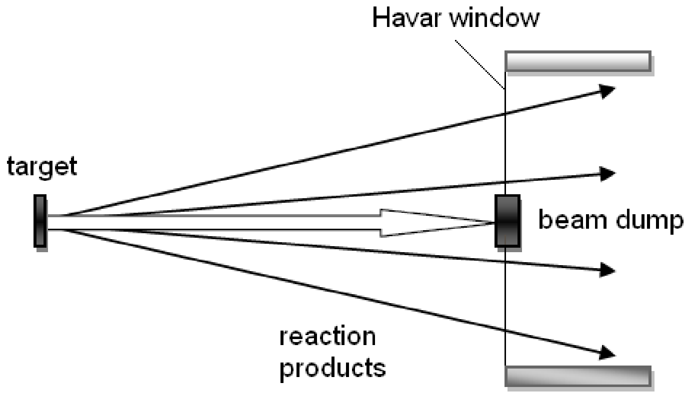

Figure 10: Shadow method takes advantage of the angular distribution of the reaction products.

interest is converted into cyclotron motion by applying a quadrupole excitation which is strongly mass dependent. Now the ions cool quickly in the buffer gas due to the fast cyclotron motion. A typical duration of the quadrupole excitation is 100-200 ms. When the ions have centered, the bunch can be extracted and thus the ions of interest have been separated [46]. The ion motion in the trap is visualized in Fig. 12. In purification trap measurements, the ions pass through the second Penning trap known as the presicion trap and fly straight to the micro-channel plate (MCP) detector. By measuring the number of detected ions at the MCP detector as a function of the applied quadrupole excitation frequency, ion yields belonging to different isobars can be determined. An example of a timing pattern of a single measurement cycle is shown in Fig. 13.

The data from the purification trap are needed to determine the yields of different isobars as well as to set correct frequencies for isobaric purification in the precision mass measurements. Mass and Q-value measurements are performed with the precision trap. The operation principle of the precision trap is similar to the purification trap but the precision trap is operated in vacuum in order to minimize damping forces. Usually one full conversion from magnetron motion to cyclotron motion is wanted and the excitation time and amplitude need to be chosen correctly. When the ions are extracted from the precision trap their magnetic moments interact with the magnetic field gradient and they gain axial energy. The ions fly to the MCP detector and the time-of-flight from the trap to the detector is measured. The ions with the most cyclotron motion will have most axial energy and therefore shortest time-of-flight. The cyclotron frequency can then be determined as the frequency that corresponds to the minimum time-of flight [47]. The mass of an ion is obtained

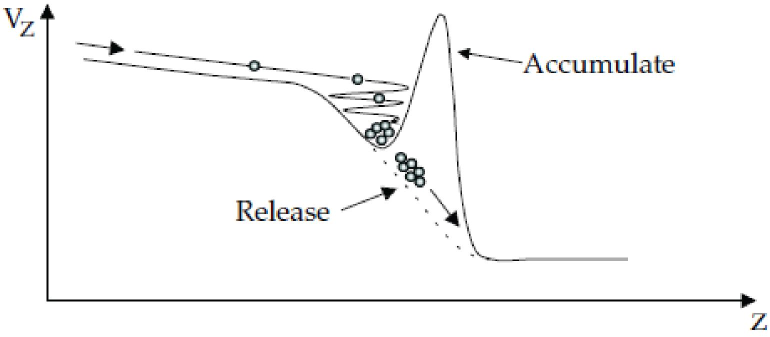

Figure 11: The ions are bunched in the RFQ [48].

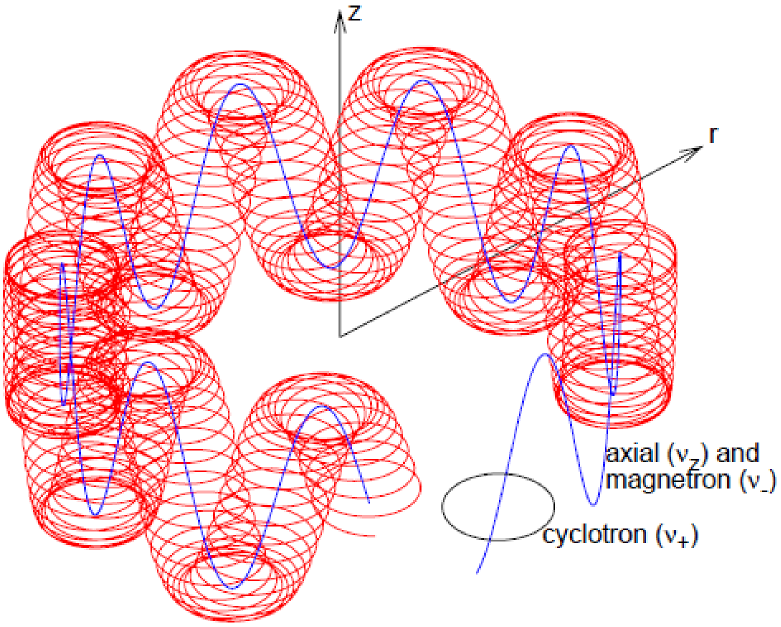

(a)

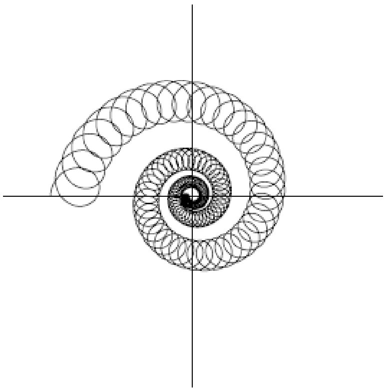

(b)

Figure 12: (a) The ion motion in a Penning trap consists of three eigenmotions [49]. The magnetic field is in the axial direction. (b) Quadrupole excitation can be used to convert the magnetron motion of the ions of interest into cyclotron motion. The ions whose cyclotron frequency corresponds to the excitation frequency will center and can be extracted [50].

via its cyclotron frequency

$$\nu_c = \frac{q}{2\pi m} B \,, \tag{1}$$

where ν_c is the cyclotron frequency, m the mass and q the charge of the ion in a magnetic field B.

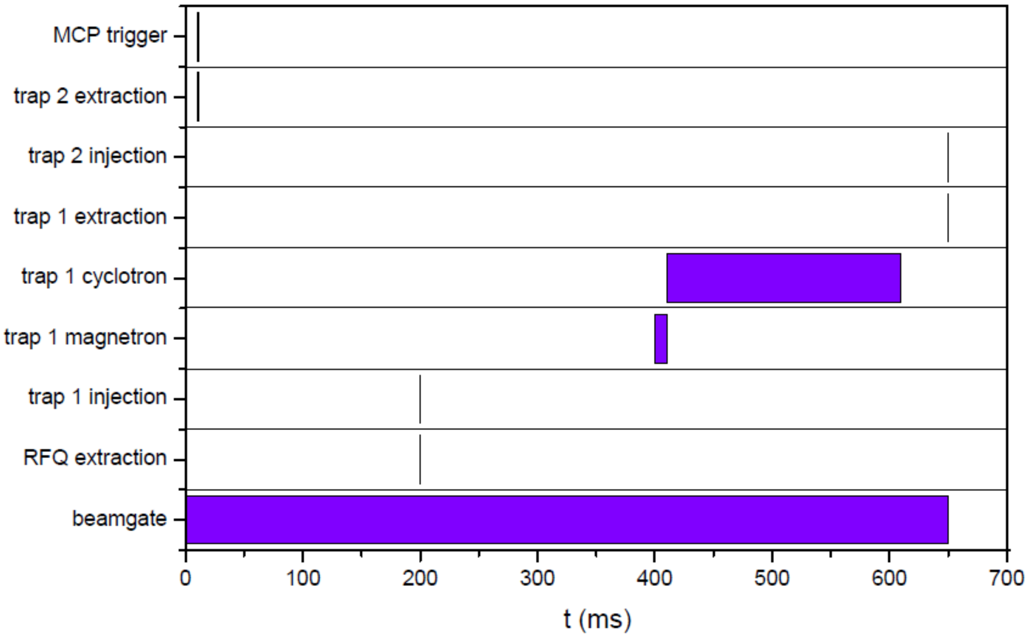

Figure 13: An example of a timing pattern used in a HIGISOL experiment in year 2007 for mass number A=110. The beamgate is open for 650 ms during each cycle. The collection of a new bunch of ions in the RFQ begins after 200 ms, after the extraction of the previous bunch. While a new bunch is collected in the RFQ, the previous bunch undergoes dipole and quadrupole excitations in the purification trap (400-610 ms). The ions of interest are then extracted through the precision trap and detected at the MCP detector between 10 and 11 ms. Thus, the duration of one cycle from collecting in the RFQ to detecting at the MCP detector is here approximately ((650-200)+650+10) ms = 1110 ms.

4 Analysis

The data were collected in five different measurements during the years 2005-2009. The measurements are labelled here as A, B, C, D and E. The data consisted of counts from the MCP detector versus excitation frequency.

4.1 Sorting of Data

To begin with, usable data had to be sorted out. The data were not collected for yield determination purposes but for the search of right purification trap frequencies for precise mass measurements in the second trap. Out of over 300 data files roughly 25 % were found to be suitable for further analysis. The files were opened with a software LAKRITSI which shows plots of time-of-flight and MCP counts against excitation frequency [49]. Time-of-flight and count windows in LAKRITSI were chosen so that all counts were included in the yield analysis. A typical useless piece of data was due to a short measurement time or a narrow frequency window. As a result, only a few counts or only a part of a peak could be detected. An example of good and eliminated pieces of data is given in Fig. 14.

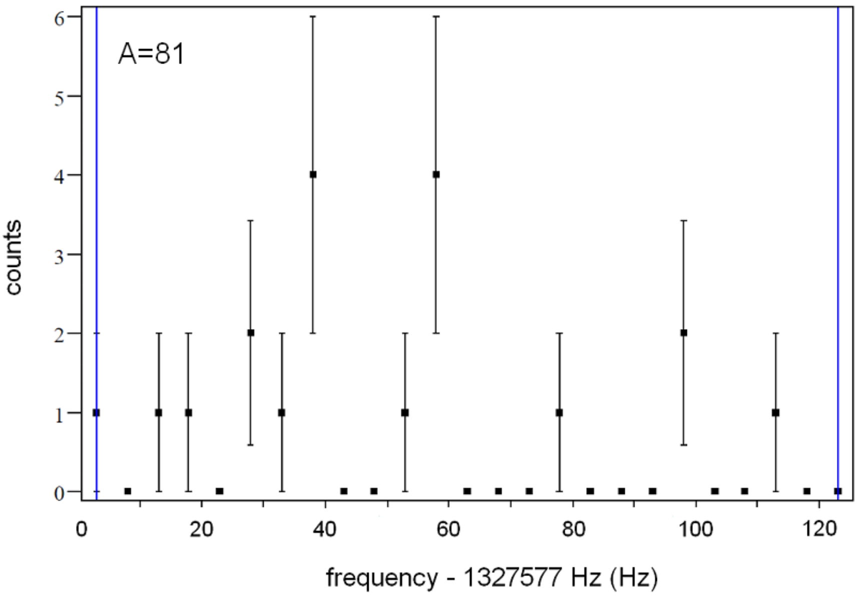

(a) The piece of data cannot be used. No clear peaks are seen.

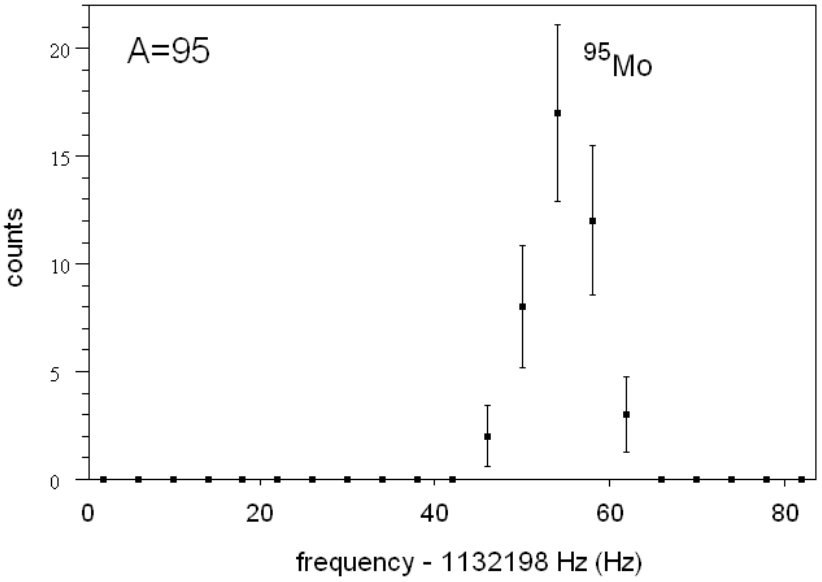

(b) The piece of data is usable but does not provide comprehensive information. The measurement window has been quite narrow and the data consist of only one peak with a few counts. With a wider frequency window and longer measurement time other peaks and a higher number of counts could have been observed.

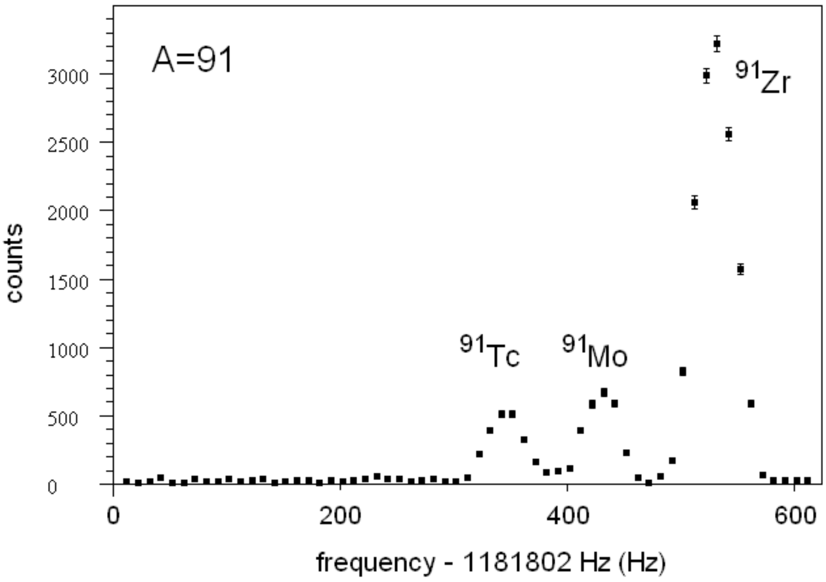

(c) An excellent piece of data for yield determination. Multiple peaks consisting of a large number of counts can be seen.

Figure 14: An example of data sorting: (a) useless, (b) usable and (c) excellent piece of data.

4.2 Fitting

Next, a Gaussian fit was done for every peak in the usable datasets. The Gaussian fit works well and was easy to perform with LAKRITSI. No remarkable differencies between the Gaussian fit and two alternative fit functions were observed in Ref. [51]. The height, background and the center of the peak were determined. Instead of the area of the peak, only the height was considered since the main interest was the yield at the center cyclotron frequency. The height corresponds now to the number of ions detected at the MCP detector. The peaks were then identified according to the center cyclotron frequencies.

4.3 Yield Determination

In order to determine the yields precisely, decay of the ions during the measurement must be considered [18]. When the beam gate is open, ions are collected to the RFQ at a constant production rate P. Simultaneous decay must be considered in the net rate. Thus the net rate is determined as the difference between the rate of production and the rate of decay:

$$\frac{\mathrm{d}N}{\mathrm{d}t} = P - \frac{\ln 2}{T_{1/2}} N = P - \lambda N \, . \tag{2}$$

The number of ions extracted from the RFQ:

$$N_{\mathrm{RFQ}} = N(t = t_{\mathrm{RFQ}}) = \frac{P}{\lambda}\left(1 - e^{-\lambda t_{\mathrm{RFQ}}}\right) \tag{3}$$

where t_{RFQ} is the duration of the collecting in the RFQ. After the ions leave the RFQ, ions are no more produced but the ions keep decaying according to $\mathrm{d}N/\mathrm{d}t = -\lambda N$. If N_{MCP} ions are detected at the MCP detector during n_{cycle} cycles,

$$\frac{N_{\mathrm{MCP}}}{n_{\mathrm{cycle}}} = N_{\mathrm{RFQ}} e^{-\lambda t_{\mathrm{trap}}} \tag{4}$$

where t_{trap} is the duration of the rest of the cycle. Finally, the production rate before the RFQ i.e. the yield per time unit can be calculated from equation

$$P = \frac{N_{\mathrm{MCP}} \cdot \lambda \cdot e^{\lambda t_{\mathrm{trap}}}}{n_{\mathrm{cycle}}(1 - e^{-\lambda t_{\mathrm{RFQ}}})} \, . \tag{5}$$

Here, the errors of λ, t_{trap} and t_{RFQ} are negligible compared to the error of N_{MCP}. The error of the production rate can thus be calculated as

$$\delta P = \left| \frac{\mathrm{d}P}{\mathrm{d}N_{\mathrm{MCP}}} \right| \delta N_{\mathrm{MCP}} \tag{6}$$

where δN_{MCP} is the error related to the height of the peak, given by the Gaussian fit [52].

The limited efficiency of the measurement set-up has been ignored in the calculation since it varies from experiment to experiment. The efficiency of HIGISOL is only around 0.5% [41], both RFQ and MCP detector of the order of 60% and JYFLTRAP about 17% [43]. Thus, to obtain efficiency-corrected yields before the RFQ, the results of this work should be multiplied by $\frac{1}{0.6}\frac{1}{0.6}\frac{1}{0.17} \approx 16$. In addition, the geometrical efficiency of HIGISOL has been ignored in the cross-section calculations. The angular distribution of the recoiling products and thus the efficiency of HIGISOL depends on the reaction channel. For example, ^{91}Tc is produced via ^{58}Ni(^{40}Ca,5p2n)^{91}Tc but also via ^{60}Ni(^{40}Ca,5p4n)^{91}Tc.

4.4 Cross-section Modelling

For comparison, fusion-evaporation application PACE4 of the LISE package [53,54] was used to determine theoretical cross sections for the reactions of interest. The PACE calculation of the de-excitation of the excited nuclei is based on JULIAN - the Hillman–Eyal evaporation code [54,55]. Partial cross section σ_l at angular momentum l is

$$\sigma_l = \pi \chi^2 (2l+1) T_l \tag{7}$$

where χ is the reduced wavelength and the maximum angular momentum of the evaporation residues l_{max} with a diffuseness parameter Δ gives

$$T_l = \left(1 + \exp \frac{l - l_{\text{max}}}{\Delta}\right)^{-1} . \tag{8}$$

The total fusion cross section σ_F determines the maximum angular momentum since

$$\sigma_F = \sum_{l=0}^{\infty} \sigma_l . \tag{9}$$

Several de-excitation events are processed with a Monte-Carlo procedure.

Projectile, target and beam energy were entered to the program and 100 000 de-excitation cascades were chosen to be used in the Monte Carlo simulations. A lower limit of 0,01% was set for the residual yields. Otherwise the default settings of the program were used. Calculations were performed around the beam energies used in the experiments [24,25,26] and the results were plotted according to mass numbers (see Figs. 17-19 and 22). Errors given by the code were not plotted since without errorbars the plots are more readable and the effect of a change in the beam energy on cross sections can be seen more easily. Also, the systematic error related to the code is unknown and could easily be bigger than the error given by the code. The PACE4 calculations are based on AME2003 masses from the year 2003 [23]. Penning-trap experiments have revealed large deviations to the AME2003 values for example for Nb, Mo and Tc [24,25,28,30]. These can have an effect on cross-section calculations as shown in Ref. [20]. There, cross-section calculations were performed based on the AME2003 mass table corrected with JYFLTRAP mass results. When the cross sections were compared to calculations based on uncorrected AME2003 values, remarkable differencies were seen especially for ^{85}Nb, ^{86}Nb and ^{88}Tc.

The PACE4 code was chosen to be used in this work since it was easily available. There are also other suitable codes for fusion-evaporation calculations. ALICE91 is one of the commonly used codes [56,57,58]. A new ALICE2011 version is also available [59]. In addition, codes such as CASCADE [60], JOANNE [61] or HIVAP [62] can be used. Another modified version of the JULIAN code can be found from Ref. [63].

5 Yields and Cross Sections of HIGISOL Experiments

5.1 Measurement A - December 2005

In 2005 the masses of $^{80-83}$Y, $^{83-86,88}$Zr and $^{85-88}$Nb were measured and $^{96-98}$Mo were used as references. In these measurements a 135-170 MeV ^{32}S beam was used in combination with a ^{54}Fe or ^{nat}Ni target [24]. Calculated yields, corresponding cross-sections and half-lives are presented in Tables 2 and 3. Half-lives were taken from Ref. [64]. In the calculation of total cross sections for ^{nat}Ni target, only ^{58}Ni and ^{60}Ni were taken into account. These isotopes cover 94% of ^{nat}Ni [1]. Heavy-ion fusion-evaporation reactions of the other stable Ni isotopes (^{61}Ni, ^{62}Ni and ^{64}Ni) produce less neutron-deficient nuclei or the calculated cross sections for the products of interest are small. Thus, they are not interesting for the measurements discussed here.

In 2005, most of the ions were measured as oxides. The production of those ions that were detected as oxides as well as of ^{78,80}Rb and ^{78}Kr is in a rough agreement with the theoretical cross sections (see Figs. 17-18). However, the yields of the ions detected as oxides are very modest. As illustrated in Fig. 15, for ^{86}Zr^{16}O and ^{86}Nb^{16}O the smallest yield corresponds to the highest cross section. The amplitudes of the wide ^{86}Nb^{16}O peaks were relatively small, only a few dozen counts. The cross sections given by the PACE4 code may be incorrect since the new mass value of ^{86}Nb differs by 701(90) keV from the AME2003 value [24]. In Ref. [20], cross-section calculations with new mass values for reaction p+^{92}Mo gave a lower cross section for ^{86}Nb. Tuning of the HIGISOL set-up, including change in the target position, was done before the measurement at a beam energy of 170 MeV. This makes comparison with the measurements at beam energies 135 and 150 MeV difficult.

The files contained ^{96,98,100}Mo. These stable or long-lived Mo isotopes originate from the Havar window which consists typically 2-3% of ^{nat}Mo [2]. Peaks corresponding to the cyclotron frequencies of $^{81-82}$Kr and ^{78}Se were also observed. These disagree with PACE4 calculations. It is possible that the identification of the peaks has failed, perhaps due to several close peaks merged together although the FWHM values of the fittings did not differ from common fitting values. Recorded target nuclei or beam energies may also be incorrect because there were some difficulties to find out the used targets and beam energies from old notes for this pioneering experiment. ^{82}Kr and ^{78}Se are stable and ^{81}Kr has a long half-life so they could come from the set-up. Kr

---

[1] ^{58}Ni: 68.0769% ; ^{60}Ni: 26.2231% ; ^{61}Ni: 1.1399% ; ^{62}Ni: 3.6345% ; ^{64}Ni: 0.9256% .

[2] ^{92}Mo: 14.77% ; ^{94}Mo:9.23% ; ^{95}Mo: 15.90% ; ^{96}Mo: 16.68% ; ^{97}Mo: 9.56% ; ^{98}Mo: 24.19% ; ^{100}Mo: 9.67%.

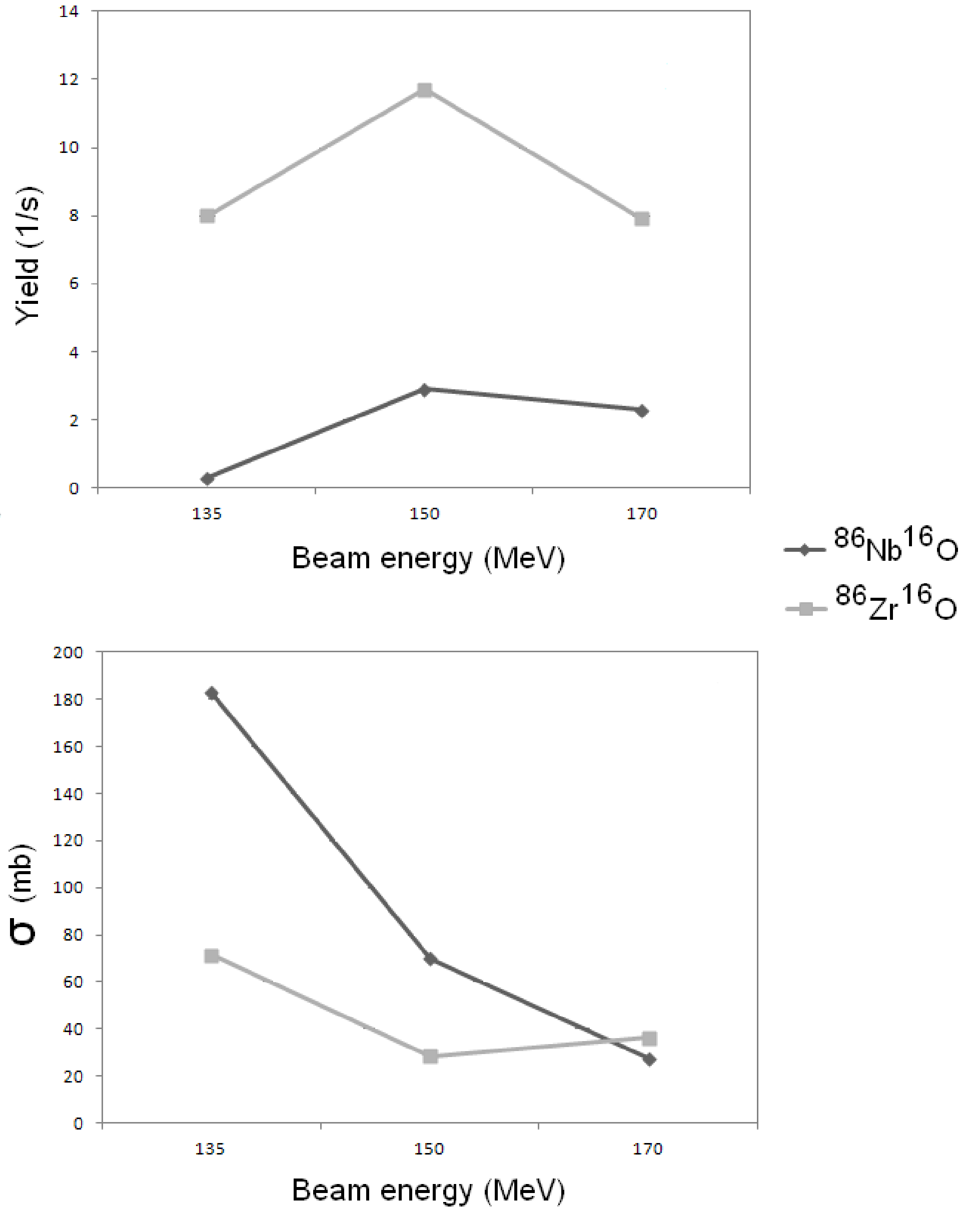

Figure 15: Yields and cross sections of $^{86}Zr^{16}O$ and $^{86}Nb^{16}O$ in the measurement A. The chemical properties of Nb and Zr as well as the bond enthalpies for NbO (771.5 kJ/mol [65]) and ZrO (776.1 kJ/mol [65]) are very similar. Therefore, the difference between the calculated cross sections and the observed yields is not explained by chemistry.

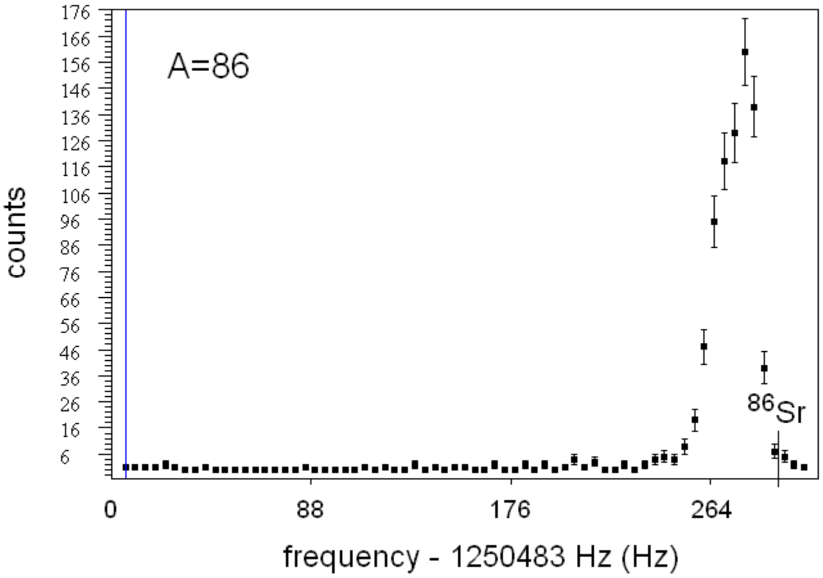

Figure 16: A mystery peak that could not be identified was detected in the measurement A.

gas is sometimes injected to IGISOL system to provide mass calibration for the dipole magnet.

A mystery peak with a beam energy of 135 MeV and the Ni target was found at a center frequency 1250793.9181 Hz. The frequency matches with ^{86}Rb but this is not supported by cross-section calculations and experimental conditions. Again, the shape of the peak (see Fig. 16) indicates that the peak could consist of two close peaks but still no reasonable nuclei can be identified in that frequency area. Out of the nuclei in Fig. 17 (g), the cyclotron frequency of stable ^{86}Sr is close to the center frequency of the peak but ^{86}Sr has no calculated cross section at a beam energy of 135 MeV. According to cross-section calculations, A=70 nuclei should not be produced with the Ni target but these oxides (e.g. ^{70}Se^{16}O) were still checked. In order to find a match, more rare possibilities such as ^{68}ZnH$_2$O and ^{172}Yb^{2+} were also checked but no match was found.

Table 2: Ion yields for ^{32}S beam on a $^{\mathrm{nat}}$Ni target in the measurement A. Half-lives $T_{1/2}$ and calculated cross sections σ_{PACE4} are also shown. Different rows in the ion yield for a given isotope refer to different measurement files. The ions that were detected in the same file are connected with lines.

Beam energy (MeV)	Produced ion	$T_{1/2}$	Yield (1/s)	σ_{PACE4} (mb)
170	^{100}Mo	$7.3 \cdot 10^{18}$ y	7.5(0.7)	– [a]
170			12(3)	– [a]
170	^{98}Mo	stable	45(2)	– [a]
150			80(10)	– [a]
135			350(30)	– [a]
150	^{96}Mo	stable	27(3)	– [a]
150	^{87}Zr^{16}O	1.68 h	3.4(0.8)	54.8(0.4) [b]
135			0.9(0.4)	33.0(0.3)
150	^{87}Nb^{16}O	3.75 m	2.9(0.7)	38.6(0.4)
135			3.8(0.5)	19.7(0.3)
170	^{86}Zr^{16}O	16.5 h	7.9(0.5)	36.2(0.4)
150			11.7(1.1)	28.6(0.5)
135			8(1)	71.5(0.7)
170	^{86}Nb^{16}O	88 s	2.3(0.3)	27.4(0.4)
150			2.9(0.6)	69.8(0.7)
135			0.3(0.1)	182.8(1.1)
170	^{82}Y^{16}O	8.30 s	2.4(0.5)	126(1)
150	^{82}Sr^{16}O	25.55 d	9(5)	61.2(0.7)
135	^{82}Kr	stable	5100(300)	–
170	^{80}Rb	33.4 s	12(2)	9.5(0.2)

a. Mo isotopes originate from the Havar window.

b. Cross section exists only for ^{60}Ni.

Table 3: Ion yields for ^{32}S beam on ^{54}Fe in the measurement A.Different rows in the ion yield for a given isotope refer to different measurement files. The ions that were detected in the same file are connected with lines.

Beam energy (MeV)	Produced ion	$T_{1/2}$	Yield (1/s)	σ_{PACE4} (mb)
170	^{98}Mo	stable	24.3(1.4)	– [a]
170	^{81}Kr	$2.29 \cdot 10^5$ y	293(6)	–
160			410(10)	–
170	^{78}Se	stable	2(1)	–
170			25.0(1.4)	
170	^{78}Kr	$\geq 2.3 \cdot 10^{20}$ y	61(2)	38.4(0.7)
170	^{78}Rb	17.66 m	27.2(1.4)	169(2)
170			26.8(1.4)	

a. Mo isotopes originate from the Havar window.

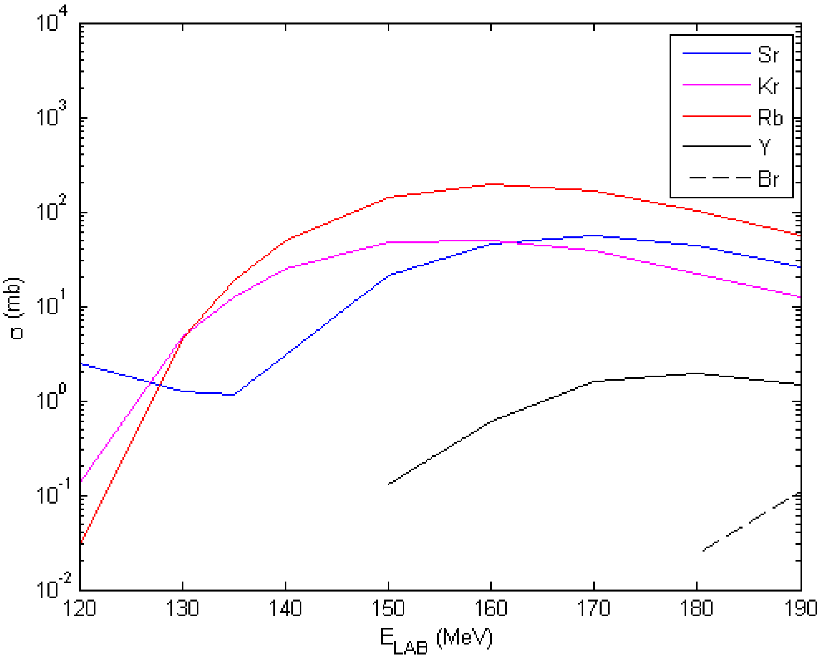

(a) A=78.

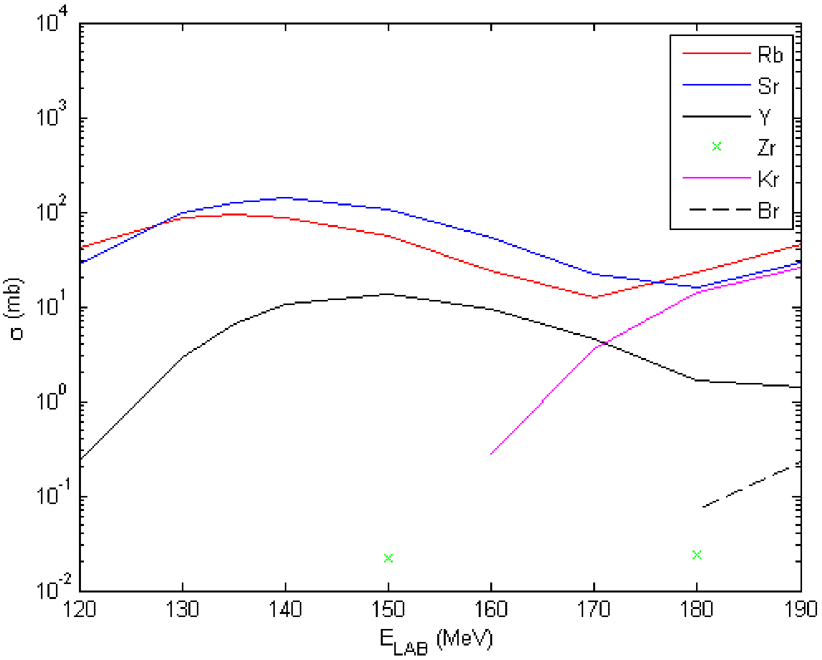

(b) A=79.

Figure 17: PACE4 cross sections for ^{32}S beam on a ^{54}Fe target.

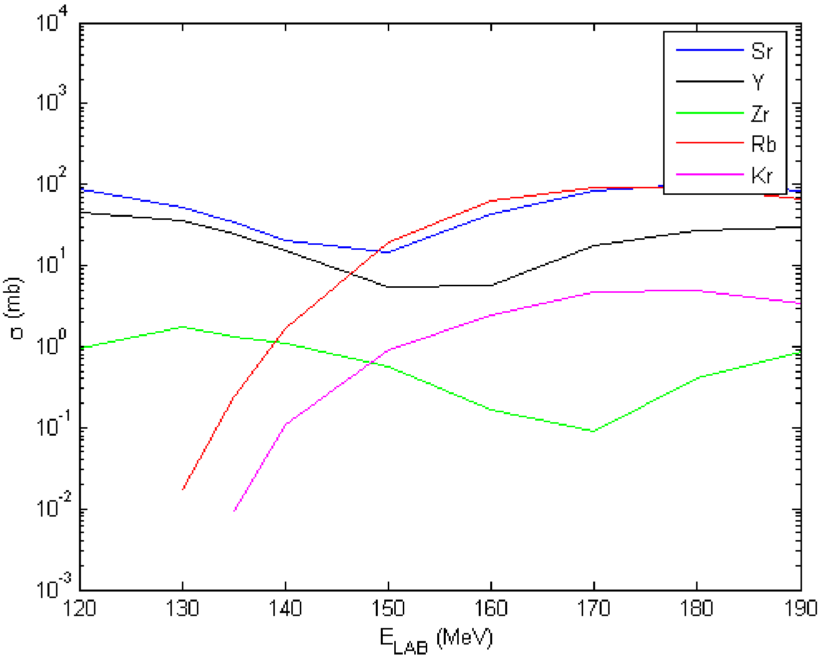

(c) A=80.

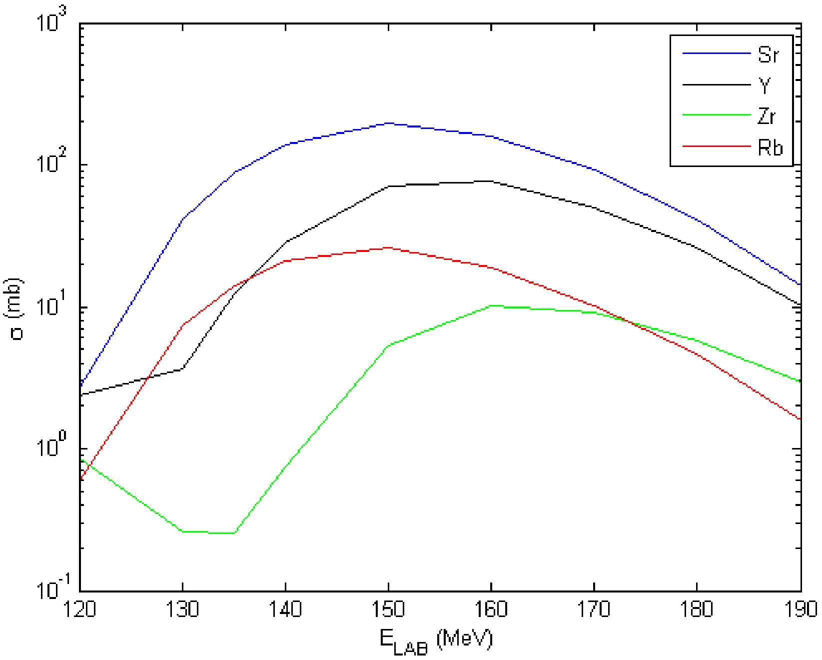

(d) A=81.

Figure 17: PACE4 cross sections for ^{32}S beam on a ^{54}Fe target.

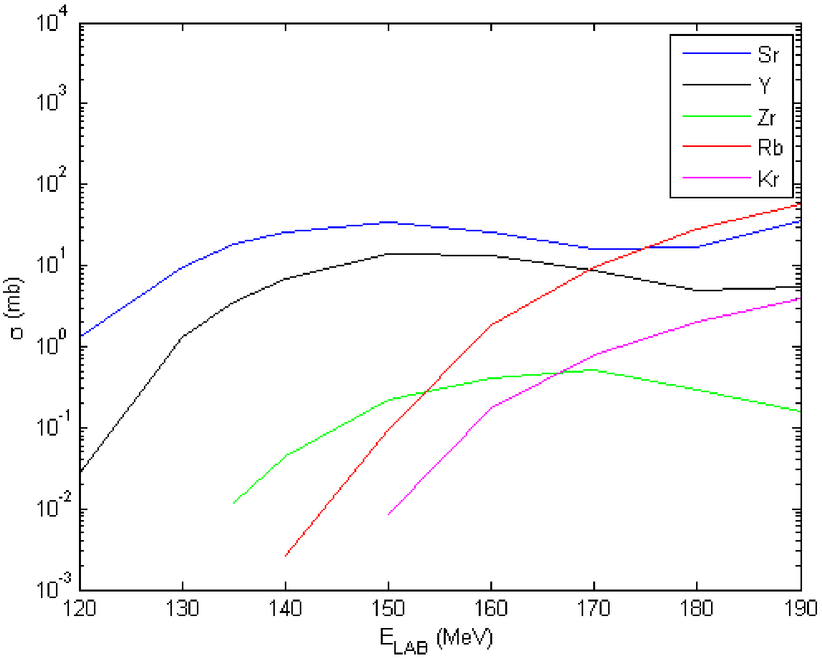

(a) A=80.

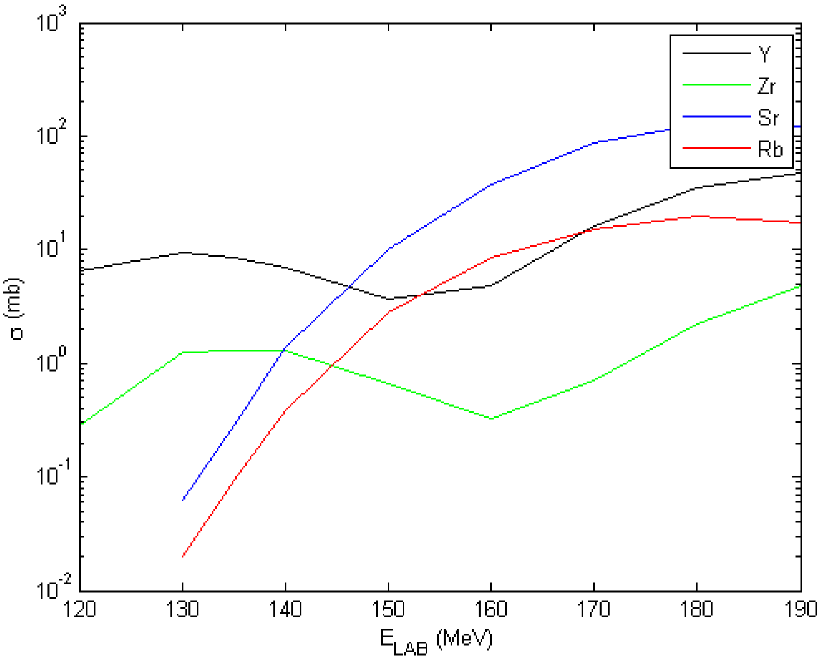

(b) A=81.

Figure 18: PACE4 cross sections for ^{32}S beam on a ^{nat}Ni target.

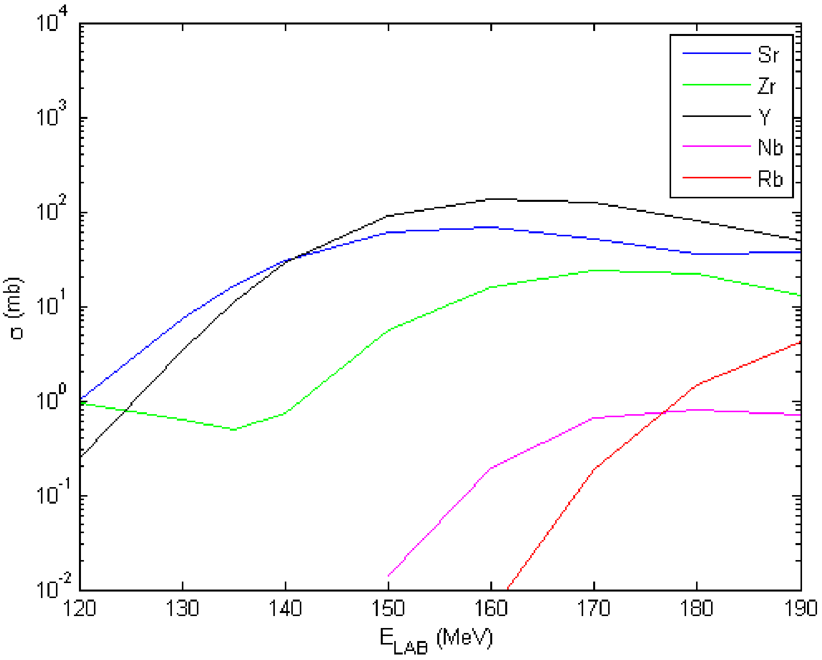

(c) A=82.

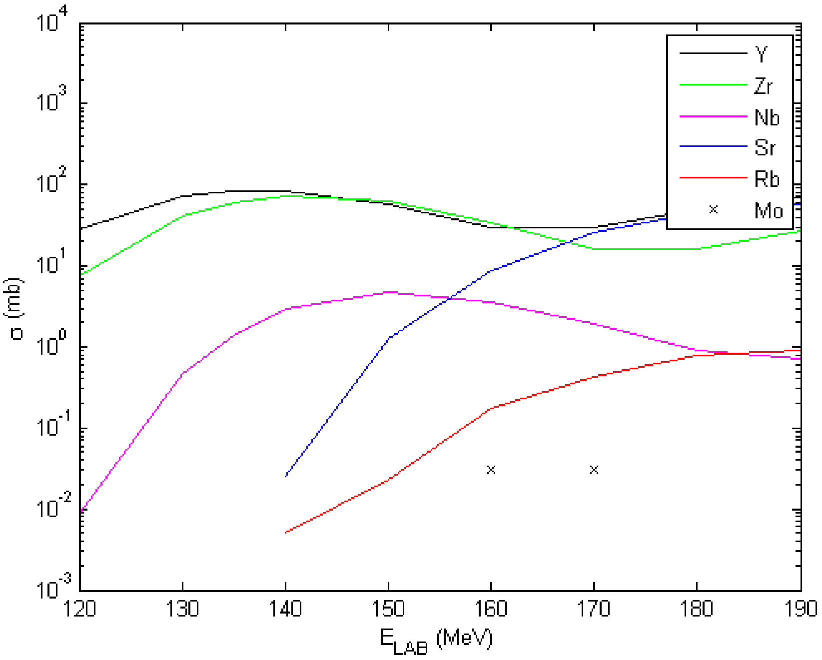

(d) A=83.

Figure 18: PACE4 cross sections for ^{32}S beam on a ^{nat}Ni target.

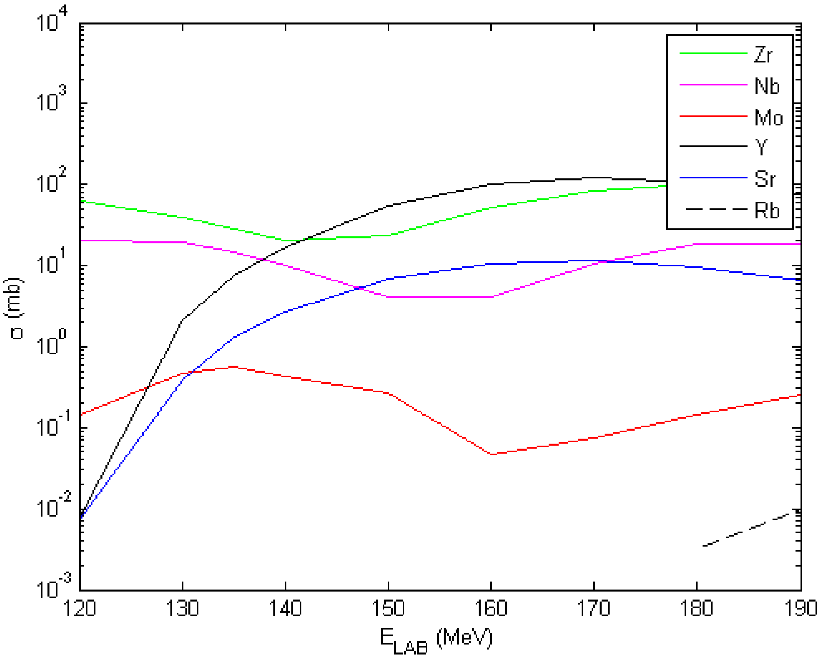

(e) A=84.

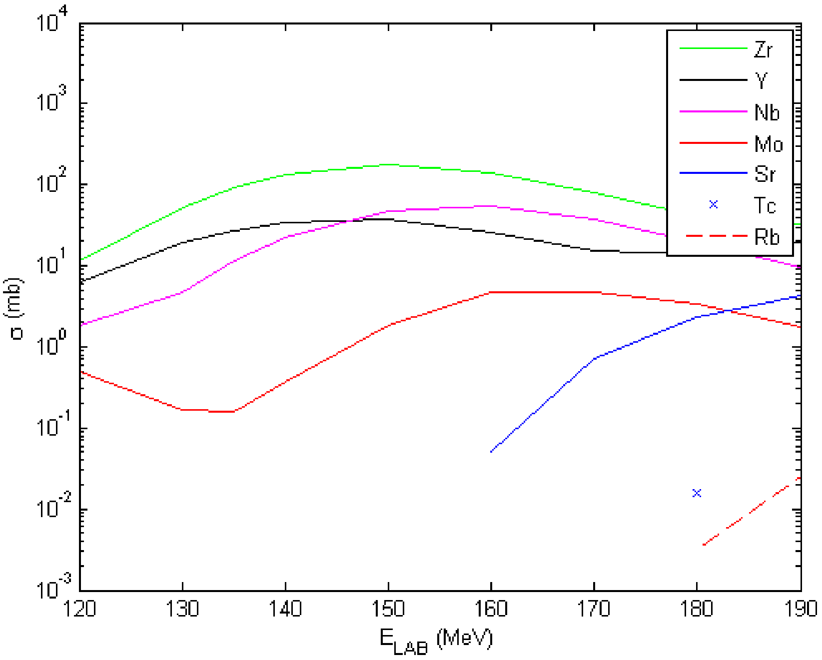

(f) A=85.

Figure 18: PACE4 cross sections for ^{32}S beam on a ^{nat}Ni target.

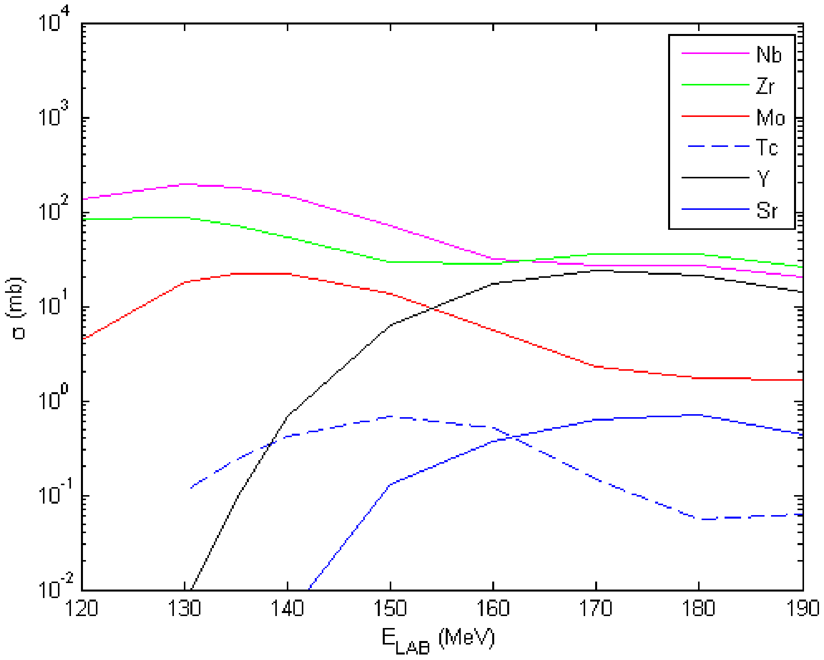

(g) A=86.

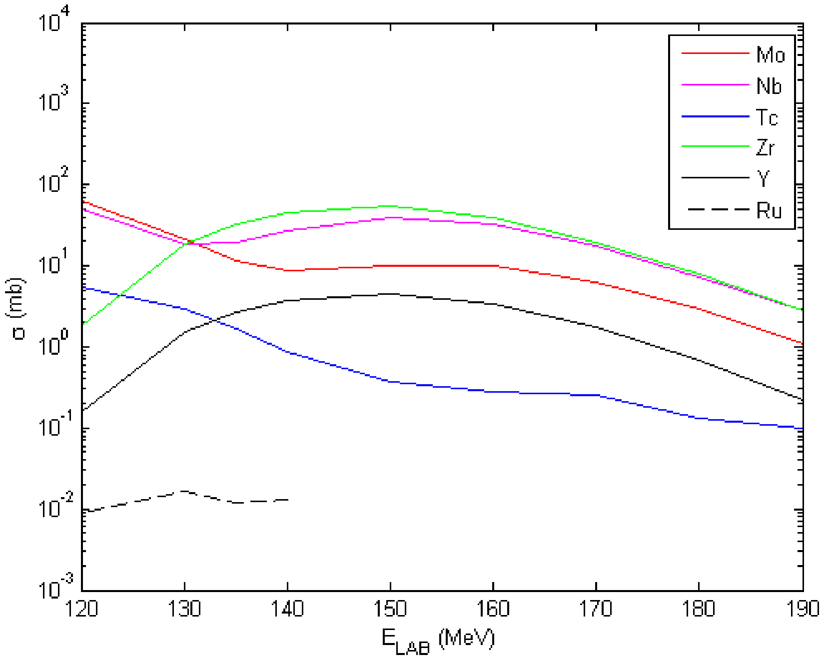

(h) A=87.

Figure 18: PACE4 cross sections for ^{32}S beam on a ^{nat}Ni target.

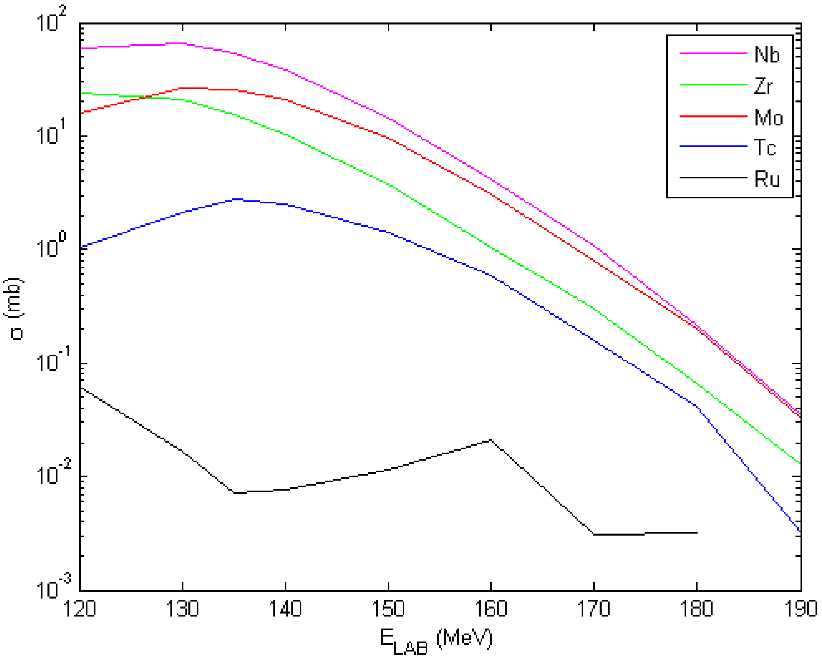

(i) A=88.

Figure 18: PACE4 cross sections for ^{32}S beam on a ^{nat}Ni target.

5.2 Measurement B - August 2006

The second measurement consisted of mass determinations of ^{84}Y, ^{87}Zr, ^{89}Mo, $^{89-90,92}$Tc, $^{90-94}$Ru and $^{92-95}$Rh. A 3.6 mg/cm^2-thick ^{nat}Ni target was used with a 189-220 MeV ^{40}Ca or 222 MeV ^{36}Ar beam [25]. However, no usable data for yield calculations were collected with ^{36}Ar beam.

Yields are collected in Table 4. The results agree roughly with cross sections shown in Fig. 19. In addition, a peak at a frequency of 1169025.5528 Hz was identified as ^{92}Ru but no reasonable fitting could be done due to small number of counts. The ions with low calculated cross sections were not detected in the collected mass spectra. However, the measurements were not aimed to calculate yields. Perhaps, if the data were collected for a longer time, also smaller yields could have been determined. Again, $^{94-95}$Mo have mainly originated from the Havar window. The significantly large yield of ^{87}Rb can be explained by the rubidium salt added for reference purposes. Namely, ^{85}Rb (ME = -82167.331(0.011) keV [23]) and ^{87}Rb (ME = - 84597.795(0.012) keV [23]) are commonly used as references in Penning trap mass measurements. Several reference measurements of ^{85}Rb were made during the measurement B.

When the ion yields are compared to cross sections, the ratio of ^{91}Mo to ^{91}Tc sticks out. The yield of ^{91}Tc is significantly larger than the yield of ^{91}Mo although the cross section of ^{91}Mo is slightly larger. The yields of ^{91}Mo, ^{91}Tc and ^{91}Ru were determined from the same file so the difference cannot be explained by different measurement conditions. The problem could lie in the PACE4 code or in the HIGISOL set-up although the ion-guide method should be independent of the chemical properties of the isotopes. ^{91}Nb did not fit to the used frequency window. A surprisingly large yield of stable ^{89}Y was also detected. An yttrium filament had been used for testing the ion guide in the previous experiment at IGISOL [66].

There is a large drop in the yields of ^{94}Mo and ^{94}Ru which were detected in pairs except for the odd Mo yield of 298 ions per second. The measurement B suffered from problems and a lot of tuning of the SPIG, cyclotron beam, He-pressure etc. had to be done during the measurement. This could also explain why for example the yield of ^{89}Mo is only twice as big as the yield of ^{96}Rh although the calculated cross section is almost hundred times larger. Based on cross sections, lower beam energies could have produced better yields for mass numbers A=94 and A=96 whereas the beam energy of 220 MeV used otherwise could have served better also for A=91.

Table 4: Ion yields for ^{40}Ca beam on a $^{\mathrm{nat}}$Ni target in the measurement B. Different rows in the ion yield for a given isotope refer to different measurement files. The ions that were detected in the same file are connected with lines.

Beam energy (MeV)	Produced ion	$T_{1/2}$	Ion yield ($1/\mathrm{s}$)	σ_{PACE4} (mb)
189	^{96}Rh	9.90 m	6.9(0.8)	0.92(0.06) [b] (
220	^{95}Mo	stable	457(5)	– [a]
220	^{94}Mo	stable	380(5)	0.034(0.011) [a,b]
			44(3)	
			298(4)	
	^{94}Ru	51.8 m	97(3)	26.6(0.3)
			13.4(1.4)	
	^{94}Rh	70.6 s	7(8)	8.8(0.2)
220	^{92}Mo	stable	56(2)	54.2(0.7) [a]
			450(7)	
	^{92}Tc	4.25 m	20(2)	127(1)
			43(3)	
189	^{91}Mo	15.49 m	20.7(1.5)	24.5(0.3)
	^{91}Tc	3.14 m	96(3)	18.8(0.4)
	^{91}Ru	7.9 s	6.0(1.4)	9.3(0.3)
220	^{90}Mo	5.56 h	470(30)	39.3(0.5)
			510(20)	
	^{90}Tc	8.7 s	102(13)	26.1(0.5)
			120(10)	
220	^{89}Y	stable	910(10)	0.034(0.011) [b,c]
			651(5)	
	^{89}Nb	2.03 h	4.2(0.7)	47.6(0.6)
	^{89}Mo	2.11 m	13(3)	90.1(0.9)
220	^{87}Rb	$4.81\cdot10^{10}$ y	47000(700)	– [d]

a. Stable Mo isotopes originate also from the Havar window.

b. Cross section exists only for ^{60}Ni.

c. Yttrium filament had been used for testing the ion guide.

d. Rubidium salt had been added for reference purposes.

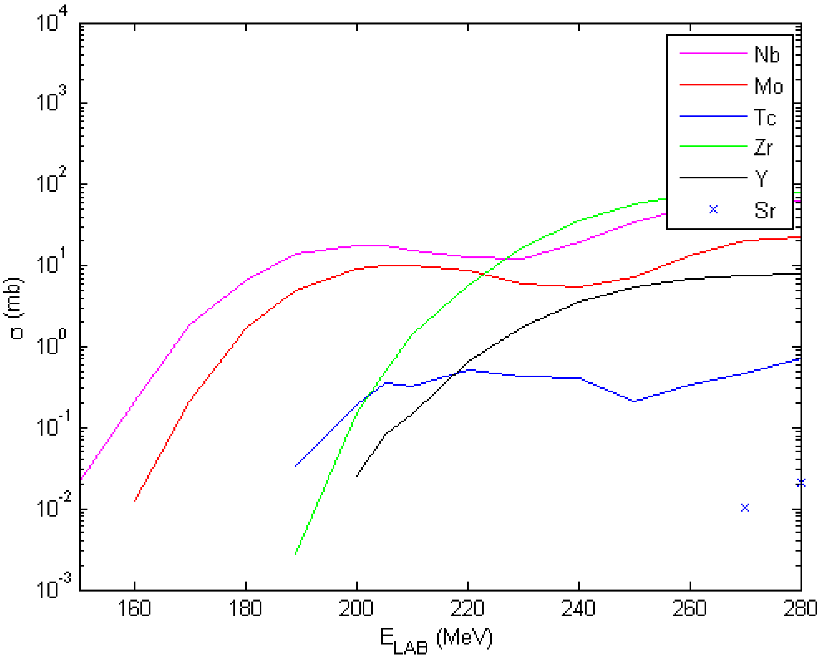

(a) A=87.

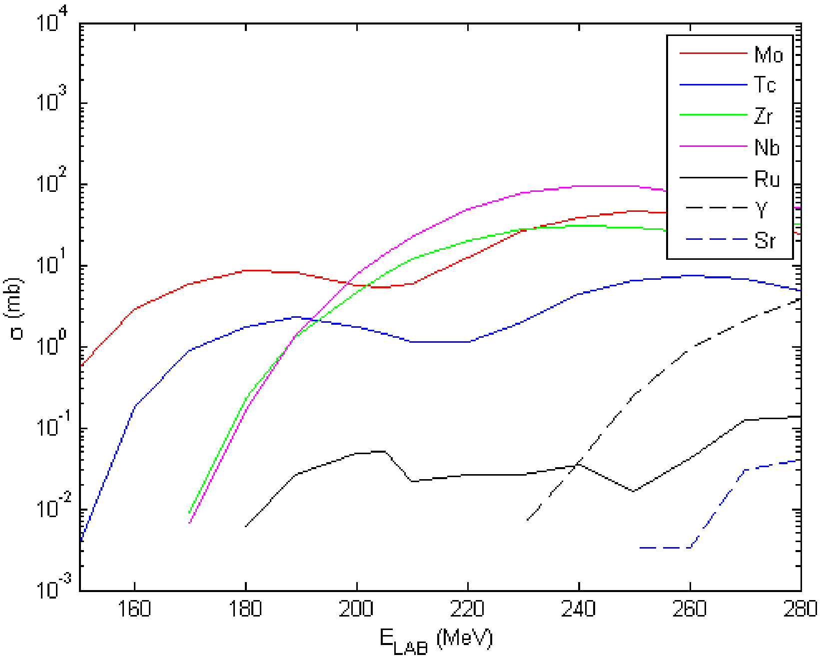

(b) A=88.

Figure 19: PACE4 cross sections for ^{40}Ca beam on a ^{nat}Ni target.

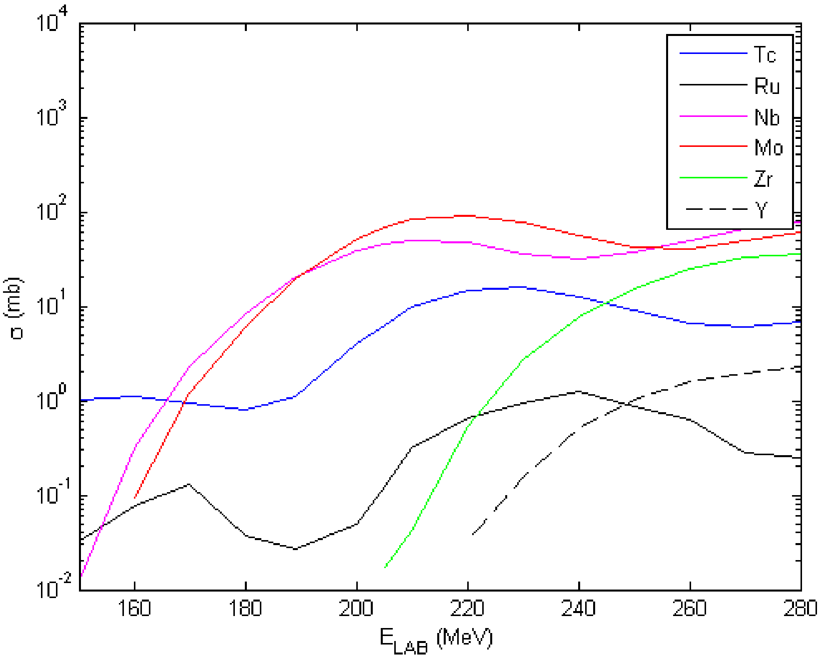

(c) A=89.

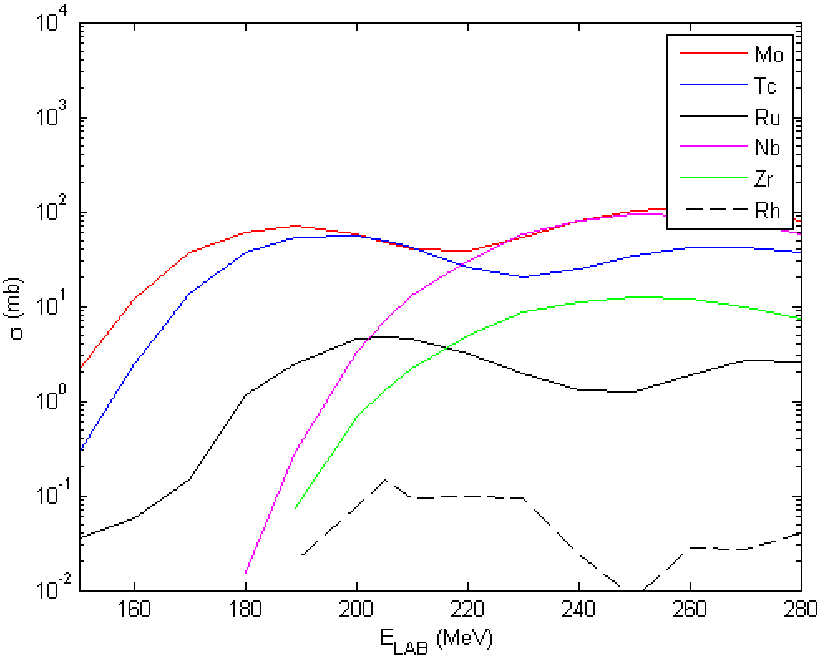

(d) A=90.

Figure 19: PACE4 cross sections for ^{40}Ca beam on a ^{nat}Ni target.

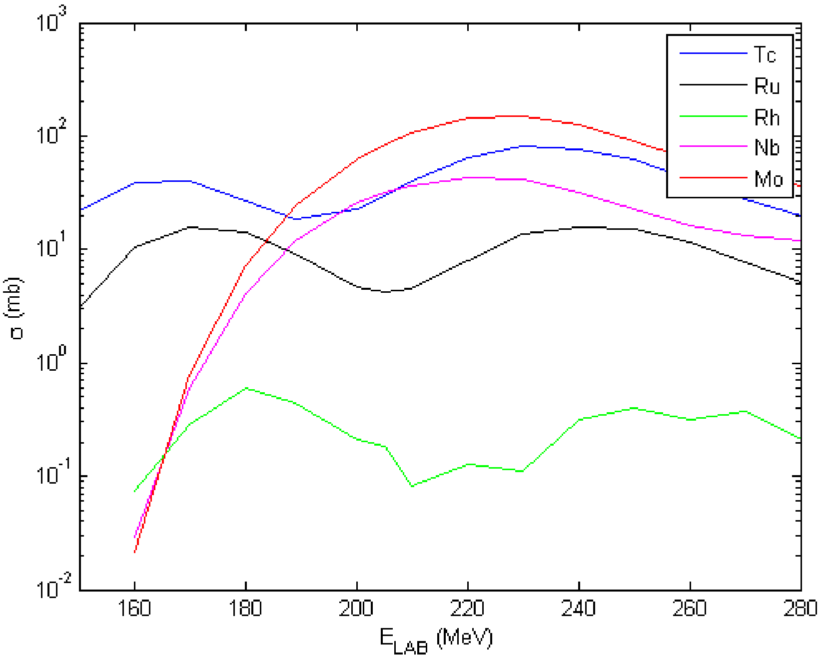

(e) A=91.

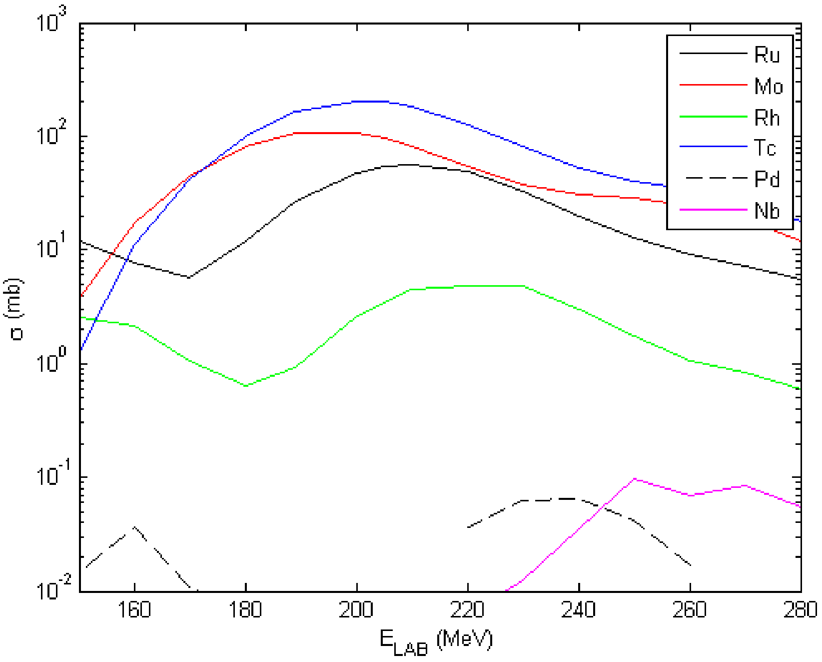

(f) A=92.

Figure 19: PACE4 cross sections for ^{40}Ca beam on a ^{nat}Ni target.

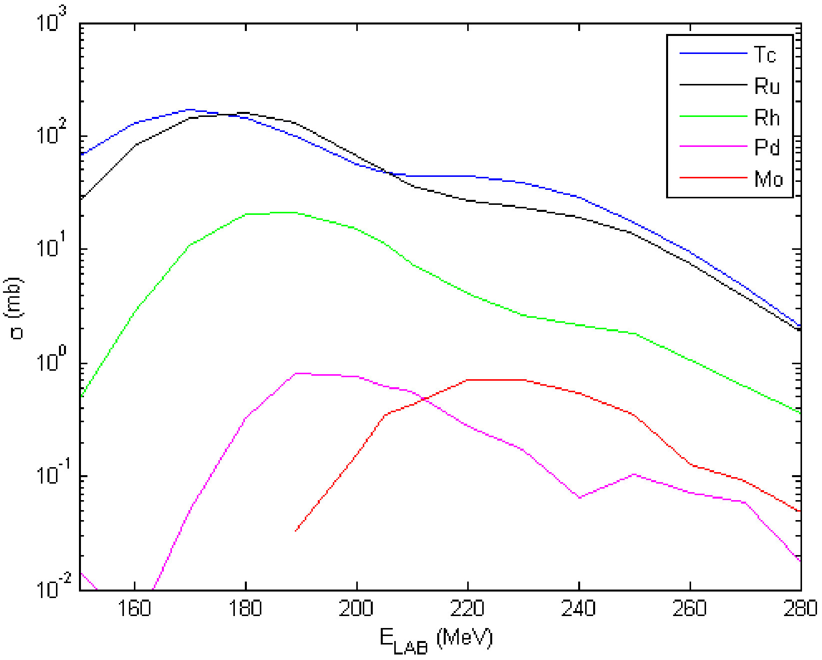

(g) A=93.

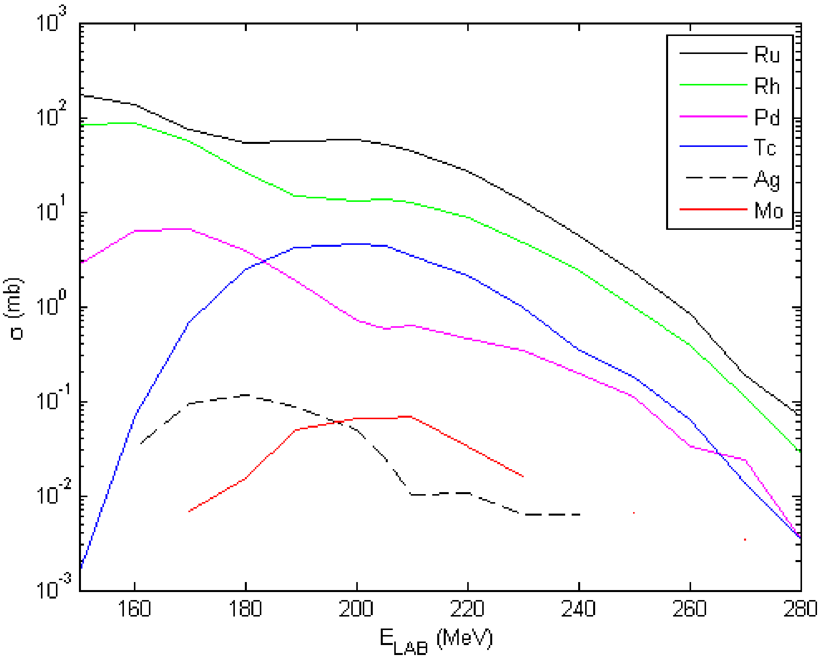

(h) A=94.

Figure 19: PACE4 cross sections for ^{40}Ca beam on a ^{nat}Ni target.

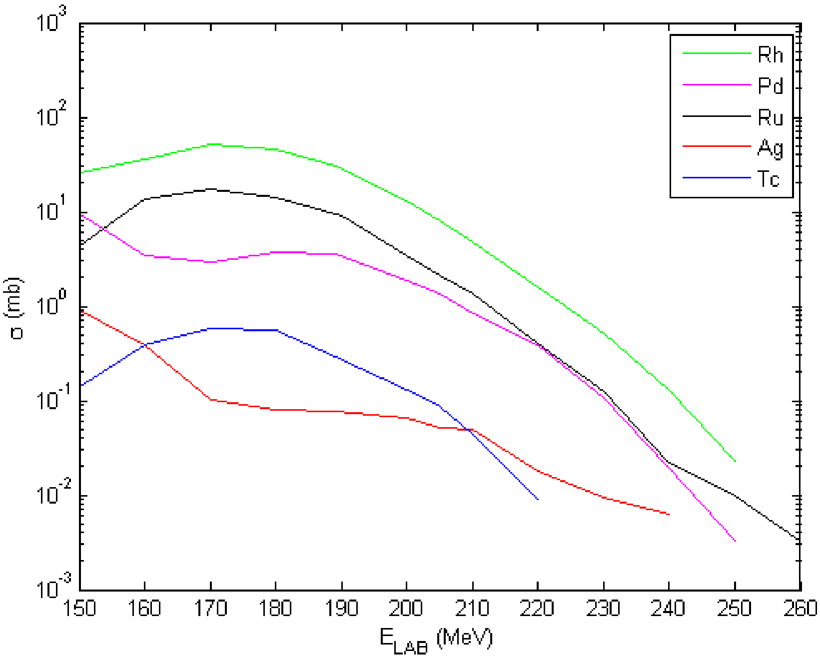

(i) A=95.

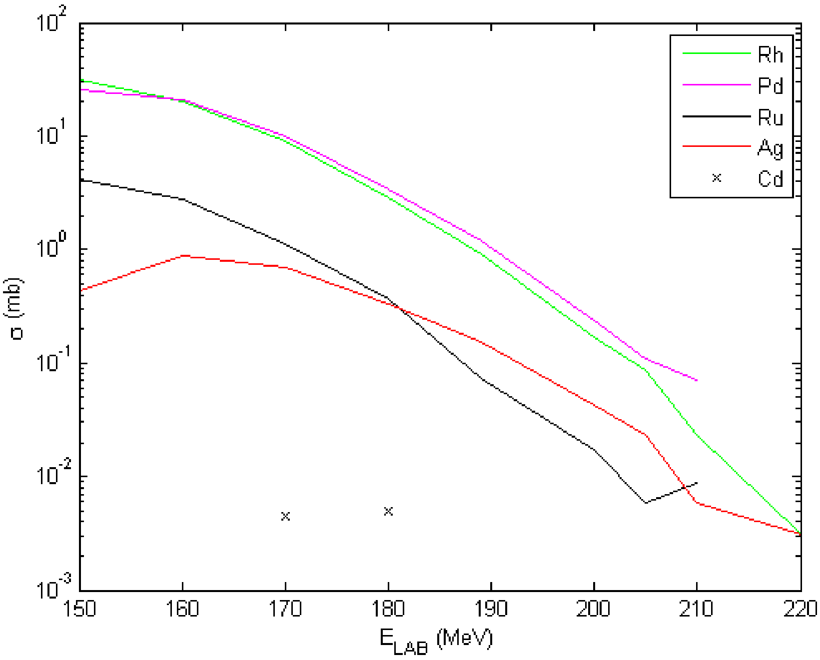

(j) A=96.

Figure 19: PACE4 cross sections for ^{40}Ca beam on a ^{nat}Ni target.

5.3 Measurement C - December 2006

This measurement was a continuation of the measurement B with a 170-205 MeV ^{40}Ca beam on a ^{nat}Ni target [25]. Isotopes $^{94-96}$Pd, together with the isomeric state ^{95}Pd^{m} and ^{91}Tc were measured. The isotope ^{91}Ru was remeasured.

Calculated yields in Table 5 are in a rough correspondence with the cross sections of Fig. 19. The large variations in the yields of ^{93}Tc and ^{93}Ru show that it is worthwhile to aim for the best conditions (see Fig. 20). For example, the yield of ^{93}Ru varied from 4.4 to 890 ions per second depending on experimental conditions. ^{93}Tc and ^{93}Ru were detected in pairs, in two of these measurement files also ^{93}Rh could be detected. Buffer gas was changed from He to Ar in two of these measurements. Due to the change, yield of ^{93}Tc dropped from 239 to 39.6 ions per second. A higher yield of 208 ions per second was retaken with He gas. The yields of ^{93}Tc and ^{93}Ru are higher at a beam energy of 190 MeV than at 205 MeV which agrees with the cross-section modellings albeit different trap settings were also used. The timing pattern and trap settings were not changed between the measurements with a certain beam energy. Again, the ratio of yields of ^{91}Mo and ^{91}Tc is opposite to the ratio of cross sections (see Fig. 21). As discussed in Subsection 5.2, the PACE4 code might fail at this mass region or the measurement set-up suffers from problems in ^{91}Mo production. ^{91}Nb did not fit to the chosen frequency window.

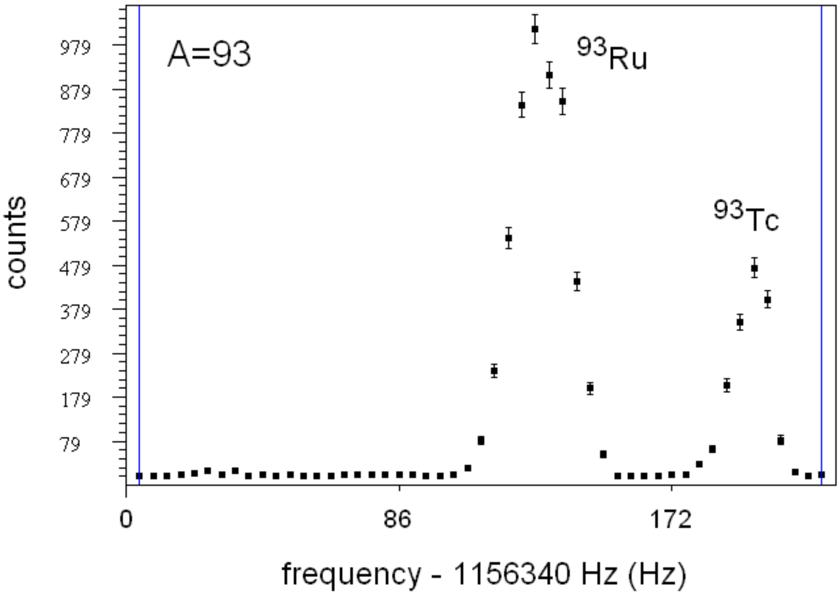

(a) ^{93}Tc and ^{93}Ru were detected in pairs i.e. two peaks were seen in one measurement file.

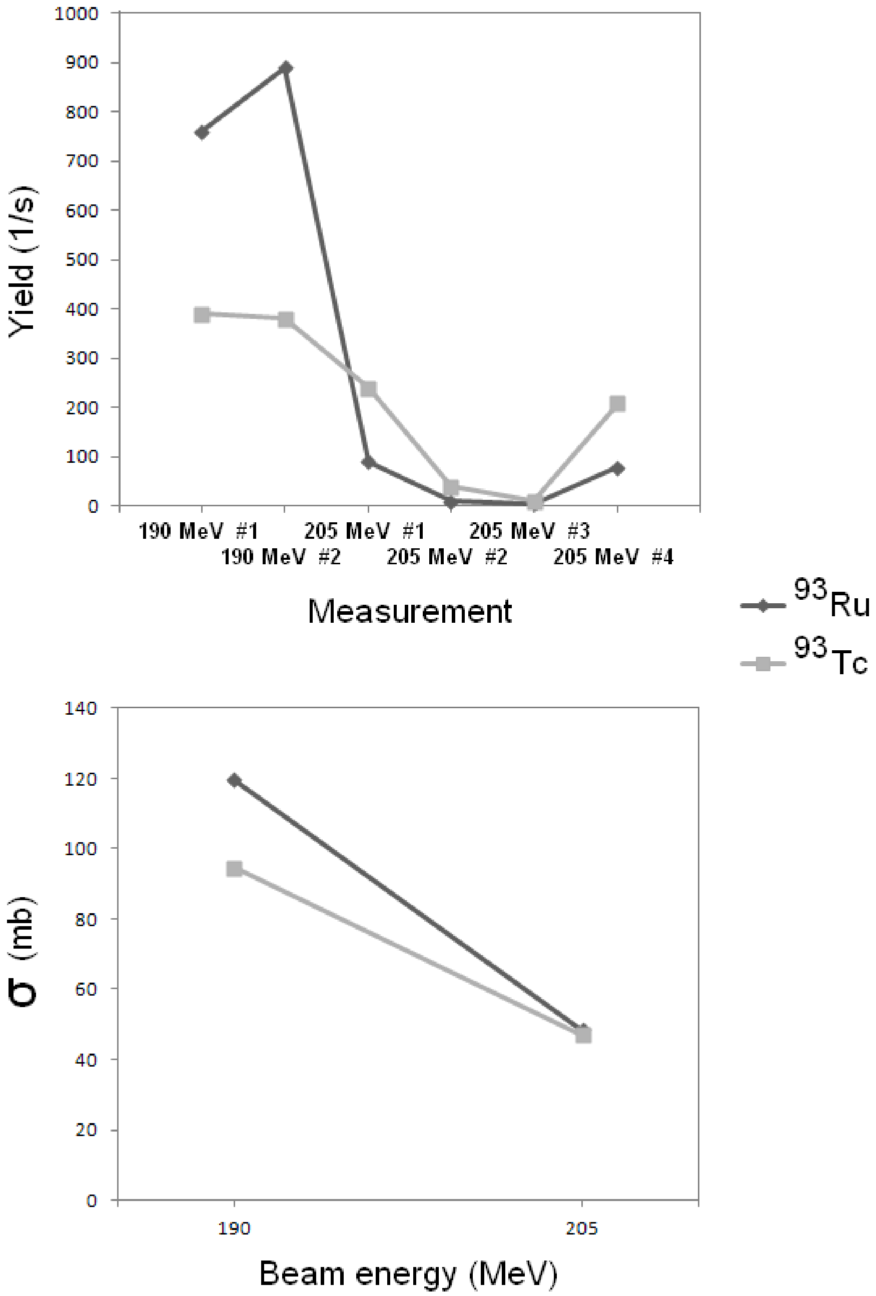

(b) The yields of ^{93}Tc and ^{93}Ru varied during the measurement C.

Figure 20: The observed yields of ^{93}Tc and ^{93}Ru show that it is worthwhile to aim for the best conditions.

Table 5: Ion yields for ^{40}Ca beam on a $^{\mathrm{nat}}$Ni target in the measurement C. Different rows in the ion yield for a given isotope refer to different measurement files. The ions that were detected in the same file are connected with lines.

Beam energy (MeV)	Produced ion	$T_{1/2}$	Ion yield ($1/\mathrm{s}$)	σ_{PACE4} (mb)
190	^{96}Mo	stable	6690(90)	– [a]
170	^{95}Mo	stable	1020(30)	– [a]
190			11(5)	– [a]
170	^{94}Mo	stable	435(11)	0.007(0.004) [a,b]
	^{94}Ru	51.8 m	26(3)	74.6(0.7)
			29(3)	
	^{94}Rh	70.6 s	37.8(1.4)	56.7(0.6)
			5.7(1.4)	
			4.8(1.4)	
			3.3(0.8)	
			8(2)	
			10(2)	
190	^{93}Tc	2.75 h	390(20)	94.6(0.8)
190			380(14)	
205			239(4)	47.0(0.6)
205			39.6(1.4)	
205			9.7(0.8)	
205			208(3)	
190	^{93}Ru	59.7 s	760(20)	119.6(0.9)
190			890(20)	
205			90(3)	48.5(0.6)
205			9.0(1.4)	
205			4.4(0.5)	
205			78(2)	
205	^{93}Rh	11.9 s	4(2)	11.3(0.3)
205			4.3(0.6)	
205	^{91}Mo	15.49 m	33(2)	85.0(0.7)
			28(2)	
	^{91}Tc	3.14 m	85(3)	29.5(0.4)
			76(3)	

a. Stable Mo isotopes originate from the Havar window.

b. Cross section exists only for ^{60}Ni.

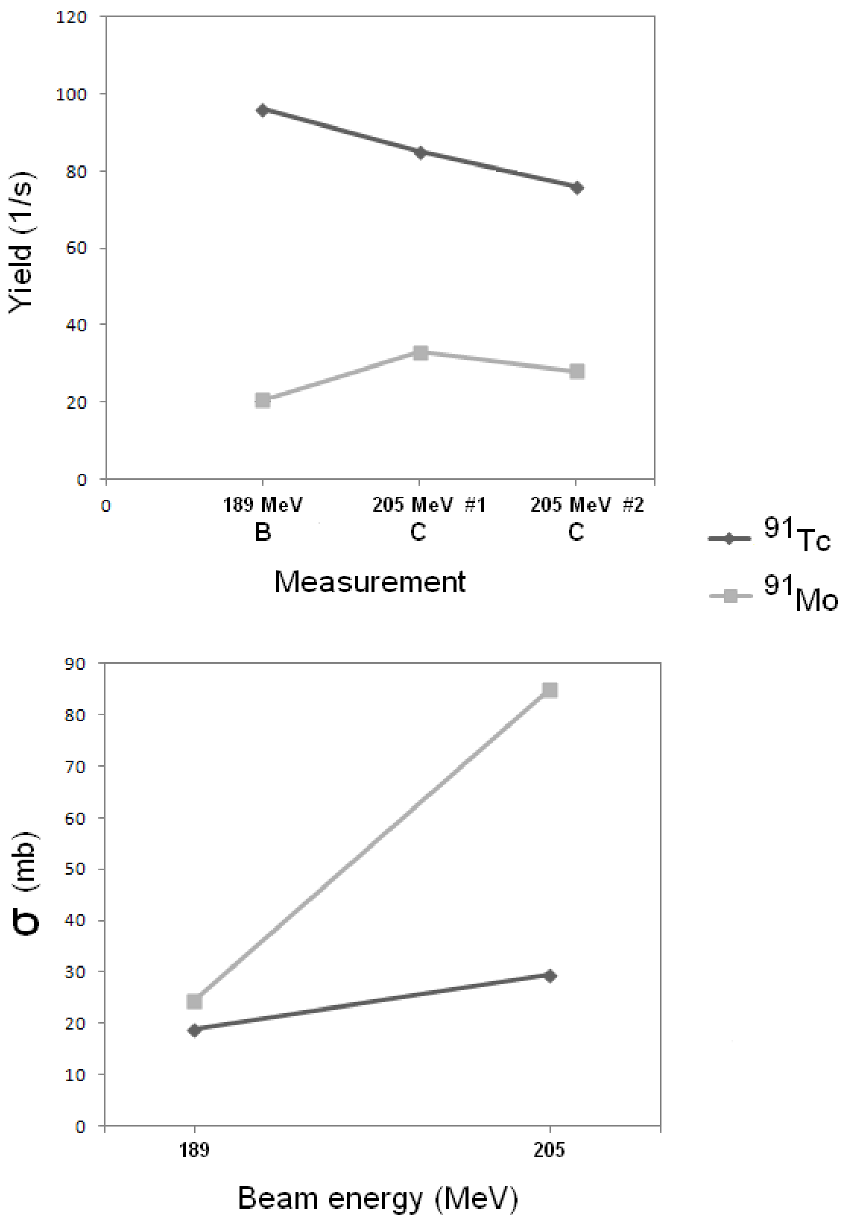

Figure 21: The ratio of yields of ^{91}Mo and ^{91}Tc was opposite to the ratio of cross sections in the measurements B and C.

5.4 Measurement D - December 2007

In 2007, the mass values of $^{104-108}$Sn, $^{106-110}$Sb, $^{108-109}$Te and ^{111}I were measured with a 295-330 MeV ^{58}Ni beam and a 4 mg/cm^{2}-thick ^{nat}Ni target [26]. In this measurement, 4.5 mg/cm^{2}-thick Havar window was used.

The yields for this measurement are given in Table 6. The calculated cross sections are shown in Fig. 22. As can be seen from Table 6, the measurement conditions have been stable since the yields did not vary much from measurement to measurement. ^{111}Sb and ^{111}Te as well as ^{110}Sb and ^{110}Te were detected as two peaks in a single measurement file.

The ion yields agree roughly with cross sections. The ions with low calculated cross sections were not detected. Tin is not detected for mass numbers 110-111 because it did not fit to the used frequency window. There is a large yield of ^{107}Ag which is not supported by cross-section calculations. ^{107}Ag had recently been used for tuning in the previous experiment at IGISOL. As a stable nucleus, ^{107}Ag does not decay away from the system.

The yield ratios at a certain mass number A do not agree with cross section ratios. For example at A=105, the production of both ^{105}Sn and ^{105}Cd has been extremely minimal although the cross section of ^{105}Cd is over three times larger than of ^{105}Sn. Perhaps the cross sections given by the PACE4 code are incorrect. New mass excess value of ^{105}In differs by 160(20) keV and of ^{105}Sn by 78(80) keV from the AME2003 values [23,67]. The yield of stable ^{106}Cd is rather high compared to the other nuclei. Unlike ^{106}In and ^{106}Sn, ^{106}Cd was detected as a single peak in different measurement conditions.

Table 6: Ion yields for ^{58}Ni beam on a ^{nat}Ni target in the measurement D. Different rows in the ion yield for a given isotope refer to different measurement files. The ions that were detected in the same file are connected with lines.

Beam energy (MeV)	Produced ion	$T_{1/2}$	Ion yield ($1/s$)	σ_{PACE4} (mb)
330	^{111}Sb	75 s	26(1)	3.1(0.1)
	^{111}Te	19.3 s	19.8(0.9)	1.14(0.07)
330	^{110}Sb	23.0 s	35.6(1.5)	3.63(0.15)
			34.2(1.4)	
			36.3(1.4)	
			34.3(1.3)	
	^{110}Te	18.6 s	7.6(0.7)	2.18(0.13)
			7.6(0.7)	
			7.7(0.7)	
			7.5(0.6)	
330	^{108}Sn	10.30 m	45(2)	37.2(0.4)
			37.3(1.2)	
	^{108}Sb	7.4 s	12.6(1.1)	4.03(0.14)
			9.5(0.7)	
			10.4(0.5)	
			10.0(0.5)	
			10.5(0.5)	
			12.9(0.6)	
295	^{107}Ag	stable	14000(200)	– [a]
295	^{106}Cd	stable	116(3)	13.2(0.3)
330	^{106}In	6.1 m	6.3(0.5)	90.1(0.8)
330	^{106}Sn	115 s	4.8(0.4)	42.0(0.6)
330	^{105}Cd	55.5 m	0.7(0.2)	30.0(0.4)
	^{105}In	5.07 m	15.9(0.6)	41.5(0.5)
			10.9(0.8)	
	^{105}Sn	34 s	1.0(0.1)	8.8(0.3)
			1.0(0.2)	
			1(2)	

a. The yield is explained by the previous IGISOL experiment.

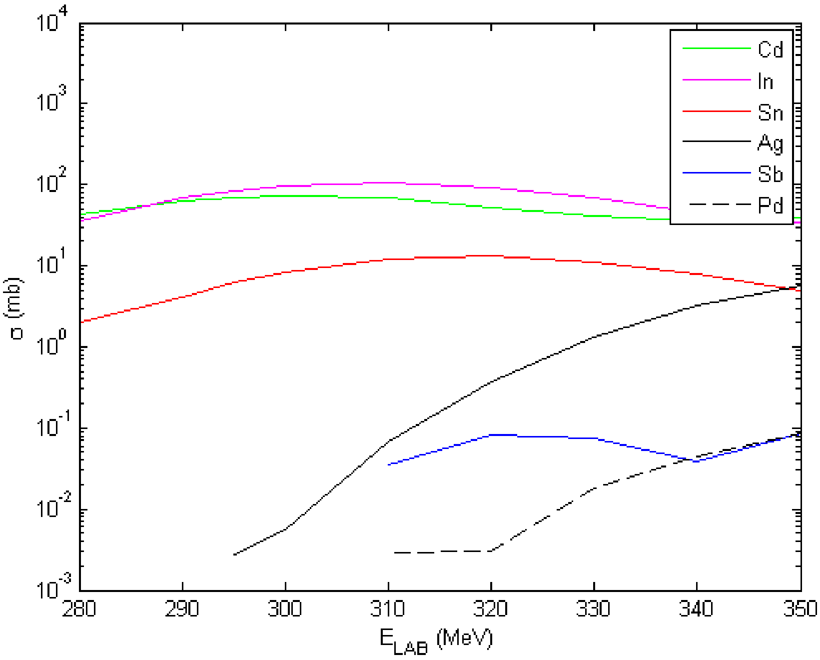

(a) A=104.

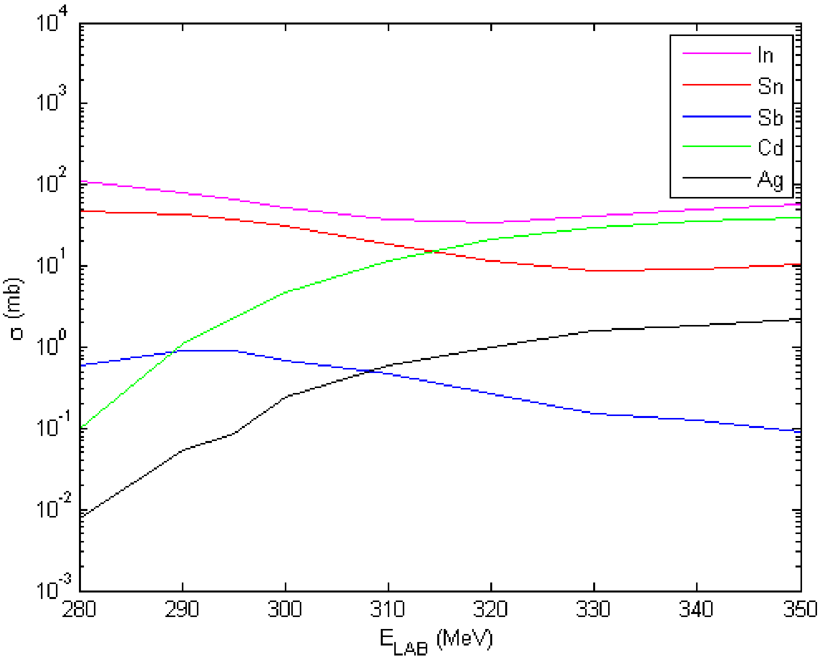

(b) A=105.

Figure 22: PACE4 cross sections for ^{58}Ni beam on a ^{nat}Ni target.

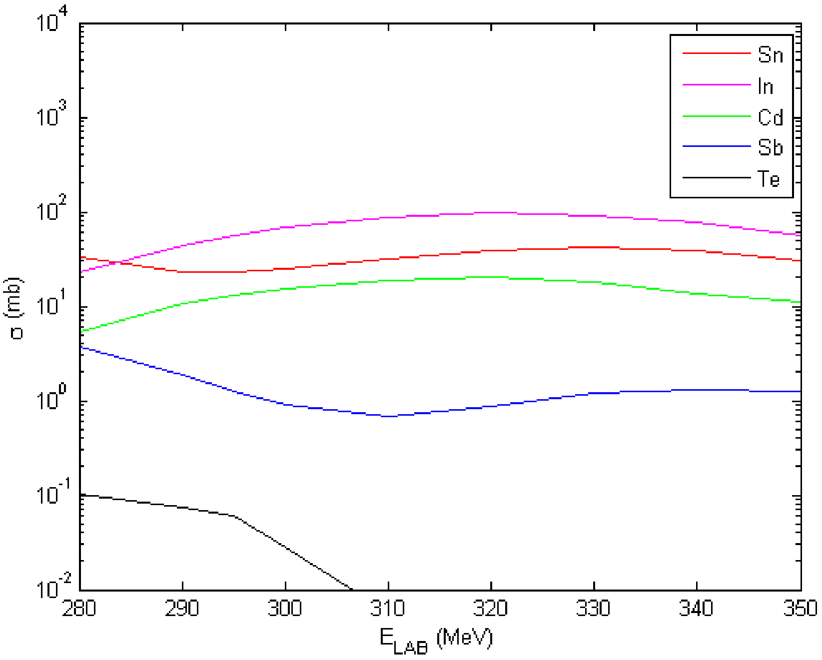

(c) A=106.

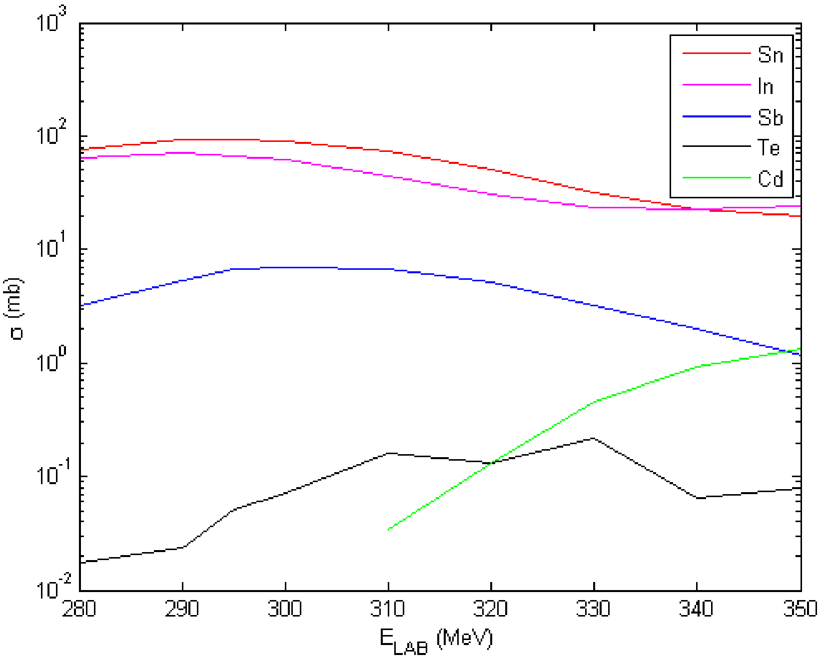

(d) A=107.

Figure 22: PACE4 cross sections for ^{58}Ni beam on a ^{nat}Ni target.

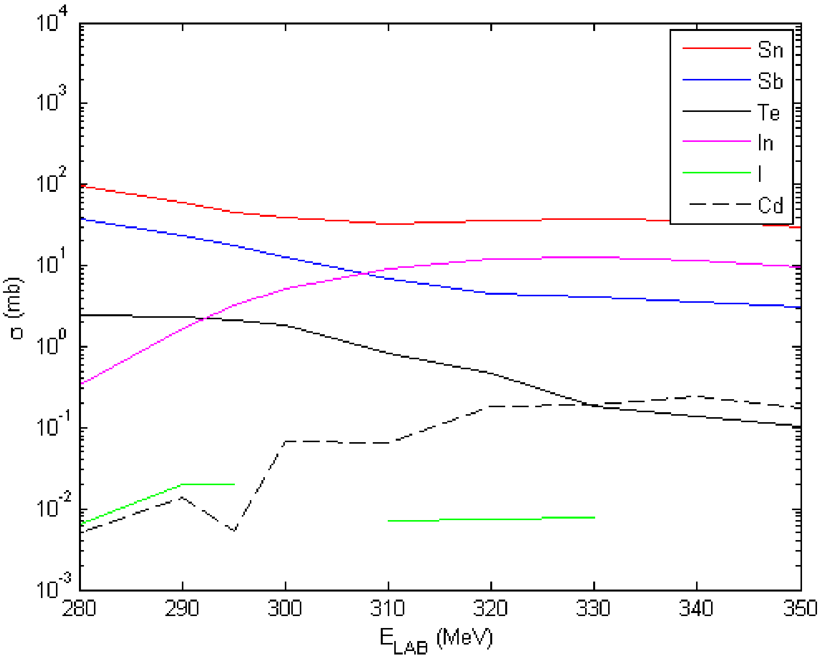

(e) A=108.

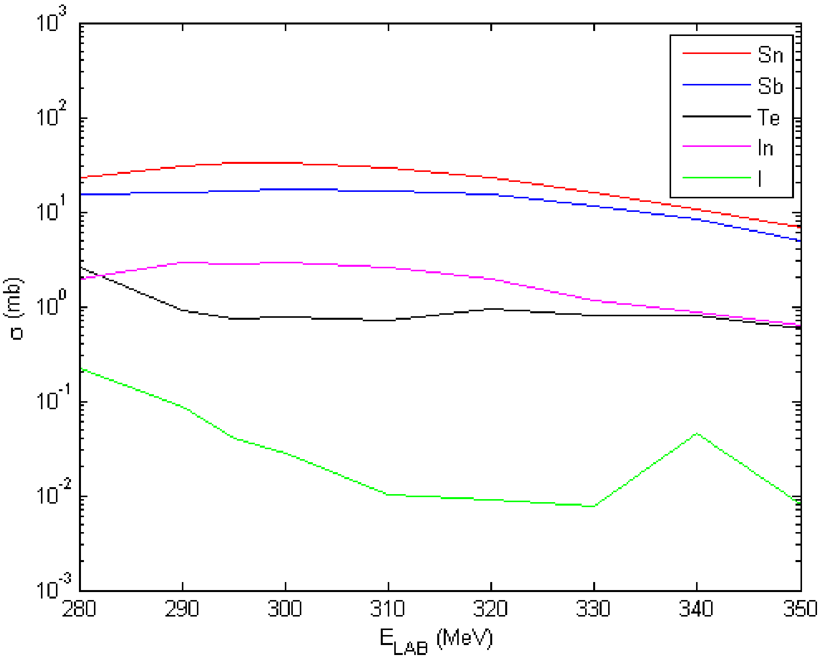

(f) A=109.

Figure 22: PACE4 cross sections for ^{58}Ni beam on a ^{nat}Ni target.

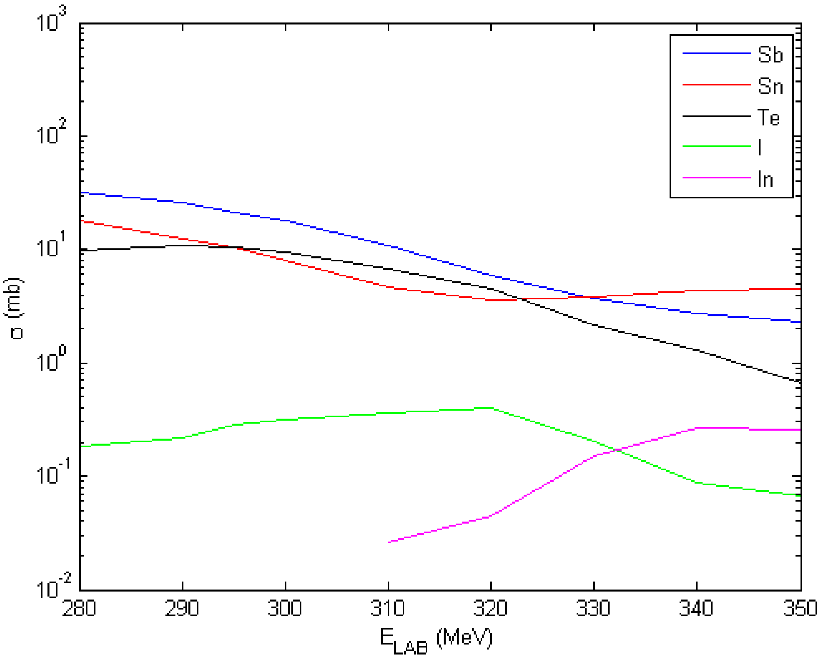

(g) A=110.

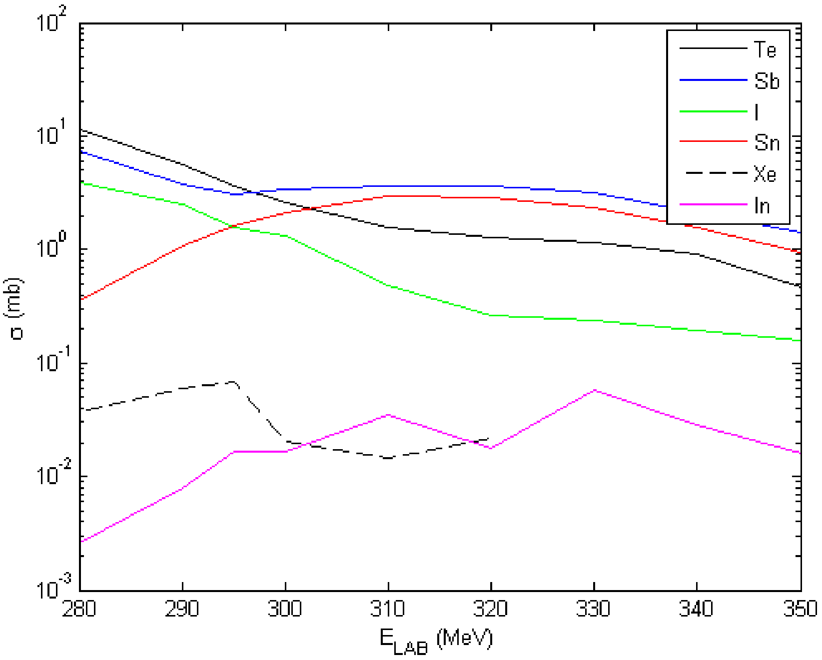

(h) A=111.

Figure 22: PACE4 cross sections for ^{58}Ni beam on a ^{nat}Ni target.

5.5 Measurement E - January 2009

Mass measurement results of the measurement E have not been published yet. A 210-260 MeV ^{40}Ca beam and a ^{nat}Ni target were used. The measurement was focused on technetium isotopes and isomers.

The yields in Table 7 are mainly in agreement with the cross sections of Fig. 19. For the mass number A=91, a slightly lower beam energy than 260 MeV has higher cross sections, and therefore might have produced higher yields. A significantly large yield of ^{91}Zr can be seen although this is not supported by cross-section calculations. ^{91}Zr was not detected in the measurements B and C due to chosen frequency windows. The identification in this measurement was not absolute since no perfect frequency match was found. Stable ^{91}Zr can be produced via β-decays but the yield could also belong to ^{91}Nb. No A=75 nuclei as oxides were found to match with the corresponding cyclotron frequency. Different trap settings were used in the first two measurements which could explain the large differencies in the ion yields.

There is a surprisingly large yield of stable ^{89}Y. Although no cross section exists for ^{89}Y at a beam energy of 210 MeV, it is still detected. The yield of ^{89}Y hails most likely from ion guide tests where yttrium has often been used [66,68]. The measurement with a beam energy of 210 MeV was performed in non-optimal conditions and therefore sticks out with low yields. Again, rubidium salt has been added for reference purposes which explains the enormous yield of ^{85}Rb. Several reference measurements of ^{85}Rb were performed during the measurement E.

Table 7: Ion yields for ^{40}Ca beam on a $^{\mathrm{nat}}$Ni target in the measurement E. Different rows in the ion yield for a given isotope refer to different measurement files. The ions that were detected in the same file are connected with lines.

Beam energy (MeV)	Produced ion	$T_{1/2}$	Ion yield ($1/\mathrm{s}$)	σ_{PACE4} (mb)
260	^{91}Zr	stable	238(3)	–
			216(8)	
			1160(20)	
			1197(13)	
	^{91}Mo	15.49 m	200(9)	62.8(0.7)
			259(9)	
			245(7)	
	^{91}Tc	3.14 m	38.9(1.2)	41.2(0.6)
			109(6)	
			184(7)	
			184(6)	
260	^{89}Y	stable	2850(30)	1.6(0.1) [a]
260			2610(30)	
260			1960(40)	
260			1880(40)	
260			1410(40)	
260			3540(50)	
210			15.7(0.9)	– [a]
260	^{89}Nb	2.03 h	90(10)	49.9(0.6)
260			48(8)	
260	^{89}Mo	2.11 m	91(6)	40.7(0.5)
260			46(4)	
260			249(13)	
260			226(14)	
260			185(14)	
210			3.0(0.5)	82.1(0.8)
210	^{85}Rb	stable	31000(2000)	– [b]

a. The yield is most likely explained by previous ion guide tests.

b. Rubidium salt had been added for reference purposes.

6 Cross-section Calculations for Future Measurements

Cross section calculations were performed with PACE4 in order to find suitable beam, target and energy combinations to fill out the chart of the nuclei measured with JYFLTRAP (Fig. 6) in future measurements. Of special interest is the unmeasured region around In–Cd–Ag. The calculations were made for ^{28}Si+^{58}Ni, ^{50}Cr+^{54}Fe, ^{50}Cr+^{58}Ni and ^{54}Fe+^{58}Ni for possible beam energies from 100 MeV to 300 MeV with 10-MeV steps. ^{28}Si beam is currently available at the Accelerator Laboratory with a maximum beam energy of 375 MeV. The production of ^{50}Cr and ^{54}Fe beams should also be possible if enriched material is available [69]. ^{50}Cr beam has been used in fusion evaporation experiments at SHIPTRAP [27]. The reaction ^{32}S+^{54}Fe results in the same compound nucleus as ^{28}Si+^{58}Ni and was not calculated separately. ^{32}S beam with a maximum beam energy of 330 MeV can be produced at the Accelerator Laboratory. Similarily, ^{54}Fe+^{54}Fe results in the same compound nucleus as ^{50}Cr+^{58}Ni.

The beam and target pairs, which give the highest cross sections, are presented for In, Cd and Ag in Table 8 and for the others in Table 9. Cross sections under 0.1 mb have been neglected. Approximated literature mass excess values are also shown [67]. Cross sections were also plotted against beam energies for different mass numbers. Measurement-wise, instead of the highest cross section for one nucleus, information on a combination that produces sufficient cross sections so that several nuclei can be measured with the same configuration is often useful. The plots are shown in Appendix A. As an example, errorbars are also shown for ^{28}Si+^{58}Ni. As can be seen in Figures 17-19 and 22, cross sections in performed measurements have varied roughly from few to few hundred millibarns. However, the masses of ^{108}Te and ^{111}I have been measured in conditions corresponding to cross sections of only 0.18(0.04) mb and 0.24(0.04) mb. Therefore, the success of a measurement with a calculated cross section under 1 mb is possible but not guaranteed.

In Table 8 there are several nuclei whose mass excess is currently known with a low accuracy. At least $^{96-98}$Ag, ^{98}Cd and ^{100,101}In could be measured in the future. These nuclei are located at the rp-process path (Fig. 1) and therefore the exact masses are of special interest. The mass-excess values of ^{95}Ag, ^{97}Cd and ^{99}In are also highly inaccurate but due to the small cross sections measurements may not succeed. In addition, there is a fine possibility to improve the precision of all the other masses as well except for $^{99,101,103-105}$Ag and ^{99,100}Cd due to current rather high precision of mass-excess values. The precision in the HIGISOL mass measurements has commonly been around 5 keV [24,25,26]. All the nuclei in Table 8 have long enough half-lives (>100 ms) to be measured. If a precision mass measurement has already been performed at another Penning trap facility, measurement at JYFLTRAP can still give valuable information on the accuracy.

All nuclei in Table 9 with mass number 84 or below have large uncertainties in the mass excess values. Out of these at least ^{79}Y, ^{81,82}Zr and ^{83,84}Nb have cross sections large enough to be attempted to be measured. These nuclei are also astrophysically interesting. If these measurements succeed, also ^{80}Zr could be possibly measured. In addition, ^{91}Mo, ^{95}Ru, $^{96-98}$Rh, ^{102,103}Sn, and ^{105}Sb could probably be succesfully measured. Due to small cross sections, the measurement of ^{84}Mo, ^{100}Rh, ^{101}Sn, ^{104}Sb and ^{110}I may not succeed. Still, it is worth trying since large improvements in the current inaccurate mass-excess values could be achieved with JYFLTRAP. The half-lives of ^{78}Y, ^{82}Nb, ^{106,107}Te and ^{109}I are too short (<100 ms) for mass measurements.

Direct mass measurements of ^{94}Ag are needed in order to solve the mysteries of its high-spin isomeric state [15]. The PACE4 calculations give a maximum cross section of 0.117 mb for ^{40}Ca+$^{\mathrm{nat}}$Ni reaction at a beam energy of 180 MeV. A hot cavity laser ion source technique has been under development at the IGISOL facility [70]. With this techinque, a better efficiency and therefore higher yields of ^{94}Ag are expected.

The future measurements will be performed at the new IGISOL facility. Operation of the new IGISOL4 set-up is currently starting in the Accelerator Laboratory extension hall [71]. At the new location, beams from both the K-130 heavy-ion and the MCC 30/15 light-ion cyclotrons are available. Since IGISOL will be the main user of the new light-ion cyclotron, an increase in the available beam time is expected.

The increased floor space enables installation of more complex and permanent equipment. The new location has no direct effects to the IGISOL efficiency since the structure is not significantly changed. However, improvements along the beam line have been made. For example, the beam transportation is expected to be better because of improved positioning of beam diagnostic units. A redesigned switchyard allows taking full advantage of the three beam lines, one of which will be used for on-line beam monitoring. The development process of the IGISOL4 is ongoing. As was seen for example in the measurement C, the set-up has a huge impact on achieved yields.

Table 8: The best beams, targets and beam energies to produce In, Cd and Ag ions according to PACE4 cross-section calculations. The mass excess values are from Atomic Mass Evaluation 2011 (AME11) [67] unless stated otherwise.

Ion of interest	Beam	Target	Beam energy (MeV)	Cross section (mb)	Mass excess (keV)
^{95}Ag	^{50}Cr	^{54}Fe	270	0.36(0.07)	-59597(401)
^{96}Ag	^{50}Cr	^{54}Fe	250	3.2(0.2)	-64623(61)
^{97}Ag	^{50}Cr	^{54}Fe	200	33.8(0.5)	-70826(111)
^{98}Ag	^{50}Cr	^{58}Ni	210	53.4(0.7)	-73051(38)
^{99}Ag	^{50}Cr	^{58}Ni	260	129(2)	-76708(4) [27]
^{101}Ag	^{54}Fe	^{58}Ni	250	96(1)	-81334(4) [27]
^{102}Ag	^{54}Fe	^{58}Ni	300	67.6(0.9)	-82247(9)
^{103}Ag	^{54}Fe	^{58}Ni	280	17.2(0.5)	-84800(4)
^{104}Ag	^{54}Fe	^{58}Ni	300	0.57(0.08)	-85115(6)
^{105}Ag	^{54}Fe	^{58}Ni	300	0.9(0.1)	-87071(5)
^{97}Cd	^{50}Cr	^{54}Fe	300	0.22(0.06)	-60454(298)
^{98}Cd	^{50}Cr	^{54}Fe	260	6.1(0.3)	-67621(55)
^{99}Cd	^{50}Cr	^{54}Fe	220	18.3(0.5)	-69931(2)
^{100}Cd	^{50}Cr	^{58}Ni	230	77.6(0.9)	-74195(2)
^{99}In	^{50}Cr	^{54}Fe	240	1.12(0.11)	-61376(196)
^{100}In	^{50}Cr	^{54}Fe	200	6.5(0.3)	-64344(181)
^{101}In	^{50}Cr	^{58}Ni	210	22.9(0.5)	-68614(298)
^{103}In	^{54}Fe	^{58}Ni	280	59.5(0.8)	-74632(9) [27]
^{105}In	^{54}Fe	^{58}Ni	220	141(1)	-79641(10) [27]
^{106}In	^{54}Fe	^{58}Ni	270	46(1)	-80604(12)
^{107}In	^{54}Fe	^{58}Ni	240	35.3(0.6)	-83564(11)

Table 9: The best beams, targets and beam energies according to PACE4 cross section calculations. The mass excess values are from Ref. [67].

Ion of interest	Beam	Target	Beam energy (MeV)	Cross section (mb)	Mass excess (keV)
^{78}Y	^{28}Si	^{58}Ni	170	2.1(0.2)	-52527(401)
^{79}Y	^{28}Si	^{58}Ni	140	14.3(0.4)	-58357(451)
^{80}Zr	^{28}Si	^{58}Ni	120	1.74(0.13)	-55517(1491)
^{81}Zr	^{28}Si	^{58}Ni	150	10.7(0.4)	-58397(165)
^{82}Zr	^{28}Si	^{58}Ni	130	49.5(0.8)	-63944(200)
^{82}Nb	^{28}Si	^{58}Ni	130	1.6(0.2)	-52201(298)
^{83}Nb	^{28}Si	^{58}Ni	110	11.8(0.4)	-58412(301)
^{84}Nb	^{28}Si	^{58}Ni	100	7.2(0.3)	-61022(300)
^{84}Mo	^{28}Si	^{58}Ni	100	0.67(0.07)	-54502(401)
^{87}Mo	^{50}Cr	^{54}Fe	280	0.26(0.06)	-66883(4)
^{90}Mo	^{50}Cr	^{54}Fe	300	24.8(0.6)	-80174(7)
^{91}Mo	^{50}Cr	^{54}Fe	300	118(2)	-82209(12)
^{93}Mo	^{50}Cr	^{54}Fe	300	3.7(0.3)	-86808(4)
^{95}Ru	^{50}Cr	^{58}Ni	290	94(2)	-83458(10)
^{96}Ru	^{50}Cr	^{58}Ni	260	38.5(0.7)	-86080(2)
^{97}Ru	^{50}Cr	^{58}Ni	300	3.1(0.2)	-86121(4)
^{98}Ru	^{50}Cr	^{58}Ni	300	0.61(0.09)	-88225(7)
^{96}Rh	^{50}Cr	^{54}Fe	220	170(2)	-79688(11)
^{97}Rh	^{50}Cr	^{58}Ni	230	89(1)	-82598(36)
^{98}Rh	^{50}Cr	^{58}Ni	280	23.5(0.6)	-83175(12)
^{99}Rh	^{54}Fe	^{58}Ni	300	5.5(0.3)	-85577(7)
^{100}Rh	^{50}Cr	^{58}Ni	300	0.53(0.09)	-85587(19)
^{101}Sn	^{50}Cr	^{54}Fe	180	0.29(0.04)	-59876(298)
^{102}Sn	^{50}Cr	^{58}Ni	190	2.38(0.11)	-64935(101)
^{103}Sn	^{54}Fe	^{58}Ni	210	3.78(0.14)	-66970(71)
^{104}Sb	^{54}Fe	^{58}Ni	270	0.12(0.04)	-59171(218)
^{105}Sb	^{54}Fe	^{58}Ni	230	1.3(0.1)	-63853(17)
^{106}Te	^{54}Fe	^{58}Ni	220	0.14(0.03)	-58220(101)
^{107}Te	^{54}Fe	^{58}Ni	190	0.23(0.03)	-60536(71)
^{110}Te	^{54}Fe	^{58}Ni	190	1.95(0.07)	-72230(7)
^{109}I	^{54}Fe	^{58}Ni	210	0.32(0.04)	-57675(6)
^{110}I	^{54}Fe	^{58}Ni	190	0.85(0.05)	-60464(51)

7 Summary and Outlook

Ion yields in heavy-ion ion-guide experiments in the mass region A=78-111 were determined and compared to cross sections calculated with PACE4 code. The data were collected for precision mass measurements, and to begin with, a fair share of the data had to be neglected as useless for yield determination purposes. Calculated yields agreed roughly with the cross-section calculations. Yields for nuclides with $\sigma < 1$ mb were not observed except for ^{96}Rh in the measurement B. However, with longer measurement time yield estimates for lower yields could have been obtained. The ratios of the calculated cross sections to the ion yields for isobars in the same file could vary a lot from run to run. High yields of stable isotopes that had been used for calibration or testing were observed. In addition, stable Mo isotopes originate from the Havar window. The reliability of the comparison between the cross sections and the ion yields can suffer from problems in tracking down the used measurement settings from old notes. For some of the isotopes, PACE4 could give incorrect cross-section values due to large deviation between old and new mass values.

In future, measurements particulary focused on the yields of neutron-deficient isotopes could be performed at JYFLTRAP. Formerly yields had to be determined from decay spectroscopy but Penning trap measurements enable a more convenient manner. Yields have already been studied in a more sophisticated way in fission experiments at JYFLTRAP [72]. Time-of-flight gating and time history analysis were applied and the production rates were compared to those of reference isotopes. As the fusion experiment data in question were collected during mass measurements, settings of the set-up varied and therefore the yields are not comparable. Precise information on ion yields could be used to improve the accuracy of cross-section calculations with codes such as PACE4. In this way, valuable measurement time can be saved since the success of a measurement could be more accurately evaluated in advance. Precise yield information would also improve our understanding of the HIGISOL set-up. For example, information on differences between oxide yields and normal ion yields or on the optimal target-window distance could be accumulated. Also, difficulties in the production of Mo isotopes were detected although ion-guide method should be independent of the chemical properties of the isotopes.

Lastly, cross sections were calculated for four different beam and target combinations in order to estimate chances to produce ions that have not yet been measured at JYFLTRAP. At least ^{79}Y, ^{81,82}Zr, ^{83,84}Nb, $^{96-98}$Ag, ^{98}Cd and ^{100,101}In could be measured based on PACE4 values. All of these ions could be produced with ^{28}Si beam on a ^{58}Ni target or with ^{50}Cr beam on a ^{54}Fe target although for some of the ions ^{58}Ni target could produce slightly larger cross sections. ^{50}Cr beam is not available at the Accelerator Laboratory but the production should be possible if enriched material can be supplied. The mass-excess values of ^{80}Zr, ^{84}Mo, ^{95}Ag, ^{97}Cd, ^{99}In, ^{101}Sn, ^{104}Sb and ^{110}I are also of interest but the measurement may not succeed based on small PACE4 cross sections. Still, the new IGISOL facility provides an excellent setting for further yield measurements.

References

1. R.K. Wallace and S.E. Woosley, Astrophys. J. Suppl. Ser. **45**, 389 (1981).
2. H. Schatz *et al.*, Phys. Rep. **294**, 167 (1998).
3. H. Schatz *et al.*, Phys. Rev. Lett. **86**, 3471 (2001).
4. H. Schatz *et al.*, Nucl. Phys. A **621**, 417c (1997).
5. H. Schatz, Int. J. Mass Spectrom. **251**, 293 (2006).
6. C. Fröhlich *et al.*, Phys. Rev. Lett. **96**, 142502 (2006).
7. S. Wanajo, Astrophys. J. **647**, 1323 (2006).
8. J. Pruet *et al.*, Astrophys. J. **644**, 1028 (2006).
9. K. Ogawa, Phys. Rev. C **28**, 958 (1983).
10. H. Grawe and M. Lewitowicz, Nucl. Phys. A **693**, 116 (2001).
11. H. Grawe, in Euroschool Lectures on Physics with Exotic Beams Vol. 1, edited by J. Al-Khalili and E. Roeckl, Springer Lecture Notes in Physics (Springer, Berlin, 2004).
12. N. Marginean *et al.*, Phys. Rev. C **67**, 061301(R) (2003).
13. T.S. Brock *et al.*, Phys. Rev. C **82**, 061309(R) (2010).
14. K. Kaneko, Y. Sun, M. Hasegawa and T. Mizusaki, Phys. Rev. C **77**, 064304 (2008).
15. A. Kankainen *et al.*, Phys. Rev. Lett. **101**, 142503 (2008).
16. Yu.N. Novikov *et al.*, Eur. Phys. J. A **11**, 257 (2001).
17. A. Kankainen *et al.*, Eur. Phys. J. A **25**, 355 (2005).
18. J.S. Lilley, Nuclear Physics Principles and Applications (Wiley, Chichester, 2001).
19. W.S.C. Williams, Nuclear and Particle Physics (Clarendon, Oxford, 1991).
20. V.-V. Elomaa *et al.*, Eur. Phys. J. A **40**, 1 (2009).
21. J. Suhonen, From Nucleons to Nucleus Concepts of Microscopic Nuclear Theory (Springer, Berlin, 2007).
22. K. Blaum, Phys. Rep. **425**, 1 (2006).
23. G. Audi, A.H. Wapstra and C. Thibault, Nucl. Phys. A **729**, 337 (2003).
24. A. Kankainen *et al.*, Eur. Phys. J. A **29**, 271 (2006).
25. C. Weber *et al.*, Phys. Rev. C **78**, 054310 (2008).
26. V.-V. Elomaa *et al.*, Phys. Rev. Lett. **102**, 252501 (2009).
27. A. Martín *et al.*, Eur. Phys. J. A **34**, 341 (2007).
28. E. Haettner *et al.*, Phys. Rev. Lett. **106**, 122501 (2011).
29. M. Breitenfeldt *et al.*, Phys. Rev. C **80**, 035805 (2009).
30. J. Fallis *et al.*, Phys. Rev. C **84**, 045807 (2011).
31. http://research.jyu.fi/igisol/JYFLTRAP_masses/area_2_2.php.
32. O. Tarvainen, Studies of Electron Cyclotron Resonance Ion Source Plasma Physics, Ph.D. Thesis, JYFL Research Report No. 8/2005.
33. R. Harkewicz, Rev. Sci. Instrum. **67**, 2176 (1996).

34. H. Koivisto, J. Ärje and M. Nurmia, Nucl. Instrum. Methods Phys. Res. B **94**, 291 (1994).
35. R. Harkewicz *et al.*, Rev. Sci. Instrum. **66**, 2883 (1995).
36. R. Harkewicz, J. Stacy, J. Greene and R.C. Pardo, Rev. Sci. Instrum. **65**, 1104 (1994).
37. J. Ärje *et al.*, Phys. Rev. Lett. **54**, 99 (1985).
38. J. Ärje *et al.*, Nucl. Instrum. Methods Phys. Res. B **26**, 384 (1987).
39. J. Äystö, Nucl. Phys. A **693**, 477 (2001).
40. M. Oinonen *et al.*, Nucl. Instrum. Methods Phys. Res. A **416**, 485 (1998).
41. J. Huikari *et al.*, Nucl. Instrum. Methods Phys. Res. B **222**, 632 (2004).
42. P. Karvonen *et al.*, Nucl. Instrum. Methods Phys. Res. B **266**, 4794 (2008).
43. V.S. Kolhinen *et al.*, Nucl. Instrum. Methods Phys. Res. A **528**, 776 (2004).
44. R. Béraud *et al.*, Nucl. Instrum. Methods Phys. Res. A **346**, 196 (1994).
45. A. Nieminen *et al.*, Nucl. Instrum. Methods Phys. Res. A **469**, 244 (2001).
46. G. Savard *et al.*, Phys. Lett. A **158**, 247 (1991).
47. M. König *et al.*, Int. J. Mass Spectrom. Ion Proc. **142**, 95 (1995).
48. A. Nieminen *et al.*, Phys. Rev. Lett. **88**, 094801-1 (2002).
49. T. Eronen, High Precision Q_{EC} Value Measurements of Superallowed $0^+ \to 0^+$ Beta Decays with JYFLTRAP, Ph.D. Thesis, JYFL Research Report No. 12/2008.
50. V.S. Kolhinen, Penning Trap for Isobaric Purification of Radioactive Beams at IGISOL, Ph.D. Thesis, JYFL Research Report No. 3/2003.
51. S. Naimi *et al.*, Hyperf. Int. **199**, 231 (2011).
52. J.R. Taylor, An Introduction to Error Analysis: the Study of Uncertainties in Physical Measurements, 2nd edition (University Science Books, Sausalito, 1997).
53. www.nscl.msu.edu/lise.
54. O.B. Tarasov and D. Bazin, Nucl. Instrum. Methods Phys. Res. B **204**, 174 (2003).
55. A. Gavron, Phys. Rev. C **21**, 230 (1980).
56. M. Blann, "Recent Progress and Current Status of Preequilibrium Reaction Theories and Computer Code ALICE", UCRL-97948, ITCP Workshop on Applied Nuclear Theory and Nuclear Model Calculations for Nuclear Technology Applications held in Trieste, Italy (1988).
57. M. Blann, "Calculation of Excitation Functions with Code ALICE", UCRL-95918, Coordinated Research Project on Isotope Production for Medical Applications Sponsored by I.A.E.A. Tokyo, Japan (1987).
58. www.oecd-nea.org/tools/abstract/detail/psr-0146.
59. www.oecd-nea.org/tools/abstract/detail/uscd1238.
60. F. Pulnhofer, Nucl. Phys. A **280**, 267 (1977).
61. J.P. Lestone *et al.*, Nucl. Phys. A **559**, 277 (1993).

62. W. Reisdorf, Z. Phys. A **300**, 227 (1981).
63. H. Rossner *et al.*, Phys. Rev. C **40**, 2629 (1989).
64. www.nndc.bnl.gov/chart.
65. www.webelements.com/periodicity/enthalpy_diatomics_MO.
66. I.D. Moore, Nucl. Instrum. Methods Phys. Res. B **266**, 4434 (2008).
67. Private Communication April 2011 by Georges Audi and Wang Meng.
68. I.D. Moore *et al.*, Nucl. Instrum. Methods Phys. Res. B **268**, 657 (2010).
69. https://www.jyu.fi/fysiikka/en/research/accelerator/ionsources/beamdatabase.
70. M. Reponen *et al.*, Eur. Phys. J. A **42**, 509 (2009).
71. H. Penttilä *et al.*, J. Korean Phys. Soc. **59**, 1589 (2011).
72. H. Penttilä *et al.*, Eur. Phys. J. A **44**, 147 (2010).

Appendices

A Cross Sections against Beam Energies for Future Measurements

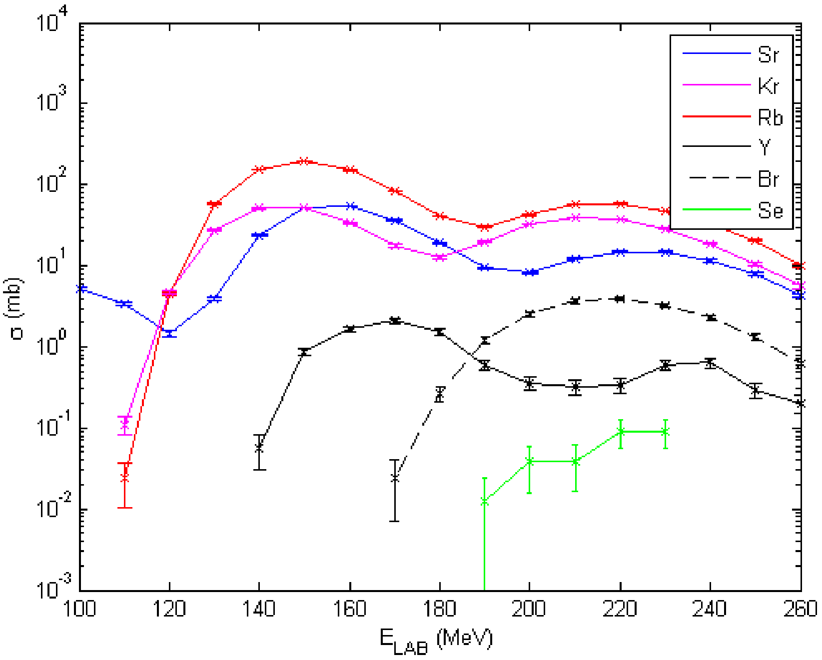

(a) A=78.

Figure 23: PACE4 cross sections for ^{28}Si beam on a ^{58}Ni target.

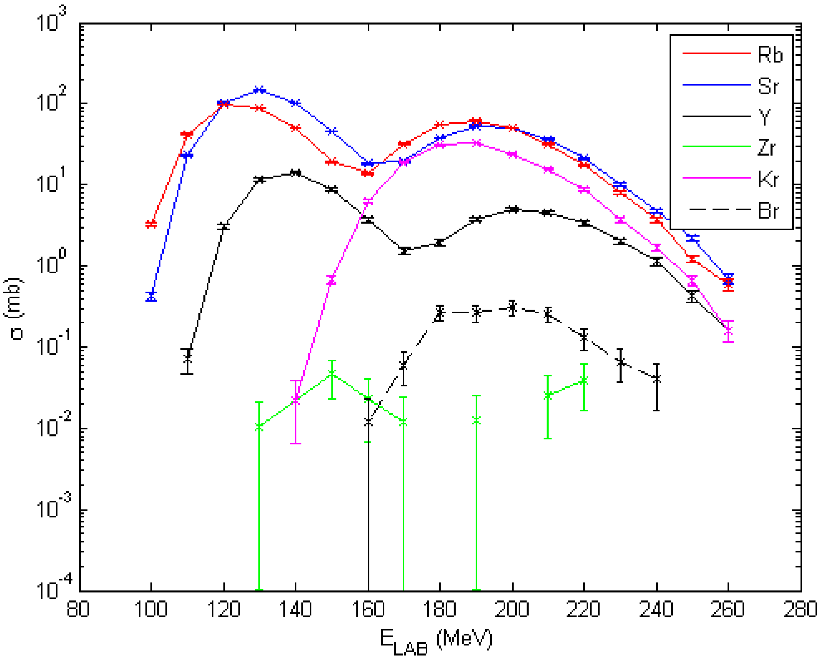

(b) A=79.

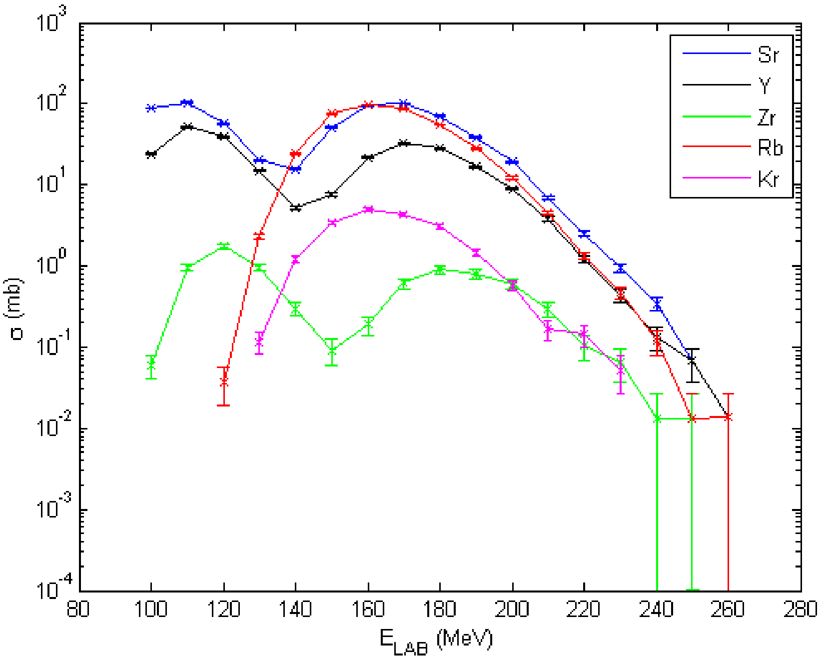

(c) A=80.

Figure 23: PACE4 cross sections for ^{28}Si beam on a ^{58}Ni target.

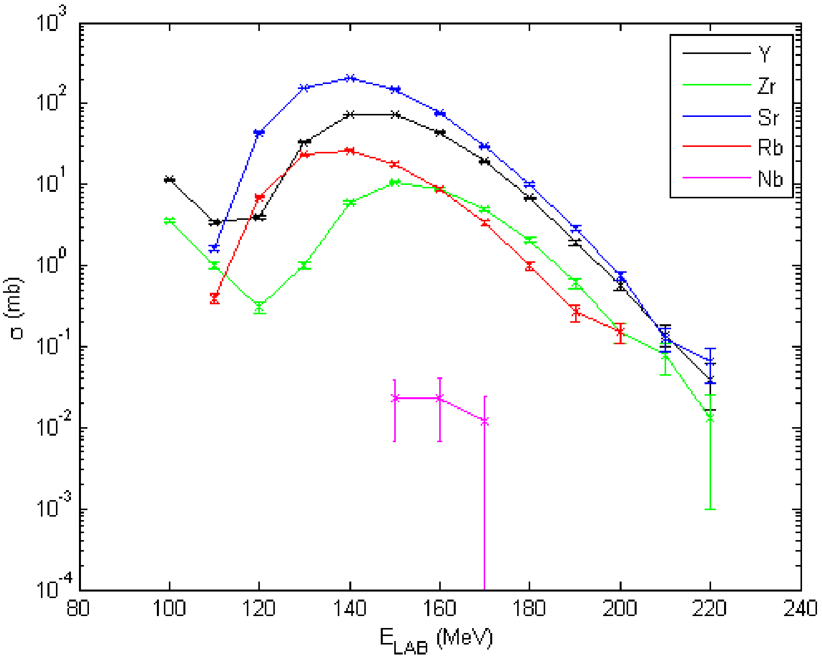

(d) A=81.

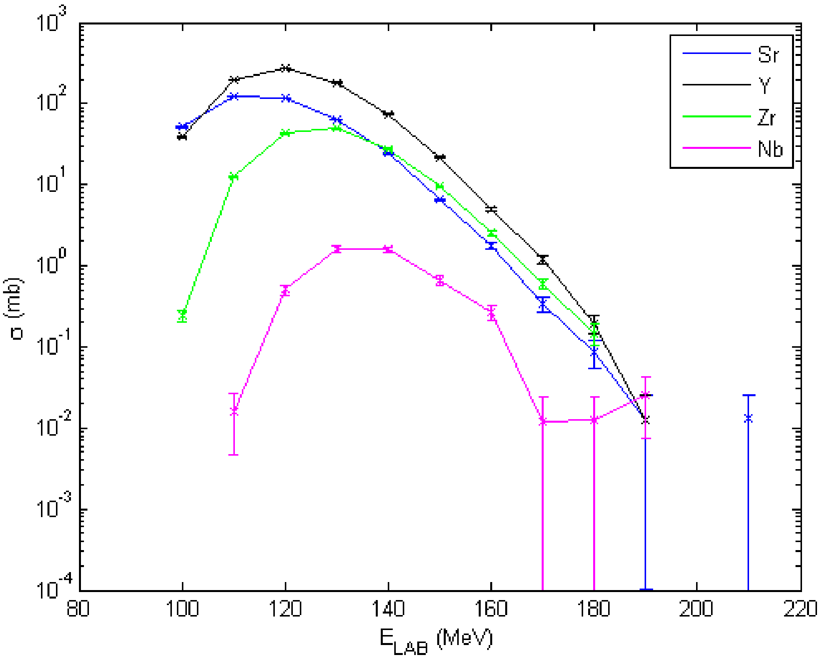

(e) A=82.

Figure 23: PACE4 cross sections for ^{28}Si beam on a ^{58}Ni target.

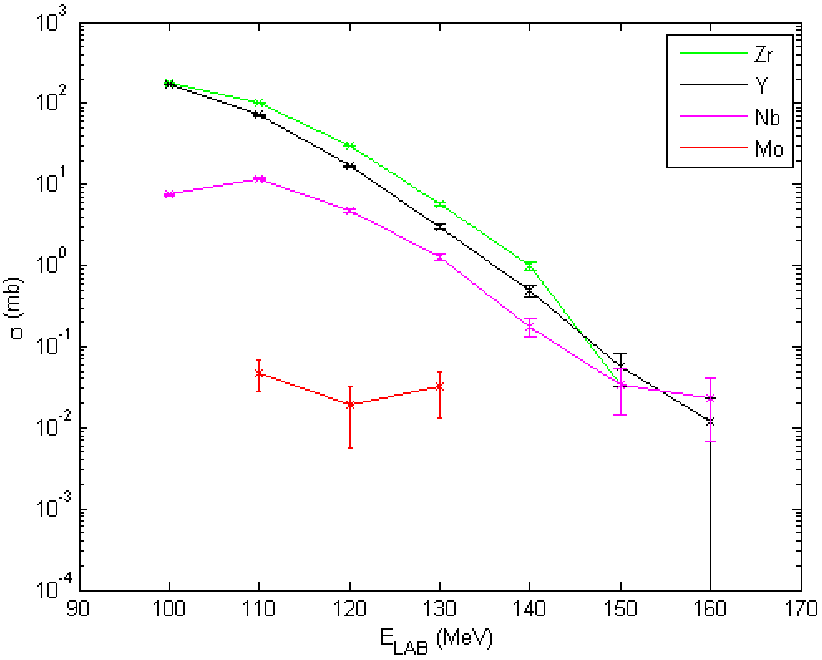

(a) A=83.

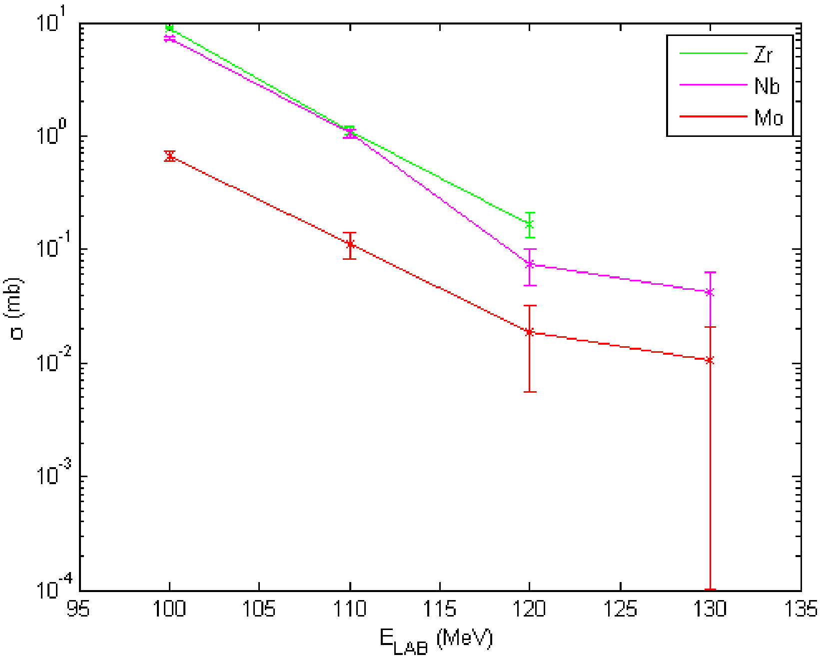

(b) A=84.

Figure 24: PACE4 cross sections for ^{28}Si beam on a ^{58}Ni target.

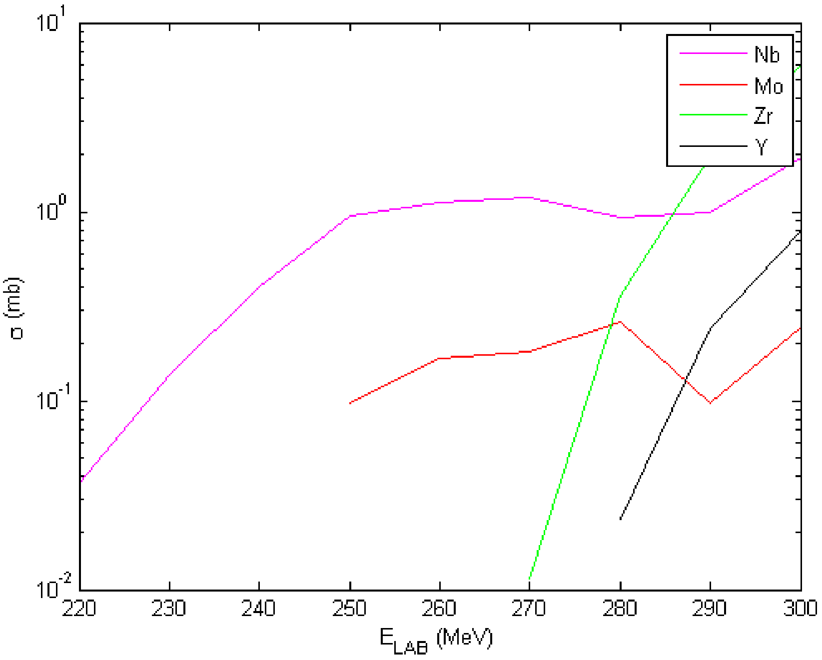

(a) A=87.

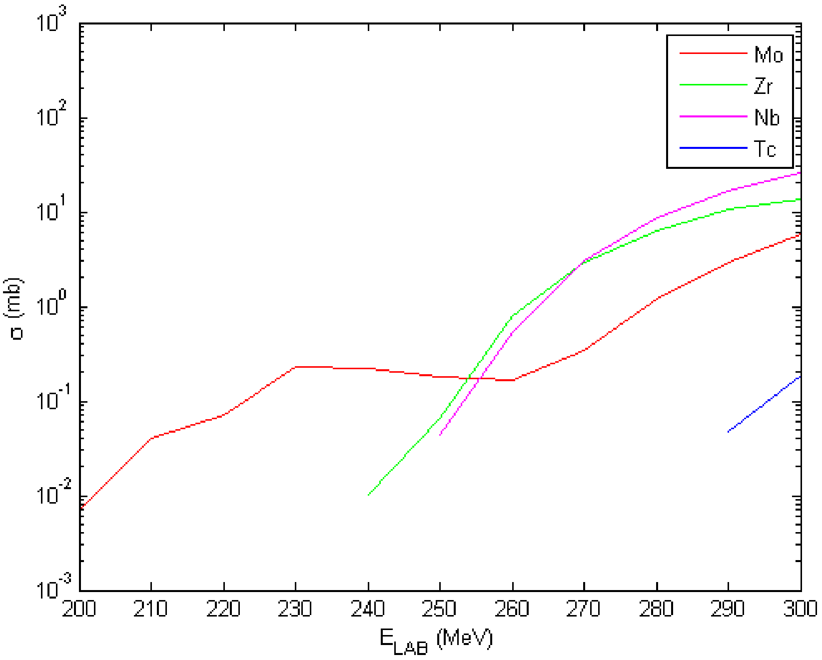

(b) A=88.

Figure 25: PACE4 cross sections for ^{50}Cr beam on a ^{54}Fe target.

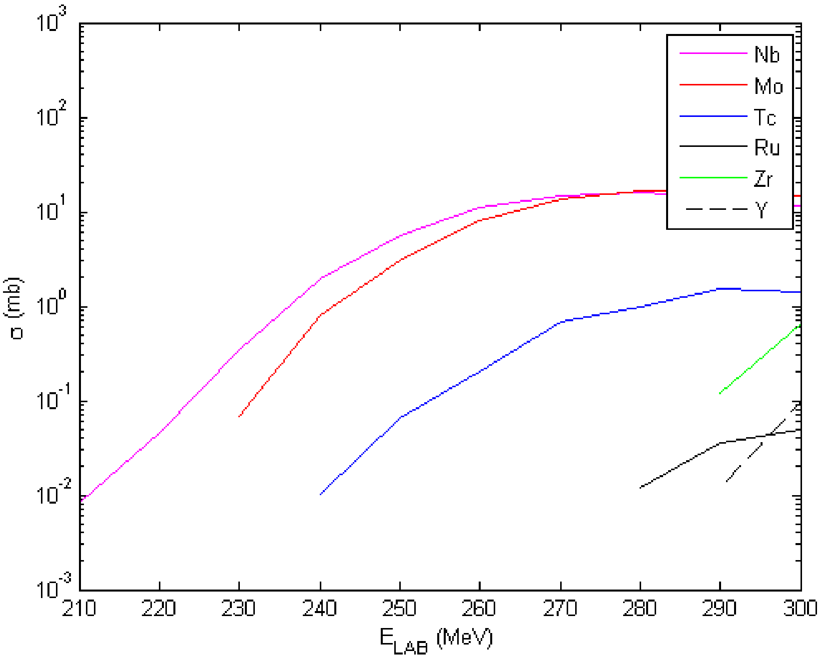

(c) A=89.

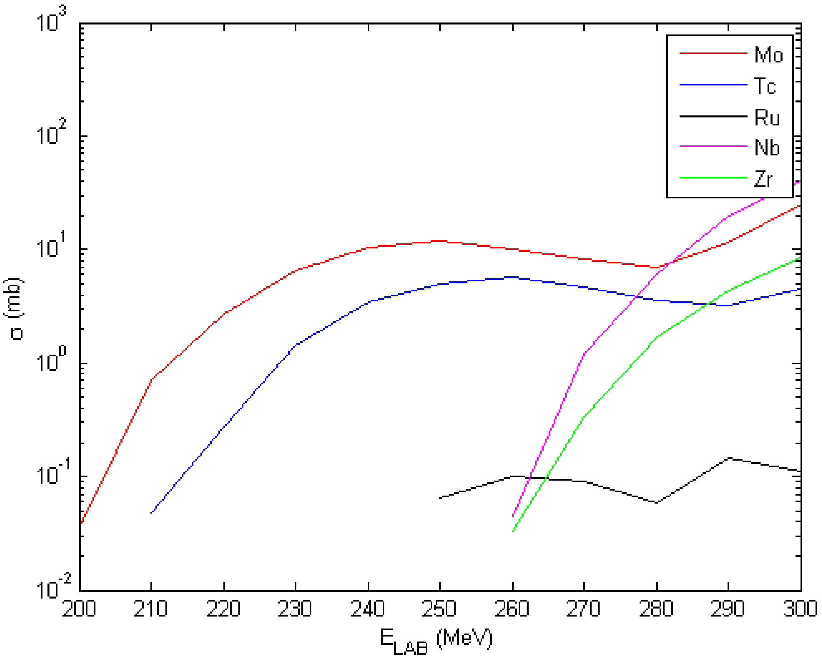

(d) A=90.

Figure 25: PACE4 cross sections for ^{50}Cr beam on a ^{54}Fe target.

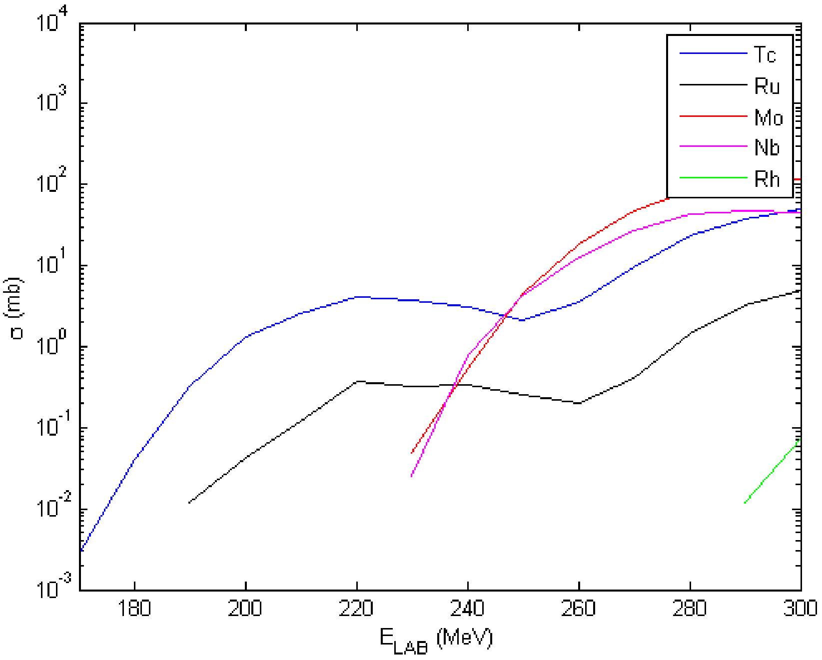

(e) A=91.

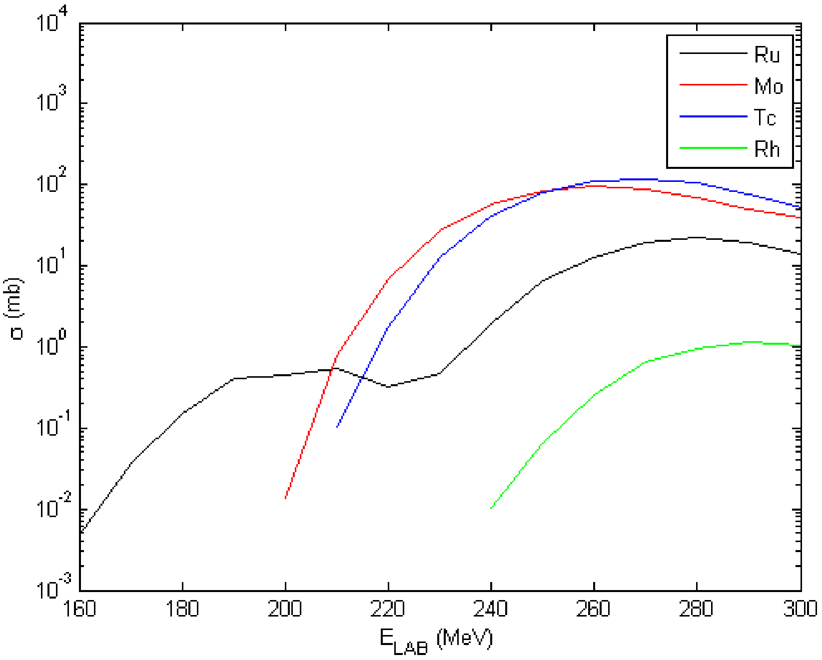

(f) A=92.

Figure 25: PACE4 cross sections for ^{50}Cr beam on a ^{54}Fe target.

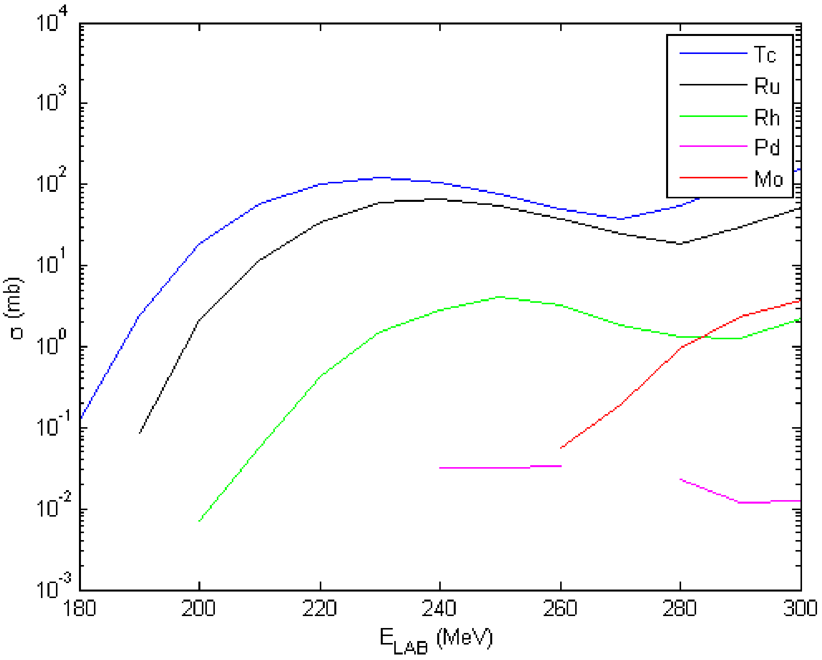

(g) A=93.

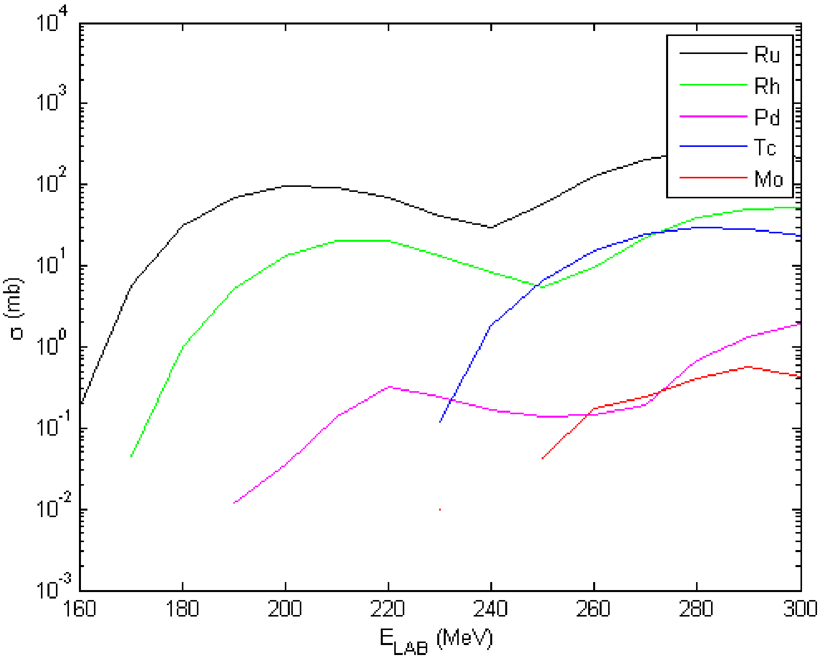

(h) A=94.

Figure 25: PACE4 cross sections for ^{50}Cr beam on a ^{54}Fe target.

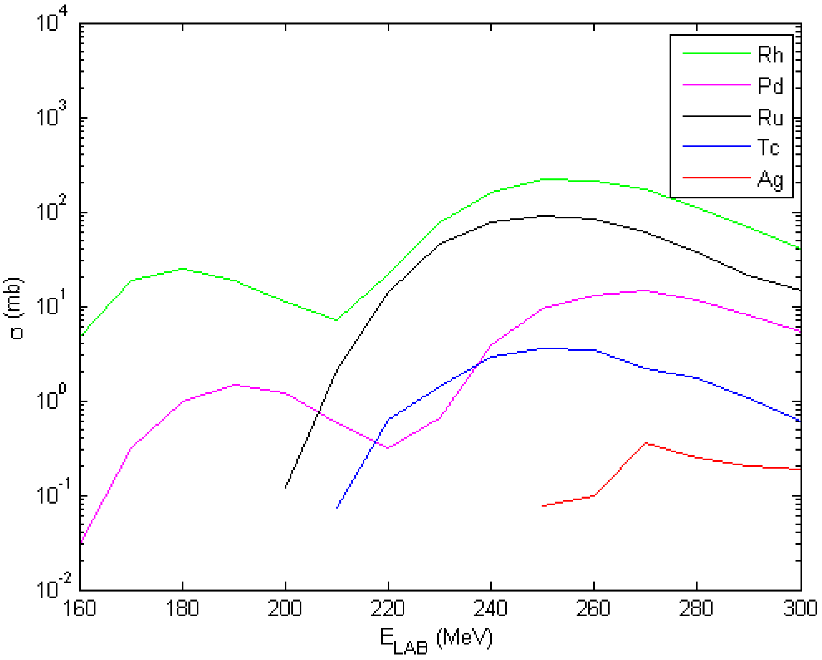

(i) A=95.

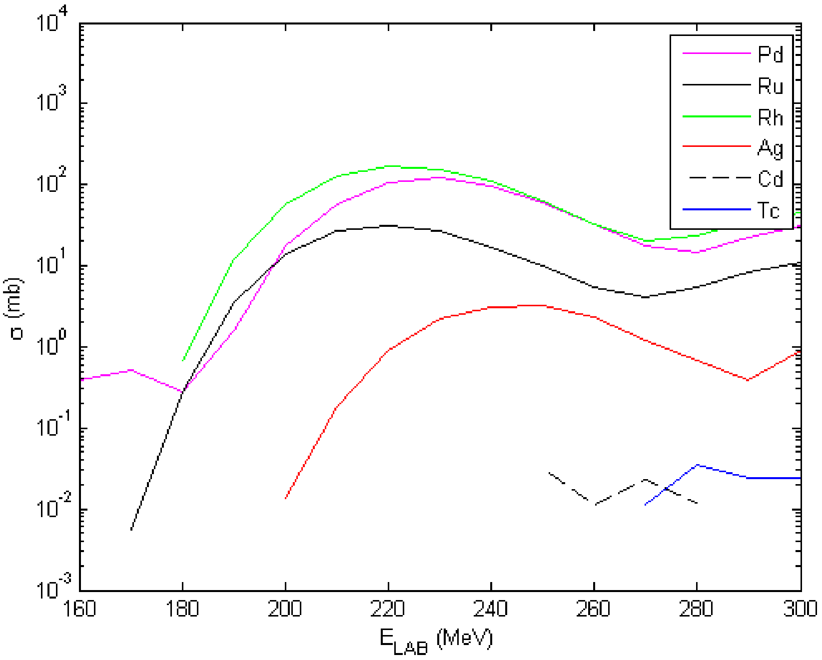

(j) A=96.

Figure 25: PACE4 cross sections for ^{50}Cr beam on a ^{54}Fe target.

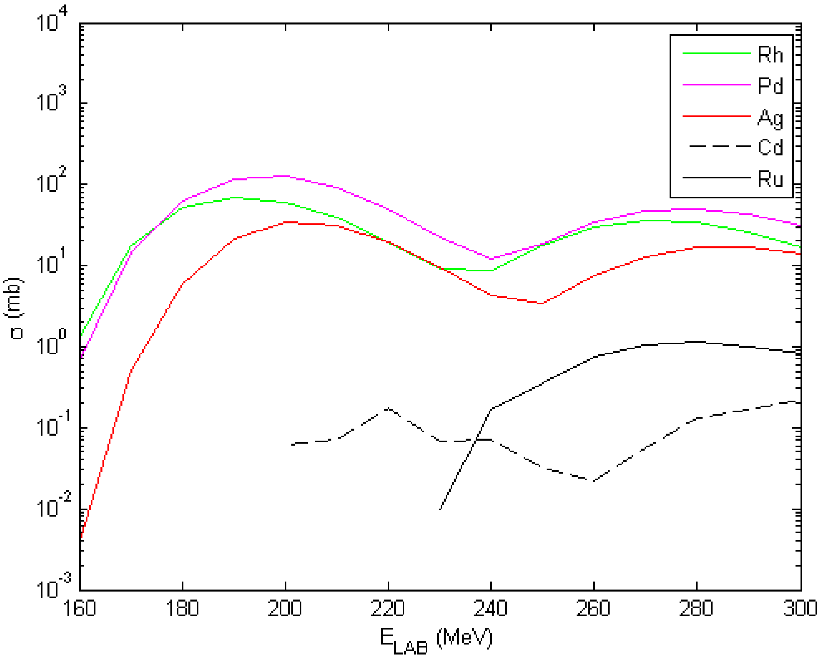

(k) A=97.

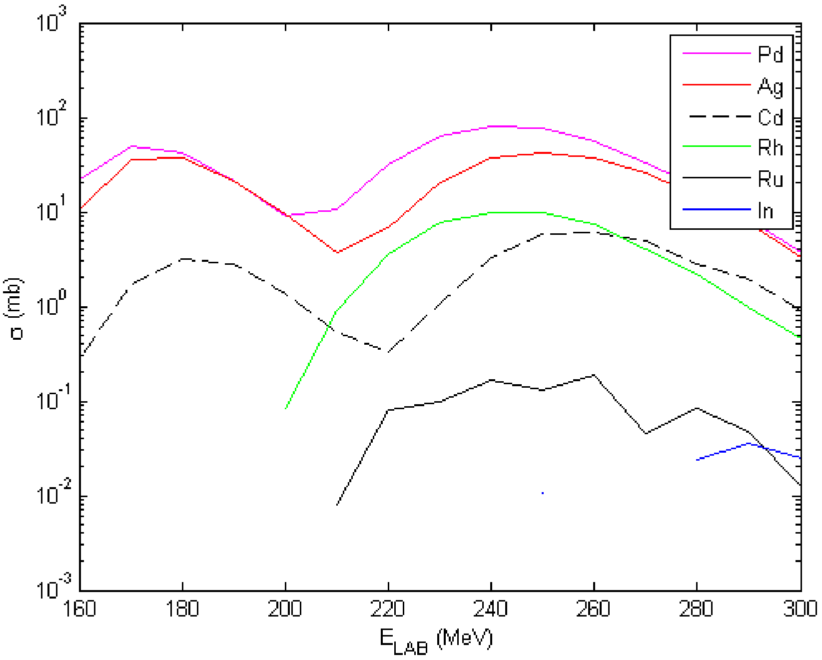

(l) A=98.

Figure 25: PACE4 cross sections for ^{50}Cr beam on a ^{54}Fe target.

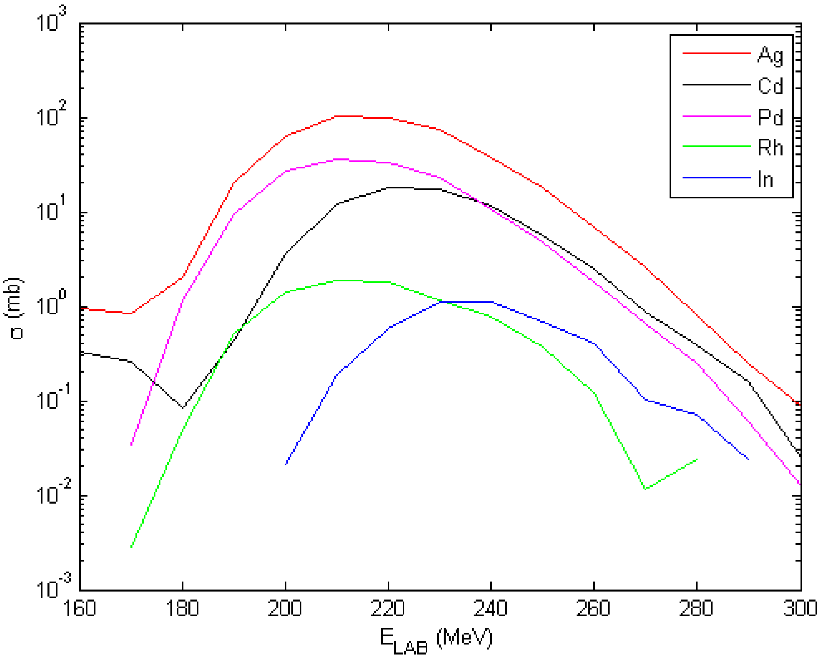

(m) A=99.

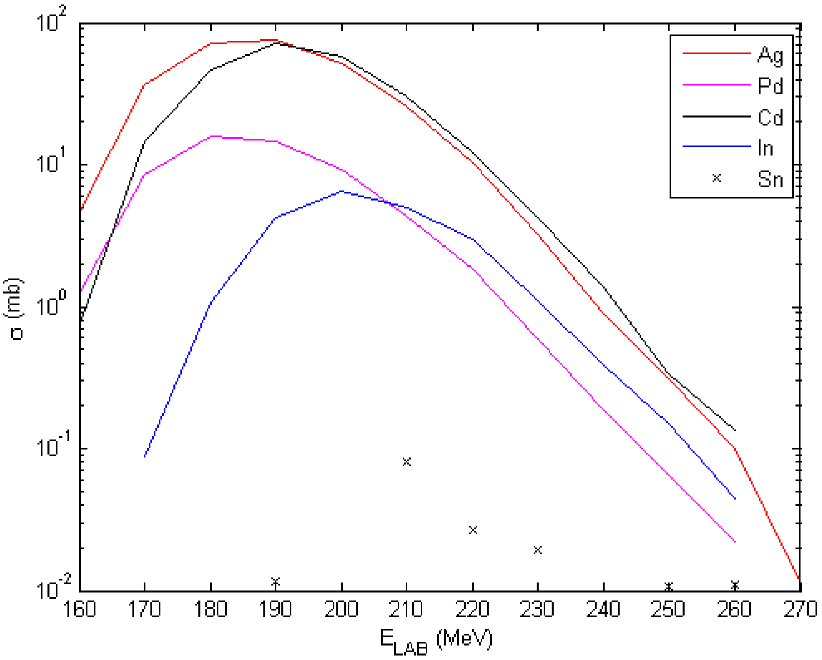

(n) A=100.

Figure 25: PACE4 cross sections for ^{50}Cr beam on a ^{54}Fe target.

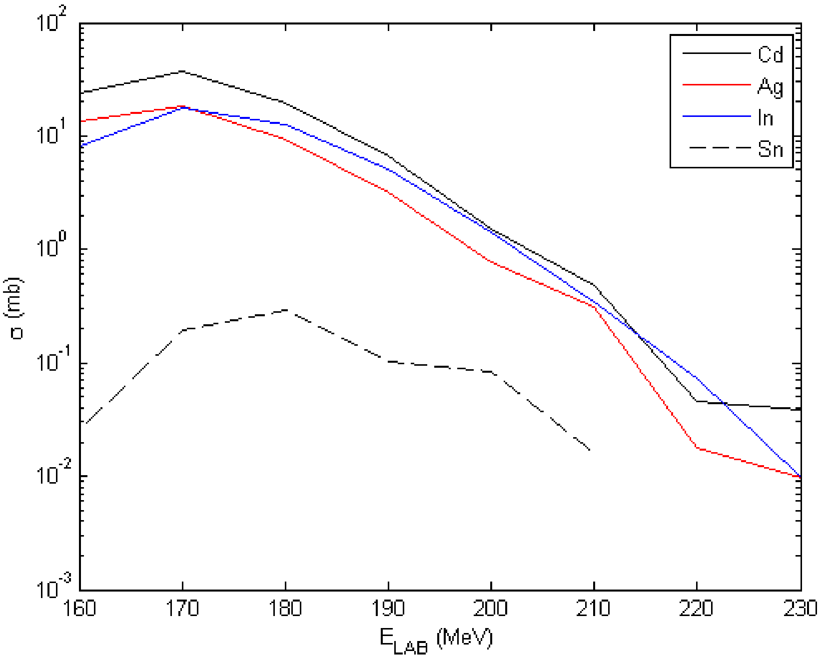

(o) A=101.

Figure 25: PACE4 cross sections for ^{50}Cr beam on a ^{54}Fe target.

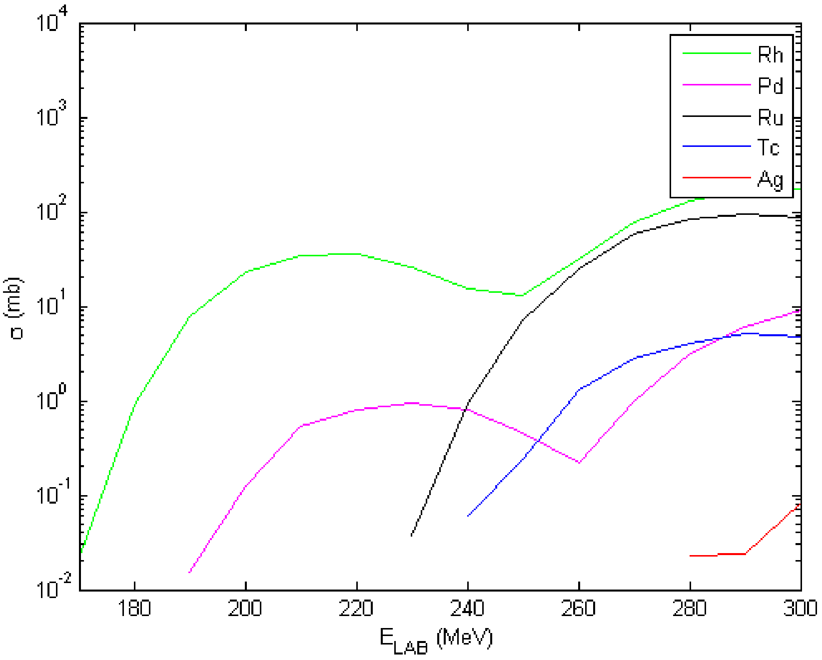

(a) A=95.

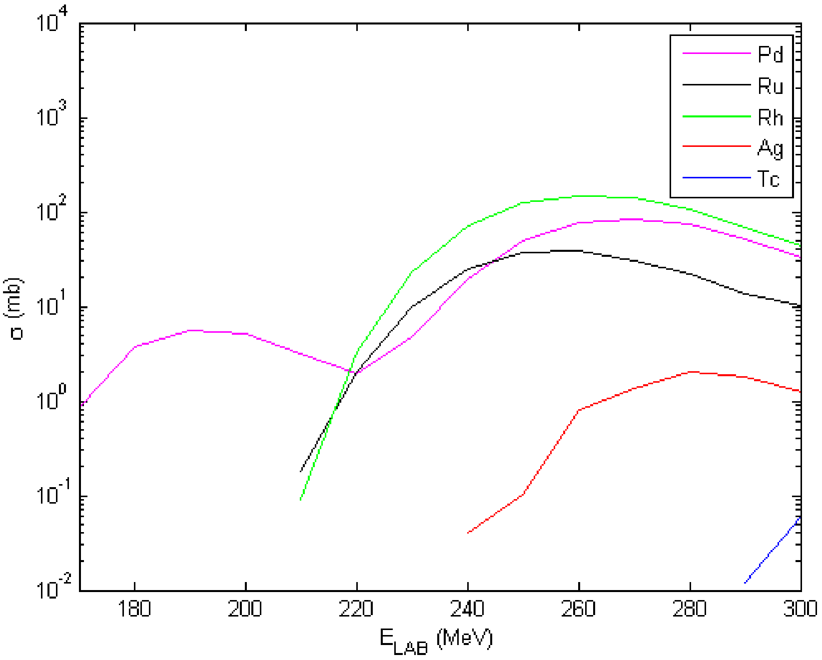

(b) A=96.

Figure 26: PACE4 cross sections for ^{50}Cr beam on a ^{58}Ni target.

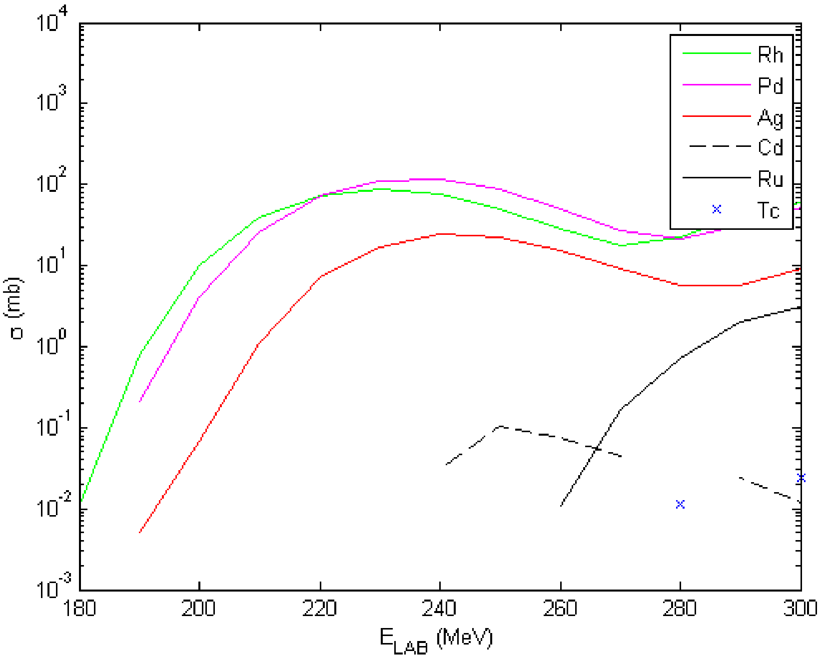

(c) A=97.

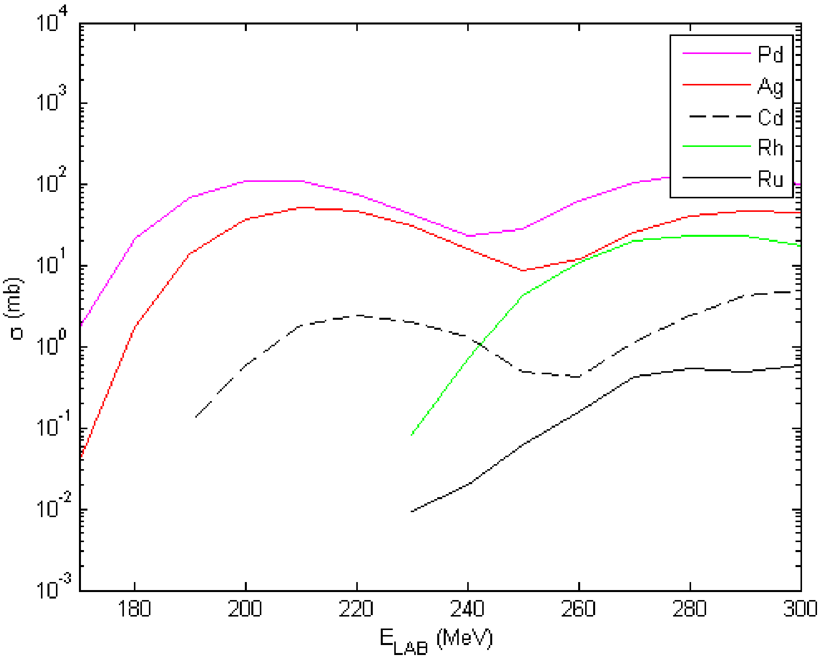

(d) A=98.

Figure 26: PACE4 cross sections for ^{50}Cr beam on a ^{58}Ni target.

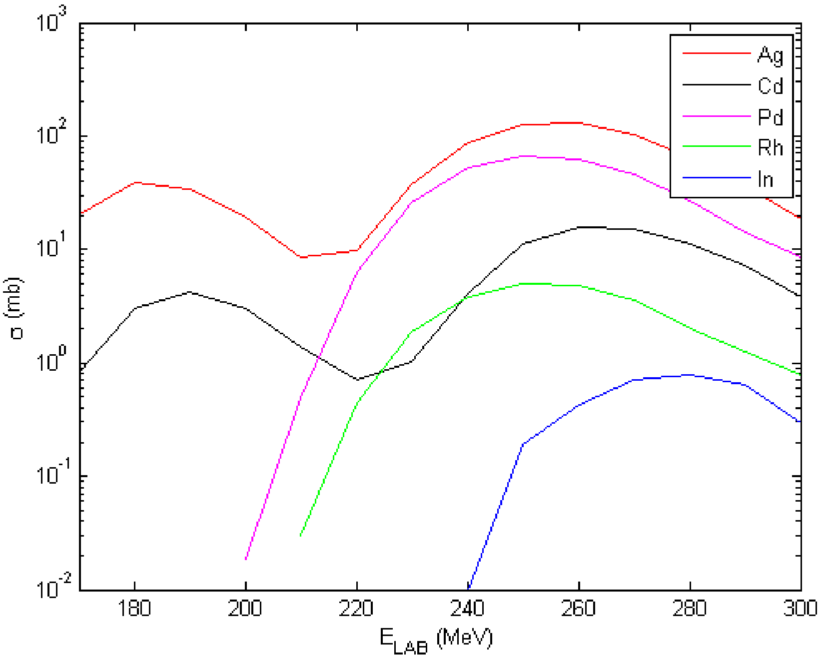

(e) A=99.

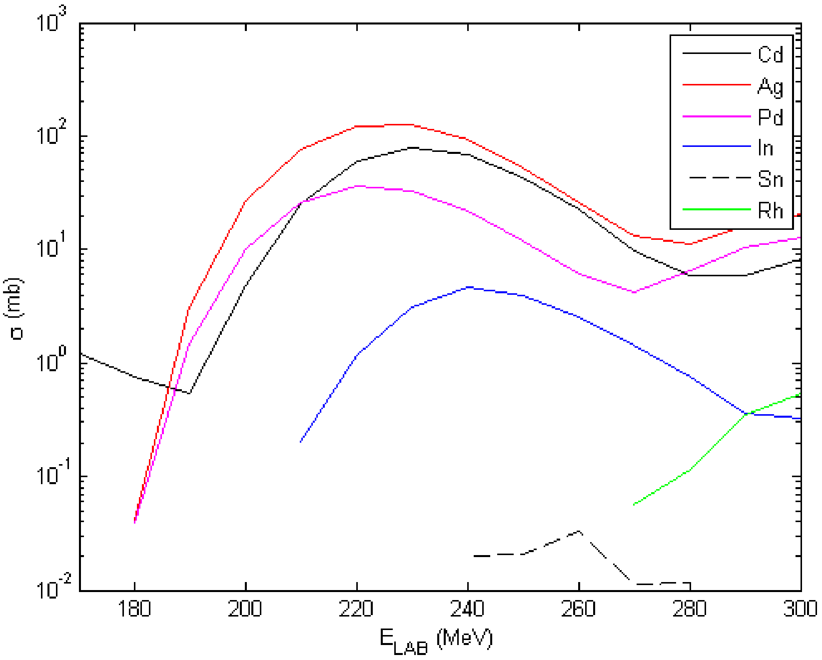

(f) A=100.

Figure 26: PACE4 cross sections for ^{50}Cr beam on a ^{58}Ni target.

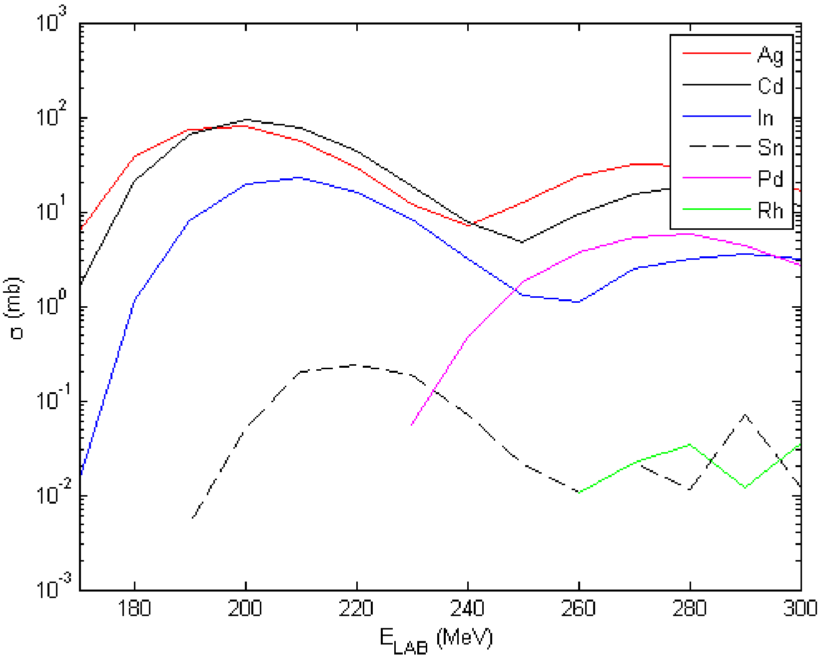

(g) A=101.

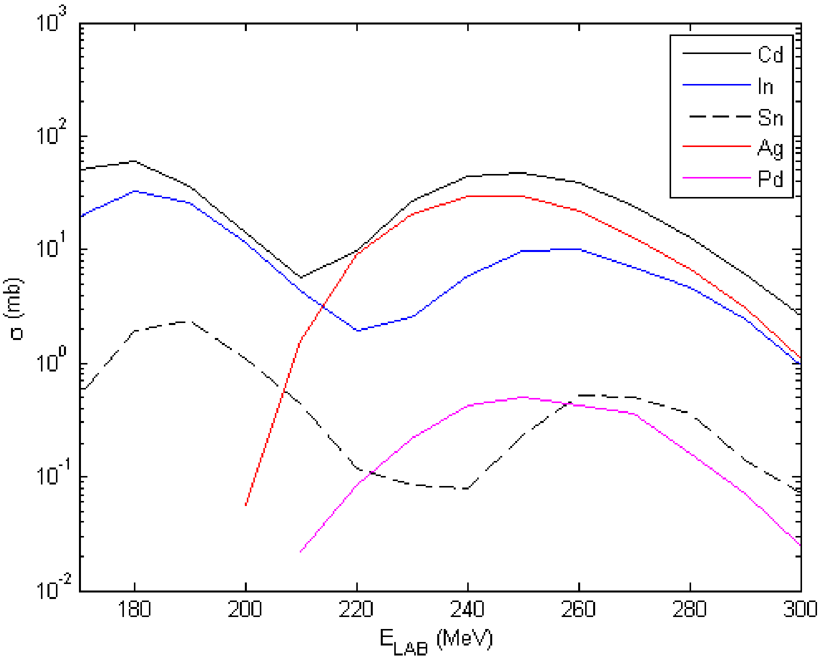

(h) A=102.

Figure 26: PACE4 cross sections for ^{50}Cr beam on a ^{58}Ni target.

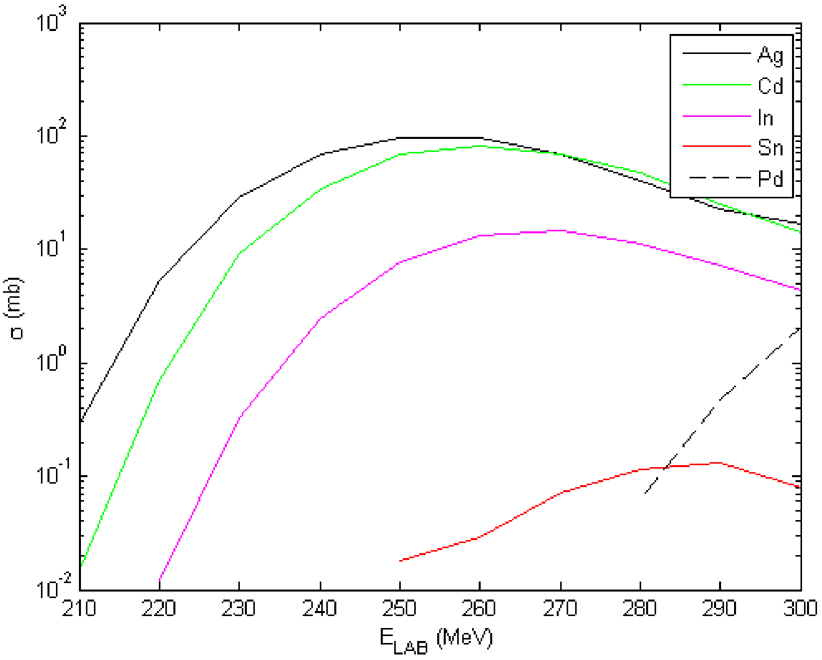

(a) A=101.

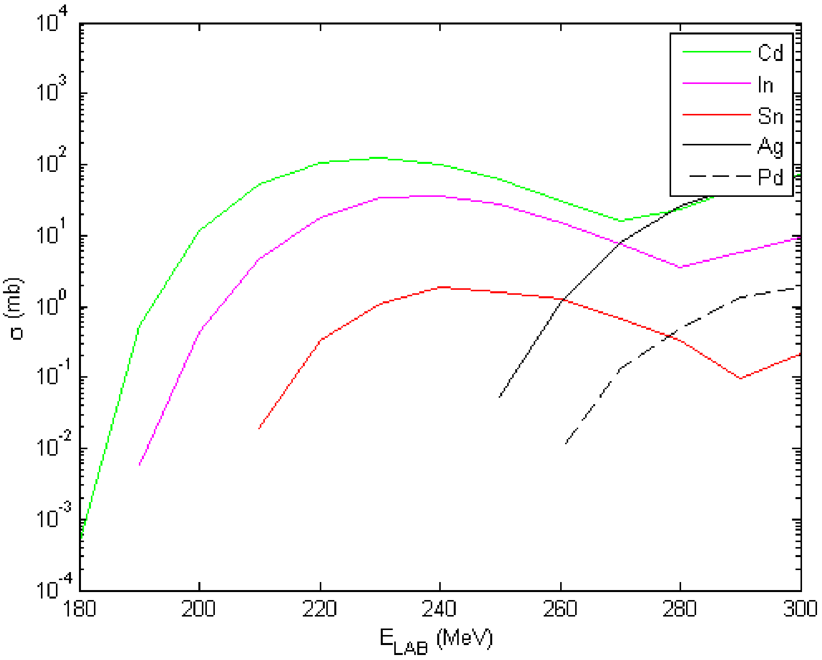

(b) A=102.

Figure 27: PACE4 cross sections for ^{54}Fe beam on a ^{58}Ni target.

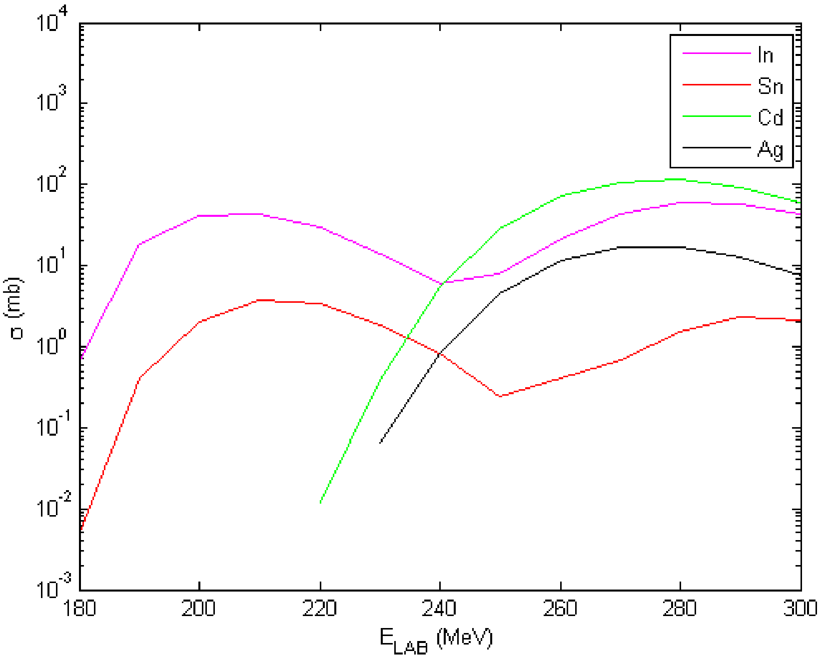

(c) A=103.

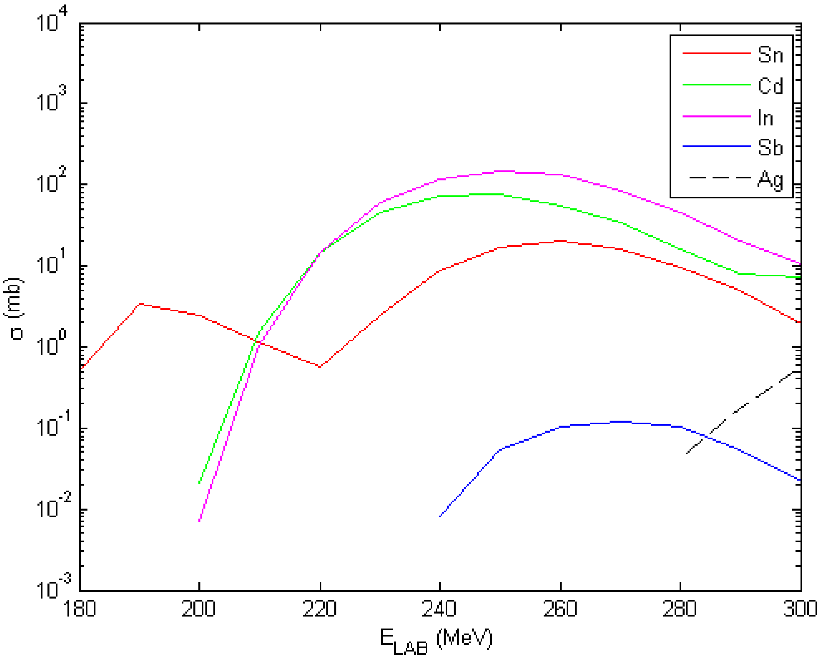

(d) A=104.

Figure 27: PACE4 cross sections for ^{54}Fe beam on a ^{58}Ni target.

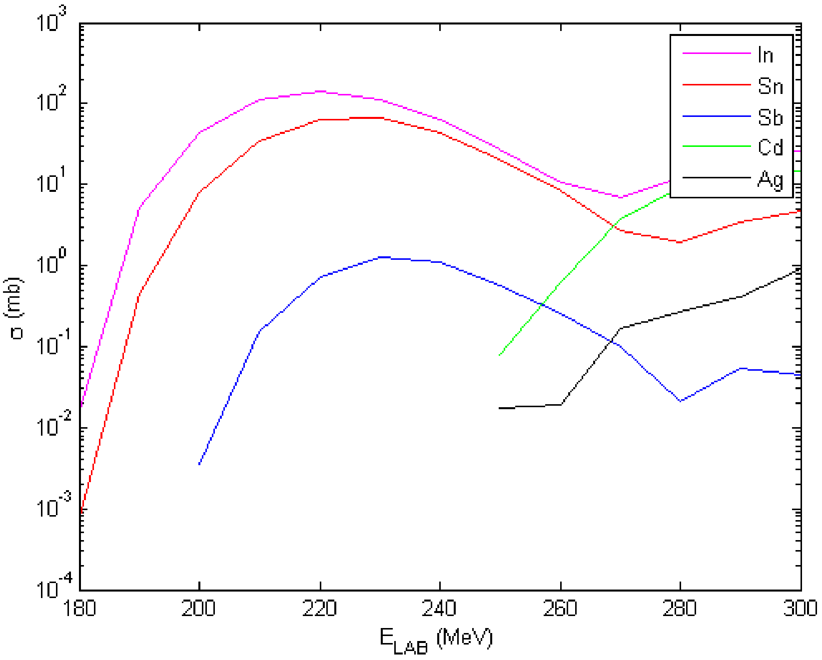

(e) A=105.

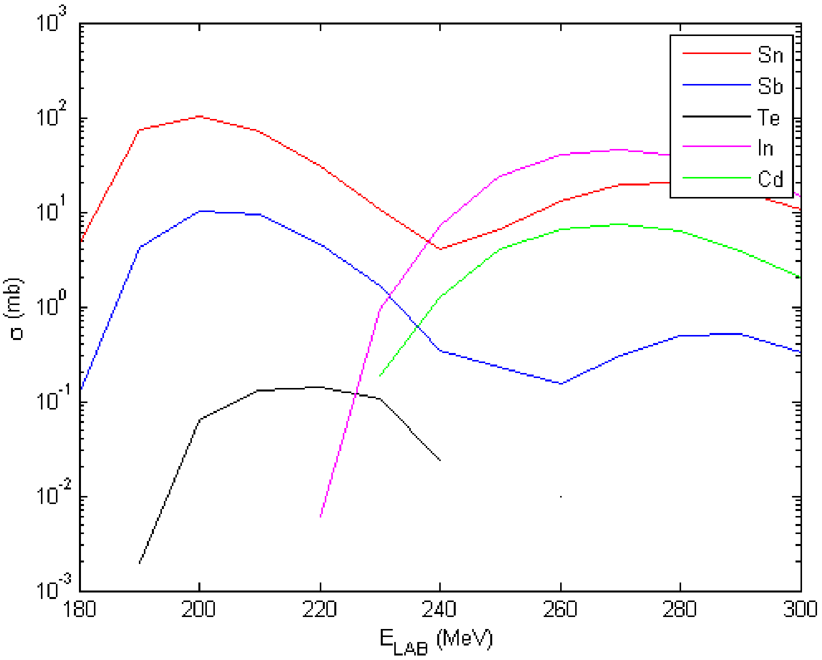

(f) A=106.

Figure 27: PACE4 cross sections for ^{54}Fe beam on a ^{58}Ni target.

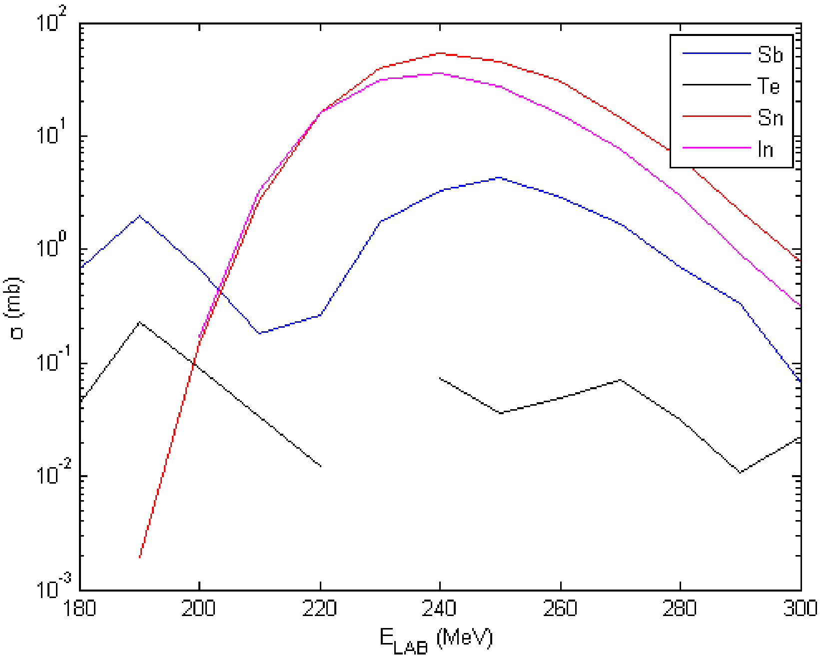

(g) A=107.

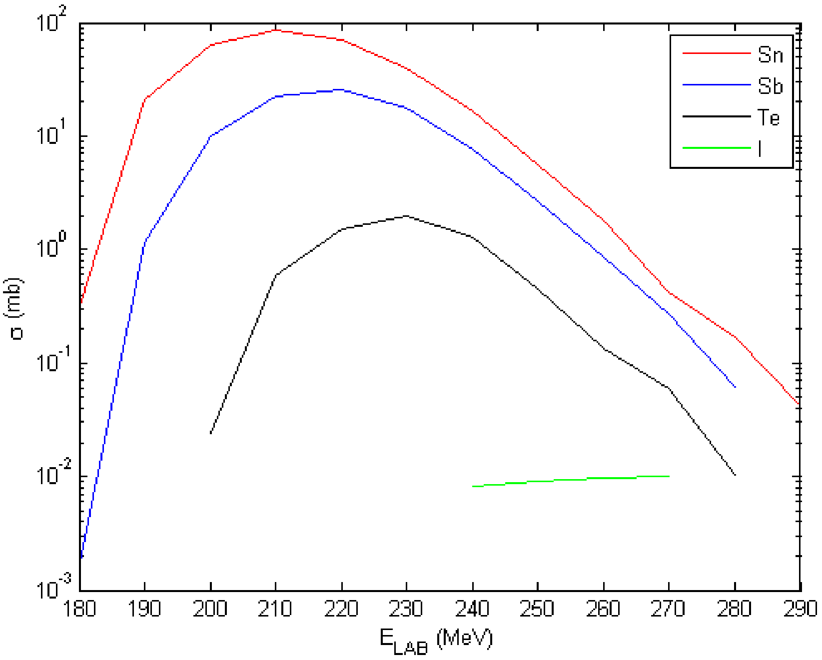

(h) A=108.

Figure 27: PACE4 cross sections for ^{54}Fe beam on a ^{58}Ni target.

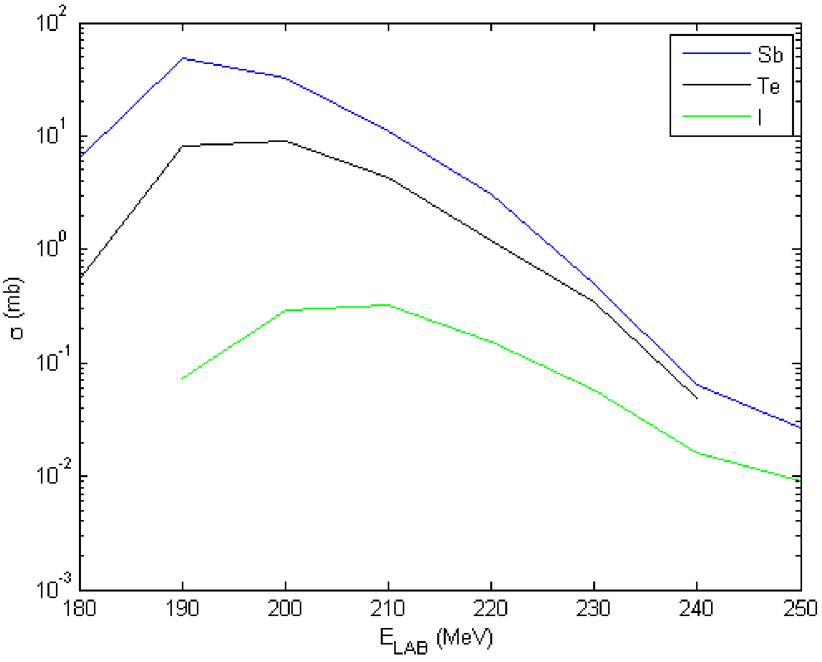

(i) A=109.

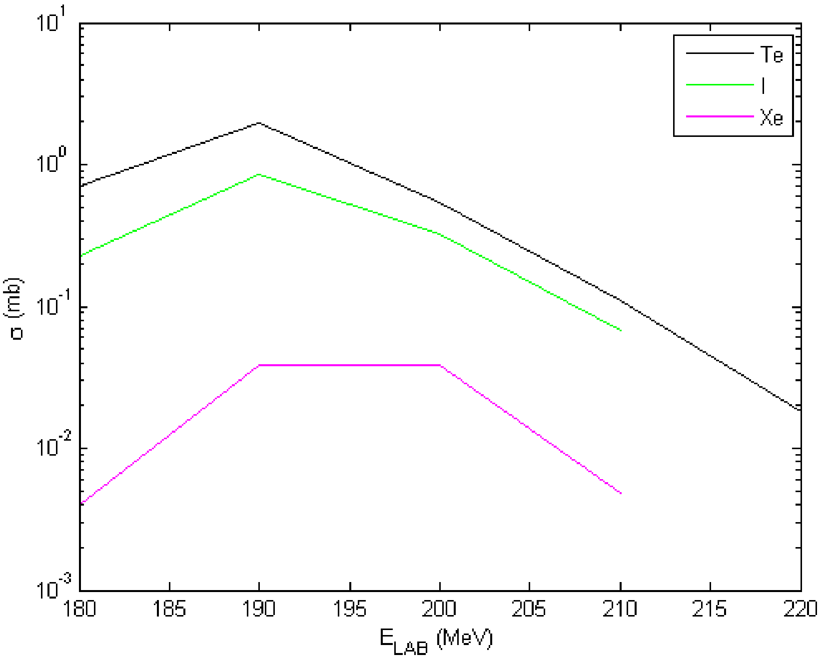

(j) A=110.

Figure 27: PACE4 cross sections for ^{54}Fe beam on a ^{58}Ni target.